Redox-coupling with RPTPγ regulates the growth factor response of EGFR

Dissertation

Zur Erlangung des akademischen Grades eines

Doktors der Naturwissenschaften

(Dr. rer. nat.)

der Fakultät Chemie und Chemische Biologie

der Technischen Universität Dortmund

vorgelegt von

Maitreyi S Joshi

Juni 2021

Vorgelegt im Juni 2021
von Maitreyi S Joshi

Gutachter:
Prof. Dr. Philippe I H Bastiaens
Dr. Leif Dehmelt

The work presented in this dissertation was performed in the laboratory of
Prof. Dr. Philippe I H Bastiaens at the Max Planck Institute for Molecular Physiology,
Dortmund, Germany.

The results in this thesis have been partially included in the following publications:

1. Interdependence between EGFR and phosphatases spatially established by vesicular dynamics generates a growth factor sensing and responding network, *Cell systems* (2018)

Angel Stanoev, Amit Mhamane, Klaus C Schuermann, Hernan E Grecco, Wayne Stallaert, Martin Baumdick, Yannick Bruggemann, Maitreyi S Joshi, Pedro Roda-Navarro, Sven Fengler, Rabea Stockert, Lisaweta Roßmannek, Jutta Luig, Aneta Koseska, and Philippe IH Bastiaens.

2. Receptor-like protein tyrosine phosphatase-γ is a redox master regulator of EGFR signaling response, (*in preparation*)

Maitreyi S Joshi, Angel Stanoev, Lisaweta Roßmannek, Philippe IH Bastiaens

Eidesstattliche Versicherung (Affidavit)

Name, Vorname
(Surname, first name)

Matrikel-Nr.
(Enrolment number)

Belehrung:

Wer vorsätzlich gegen eine die Täuschung über Prüfungsleistungen betreffende Regelung einer Hochschulprüfungsordnung verstößt, handelt ordnungswidrig. Die Ordnungswidrigkeit kann mit einer Geldbuße von bis zu 50.000,00 € geahndet werden. Zuständige Verwaltungsbehörde für die Verfolgung und Ahndung von Ordnungswidrigkeiten ist der Kanzler/die Kanzlerin der Technischen Universität Dortmund. Im Falle eines mehrfachen oder sonstigen schwerwiegenden Täuschungsversuches kann der Prüfling zudem exmatrikuliert werden, § 63 Abs. 5 Hochschulgesetz NRW.

Die Abgabe einer falschen Versicherung an Eides statt ist strafbar.

Wer vorsätzlich eine falsche Versicherung an Eides statt abgibt, kann mit einer Freiheitsstrafe bis zu drei Jahren oder mit Geldstrafe bestraft werden, § 156 StGB. Die fahrlässige Abgabe einer falschen Versicherung an Eides statt kann mit einer Freiheitsstrafe bis zu einem Jahr oder Geldstrafe bestraft werden, § 161 StGB.

Die oben stehende Belehrung habe ich zur Kenntnis genommen:

Official notification:

Any person who intentionally breaches any regulation of university examination regulations relating to deception in examination performance is acting improperly. This offence can be punished with a fine of up to EUR 50,000.00. The competent administrative authority for the pursuit and prosecution of offences of this type is the chancellor of the TU Dortmund University. In the case of multiple or other serious attempts at deception, the candidate can also be unenrolled, Section 63, paragraph 5 of the Universities Act of North Rhine-Westphalia.

The submission of a false affidavit is punishable.

Any person who intentionally submits a false affidavit can be punished with a prison sentence of up to three years or a fine, Section 156 of the Criminal Code. The negligent submission of a false affidavit can be punished with a prison sentence of up to one year or a fine, Section 161 of the Criminal Code.

I have taken note of the above official notification.

Ort, Datum
(Place, date)

Unterschrift
(Signature)

Titel der Dissertation:
(Title of the thesis):

Ich versichere hiermit an Eides statt, dass ich die vorliegende Dissertation mit dem Titel selbstständig und ohne unzulässige fremde Hilfe angefertigt habe. Ich habe keine anderen als die angegebenen Quellen und Hilfsmittel benutzt sowie wörtliche und sinngemäße Zitate kenntlich gemacht.
Die Arbeit hat in gegenwärtiger oder in einer anderen Fassung weder der TU Dortmund noch einer anderen Hochschule im Zusammenhang mit einer staatlichen oder akademischen Prüfung vorgelegen.

I hereby swear that I have completed the present dissertation independently and without inadmissible external support. I have not used any sources or tools other than those indicated and have identified literal and analogous quotations.

The thesis in its current version or another version has not been presented to the TU Dortmund University or another university in connection with a state or academic examination.*

*Please be aware that solely the German version of the affidavit ("Eidesstattliche Versicherung") for the PhD thesis is the official and legally binding version.

Ort, Datum
(Place, date)

Unterschrift
(Signature)

Contents

List of figures

List of tables

Abbreviations

5P-EGF	5 minutes pulse of EGF-Alexa647
a.u.	arbitrary units
Ab	antibody
Akt/PKB	protein kinase B
ALL	acute lymphoblastic leukemia
Cas9	CRISPR-associated protein 9
CBL	Casitas B-lineage lymphoma proto-oncogene
cDNA	complementary DNA
CRC	colorectal cancer
CRISPR	clustered regularly interspaced short palindromic repeats
DMEM	Dulbecco´s modified Eagle´s medium
DMSO	dimethyl sulfoxide
DNA	deoxyribnucleic acid
DTT	Dithiothreitol
ECD	extracellular domain
EE	early endosome
EGF	epidermal growth factor
EGFR	epidermal growth factor receptor
ER	endoplasmic reticulum
ERK	extracellular signal-regulated kinase
FBS	Fetal Bovine Serum
FLAP	fluorescence loss after photoactivation
FLIM	fluorescence lifetime imaging microscopy
FRET	Förster resonance energy transfer
HPLC	high performance liquid chromatography
hr	Hour
IF	Immunofluorescence

IP	Immunoprecipitation
Kb	kilo base pair
KD	Knock-down
kD	kilo Dalton
KO	Knock-out
LB	lysogeny broth
LE	late endosome
LY	Lysosome
MCF10A	Michigan cancer foundation 10A
MCF7	Michigan cancer foundation 7
mCitrine	monomeric citrine
min	Minutes
mTFP	monomeric teal fluorescent protein
NA	numerical aperture
NM	nuclear membrane
NOX	NADPH oxidase
NPC	nasopharyngeal carcinoma
NSCLC	non-small-cell lung carcinoma
paGFP	photoactivable green fluorescent protein
PBS	phosphate buffered saline
pH	Potential of hydrogen
PM	plasma membrane
PTB	phosphotyrosine binding
PTP	protein tyrosine phosphatase
pY	Phosphotyrosine
R	Radius
RE	recycling endosome
RNA	Ribonucleic acid
ROS	reactive oxygen species
RPTP	receptor-like protein tyrosine phosphatase

RTK	receptor tyrosine kinase
s	Second
S-EGF	sustained stimulus of EGF-Alexa647
sgRNA	single guide RNA
SH2	src homology 2
siRNA	small interfering RNA
SOD	Superoxide dismutase
Src	proto-oncogene tyrosine-protein kinase Src
STM	spatiotemporal map
TBS	tris-buffered saline
TKD	tyrosine kinase domain
TM	Transmembrane
WB	western blot
WT	wild type
α_{oxi}	fraction of oxidized protein
α_{p}	fraction of phosphorylated protein

Abstract

Somatic cells rely on surface receptors like receptor tyrosine kinases (RTK) that are situated at the cell-surrounding interface to sense the environmental cues encoding the information about nutrients, cell growth and tissue damage. Proto-oncogenic epidermal growth factor receptor (EGFR) is a prominent RTK that binds to extracellular epidermal growth factor (EGF) and transduces the associated signal patterns inside the cell. Spatial re-organization of EGFR and its interactions with protein tyrosine phosphatases (PTPs) bridge EGF-binding to EGFR signaling to yield diverse cell fate outcomes. By exerting their phosphatase activities PTPs regulate the sensitivity and response dynamics of EGFR to growth factors. This raises a question on how do PTPs inhibit the spurious activation of EGFR without hindering its ligand dependent activation.

In this thesis, the coupling of EGFR with plasma membrane (PM)-based receptor-like protein tyrosine phosphatase-γ (RPTPγ) and endoplasmic reticulum (ER)-bound T-cell protein tyrosine phosphatase (TCPTP) is examined to decipher the regulatory mechanisms that make EGFR capable of responding to the growth factor signals. We prove that expression of RPTPγ is essential to suppress the anomalous activation of EGFR. The lack of RPTPγ associated phosphatase activity makes the system susceptible to ligand-independent activation that turns it blind to the upcoming EGF signals. Consequently, cancer cells lacking RPTPγ expression exhibit constitutive activity of EGFR. On the other hand, inhibition of RPTPγ activity is necessary to trigger the activation of EGFR. This is achieved by EGF induced oxidation of the catalytic cysteine of RPTPγ by the activation of reactive oxygen species (ROS) generating NOX-complexes. In the absence of NOX-activity, activation of EGFR is inhibited as a consequence of unhindered RPTPγ catalytic activity. The regulation of EGFR response by the phosphatase activity of RPTPγ and the EGFR kinase activity dependent regulation of RPTPγ generates a ROS actuated toggle switch at the PM.

By designing a live-cell imaging probe for the spatial resolution of oxidized proteins, we show that the EGFR activity dependent oxidation of RPTPγ happens at the PM by localized ROS production. Vesicular recycling reduces RPTPγ and restores its catalytic activity by exposing it to the reducing environment of the cytoplasm. Additionally, endocytosis of EGFR establishes its interaction with TCPTP that regulates EGFR signaling duration by dephosphorylation. Therefore, vesicular recycling couples the redox cycle of RPTPγ to the activity cycle of EGFR and also maintains the reversibility in the system. The interaction between RPTPγ and monomeric EGFR spanning from the plasma membrane to recycling endosomes adds a spatial dimension to their regulation. By demonstrating its coupling with EGF-induced EGFR activity, we prove redox regulation of RPTPγ as a major coordination mechanism that prevents EGFR from attaining uncontrolled signaling but allows for its EGF dependent signal propagation.

Zusammenfassung

Somatische Zellen sind auf Oberflächenrezeptoren wie Rezeptor-Tyrosin-Kinasen (RTK) angewiesen, die sich an der Grenzfläche zwischen Zellen und Umgebung befinden, um Umweltsignale zu erfassen, die Informationen über Nährstoffe, Zellwachstum und Gewebeschäden kodieren. Der proto-onkogene epidermale Wachstumsfaktor-Rezeptor (EGFR) ist ein zentraler RTK, der an den extrazellulären epidermalen Wachstumsfaktor (EGF) bindet und die damit verbundenen Signalmuster innerhalb der Zelle umwandelt. Die räumliche Reorganisation von EGFR und seine Interaktionen mit Protein-Tyrosin-Phosphatasen (PTPs) koppeln die EGF-Bindung mit der EGFR-Signalweiterleitung, um unterschiedliche Zellschicksale zu hervorzubringen. Mittels ihrer Phosphatase-Aktivitäten regulieren PTPs die Sensitivität und Ansprechdynamik von EGFR auf Wachstumsfaktoren. Dies wirft die Frage auf, wie PTPs die unberechtigte Aktivierung von EGFR hemmen kann, ohne seine liganden-abhängige Aktivierung zu behindern.

In dieser Arbeit wird die Kopplung von EGFR mit Plasmamembran (PM)-lokalisierter Rezeptor-ähnlicher Protein-Tyrosin-Phosphatase-γ (RPTPγ) und endoplasmatischer Retikulum (ER)-gebundener T-Zell-Protein-Tyrosin-Phosphatase (TCPTP) untersucht, um die Regulationsmechanismen zu entschlüsseln, die EGFR dazu befähigen, auf die Wachstumsfaktorsignale zu reagieren. Wir zeigen, dass die Expression von RPTPγ essentiell ist, um die anomale Aktivierung von EGFR zu unterdrücken. Die Abwesenheit von RPTPγ-assoziierter Phosphatase-Aktivität macht das System anfällig für eine ligandenunabhängige Aktivierung, die es für kommende EGF-Signale blind macht. Folglich zeigen Krebszellen, denen die RPTPγ-Expression fehlt, eine konstitutive Aktivität von EGFR. Andererseits ist die Hemmung der RPTPγ-Aktivität notwendig, um die Aktivierung von EGFR auszulösen. Dies wird durch die EGF-induzierte Oxidation des katalytischen Cysteins von RPTPγ durch die Aktivierung von reaktiven Sauerstoffspezies (ROS) erreicht, die NOX-Komplexe erzeugen. In Abwesenheit von NOX-Aktivität wird die Aktivierung von EGFR als Folge der ungehinderten katalytischen Aktivität von RPTPγ gehemmt. Die Regulierung der EGFR-Antwort durch die Phosphatase-Aktivität von RPTPγ und die von der EGFR-Kinase-Aktivität abhängige Regulierung von RPTPγ erzeugen einen ROS-abhängigen Kippschalter an der PM.

Durch die Entwicklung einer Live-Cell-Imaging-Sonde für die räumliche Auflösung oxidierter Proteine zeigen wir, dass die EGFR-aktivitätsabhängige Oxidation von RPTPγ an der PM durch lokale ROS-Produktion stattfindet. Das vesikuläre Recycling reduziert RPTPγ und stellt seine katalytische Aktivität wieder her, indem es der reduzierenden Umgebung des Zytoplasmas ausgesetzt wird. Darüber hinaus ermöglicht die Endozytose von EGFR seine Wechselwirkung mit TCPTP, welches die EGFR-Signaldauer über Dephosphorylierung reguliert. Somit koppelt vesikuläres Recycling den Redoxzyklus von RPTPγ an den Aktivitätszyklus von EGFR und erhält auch die Reversibilität im System. Die Interaktion zwischen RPTPγ und monomerem EGFR, die sich von der Plasmamembran bis hin zu den Recycling-Endosomen erstreckt, fügt ihrer Regulation eine räumliche Dimension hinzu. Durch den Nachweis seiner Kopplung mit EGF-induzierter EGFR-Aktivität enthüllen wir die Redox-Regulierung

von RPTPγ als einen wichtigen Koordinationsmechanismus, der verhindert, dass EGFR unkontrolliert Signale überträgt, aber seine EGF-abhängige Signalausbreitung zulässt.

Introduction

Development and growth of a living organism is the consequence of the collective behavior of the constituent cells and their interactions with the extracellular matrix. One of the ways to establish such cellular communication is through chemical signaling via signaling molecules like cytokines, hormones and growth factors. These cues are organized in space and time to convey the signals of stress, survival and nutrient abundance that are then reflected into broader cell responses like metabolic alteration, inflammation and tissue remodeling. Cells sense the changes in the environment with surface receptors that act as receivers for the signaling messengers and translate the encoded information through the activation of intracellular proteins. Cells can exhibit completely opposite responses to different growth factors as well as to varied concentrations of the same growth factor by spatially organizing the receptor induced singling activities[1]. Therefore, converting external stimuli to a functional response is not merely a linear aftermath of the binding of signaling molecules to the receptor. These functionally distinct responses result from the context dependent reengineering of the intracellular causal links that form a growth factor processing network. Depending on the cellular environmental context, such a network can evolve spatiotemporally by altering the biochemical interactions and the strengths of feedback/feedforward loops[2,3,4,5].

An example of context dependent signaling is described for Cos7 cells in which Eph receptor activation at cell-cell contacts causes suppression of EGF-promoted migratory signaling and promotes cell proliferation. At the physiological levels of EGF in the environment, these cells rely on Akt-dependent vesicular recycling of EGFR to constantly retain a steady state population of EGFR on the PM so as to keep sensing the chemotactic signals in terms of EGF gradients. However, at higher cell densities, activation of Eph receptor by A1 causes Akt-inhibition at the PM and therefore traps EGFR in early endosomes. Altered vesicular trafficking of EGFR changes the spatial distribution of EGFR activity and cuts off the positive feedback to Akt activation at the PM. Entrapment of EGFR preserves the ERK activation on endosomes and consequently ERK dependent cell proliferation but selectively hinders migration associated with Akt activation[6].

EGFR emerges as a fundamental node in such regulatory networks due to the involvement of its kinase activity in various developmental and growth associated processes like lung, colon, brain formation during embryogenesis[7,8,9,10] as well as mammary gland activity in fully formed organisms[11]. The downregulation of EGFR signaling is linked to neurodegenerative diseases[12,13] whereas its overexpression is proved to cause onset of tumorigenesis[14,15]. In order to comprehend the diversity of EGFR signaling, along with its activation it is important to understand the regulatory interactions with dephosphorylating activities like PTPs and inter-organelle communication mechanisms like vesicular trafficking that are elaborated in subsequent sections.

1.1 Growth factor sensing by epidermal growth factor receptor (EGFR)

1.1.1 EGFR: a prominent member of receptor tyrosine kinases (RTK) family

Cell surface receptors hold a prime place in intracellular signaling networks owing to their function as a primary recipient of the environmental cues which then manifest into signaling responses. Receptor tyrosine kinases (RTK) stand out as an important class of transmembrane receptors because of their involvement in cell regulatory and survival processes like proliferation, differentiation, cell migration and cell cycle control. There are 58 known RTKs in humans and they share a distinct molecular architecture consisting of an extracellular ligand-binding domain, a single-pass transmembrane domain, intracellular juxtamembrane domain, an intracellular component with a tyrosine kinase domain (TKD) and C-terminal tail harboring signaling associated tyrosine residues[16,17].

The activation of RTK family members like EGFR or PDGFR is described to rely on the ligand binding induced conformational change in the receptor structure, leading to dimerization[18,19]. However, receptors like insulin receptor or IGF1 are expressed as disulfide linked dimers and they attain activity after the ligand induced structural reformation[20,21]. Despite the organizational differences before ligand binding, activation and signal transduction by RTKs show distinct analogy across the family. Upon ligand binding, *cis*-inhibitory interactions on the receptors subside and they are stabilized in active conformation to attain dimeric or oligomeric form resulting in *trans*-phosphorylation of tyrosine residues on the involved species. These sites then serve as docking sites for effector proteins like GRB2 or CBL that propagate the signal further in the cytosol and cell organelles[17].

An important section of RTK family is ErbB/HER subgroup consisting of four members viz. ErbB1 (HER1/EGFR), ErbB2 (HER2), ErbB3 (HER3) and ErbB4 (HER4)[22]. Expression of ErbB receptors is characterized in epithelial, cardiac, neuronal and pituitary gland cells; accounting to their wide spanning function from tissue development to wound healing. For example, ErbB module is often associated with regulation of cell migration in epithelia, accounting to its role during embryogenesis as well in facilitating invasion of cancer cells to blood and lymph nodes. EGFR, the first discovered member of ErbB family has attained physiological importance due its conspicuous link with numerous cancers and developmental defects[23,24,25].

Like other members of ErbB group, activation of EGFR can take place upon binding to the different cognate ligands like EGF, transforming growth factor-α (TNF-α), amphiregulin (AREG), heparin-binding EGF (HB-EGF), betacellulin (BTC), epigen (EGN) and epiregulin (EPR). EPR and EGN are low-affinity ligands to EGFR, which function as partial agonists of EGFR dimerization but complete agonists of EGFR phosphorylation. On the other hand, TNF-α and EGF are high affinity ligands that bind to EGFR with a K_D of 0.1–1 nM, around 10-100-fold stronger than low affinity ligands[26]. Binding to different cognate ligands yields seemingly diverse cellular and phenotypic responses as a result of the structural change-induced activation of varied signaling residues on EGFR[27].

1.1.2 Structural basis of EGFR Activation

X-ray crystal studies have elaborated the structure of the EGFR extracellular domain (ECD) comprising of 4 subdomains (I-IV) (Figure 1, left). Subdomains I and III form a ligand binding pocket whereas cysteine rich subdomain II harboring a dimerization arm intramolecularly interacts with IV so as to uphold a compact tethered conformation in the absence of a ligand. Exposure to ligand bridges two binding sites in subdomains I and III on the same receptor and promotes a structural rearrangement in the ECD. This results in the disruption of the *cis*-autoinhibitory tether and frees up the dimerization arm which was previously confined to the subdomain IV, converting ECD into back-to-back dimer conformation with ligand residing between subdomains I and III of the individual receptors. Structural changes in the ECD release the autoinhibition of juxtamembrane domain from the PM and further propagates the series of intramolecular rearrangements to the cytosolic side of the receptor[28,29,18].

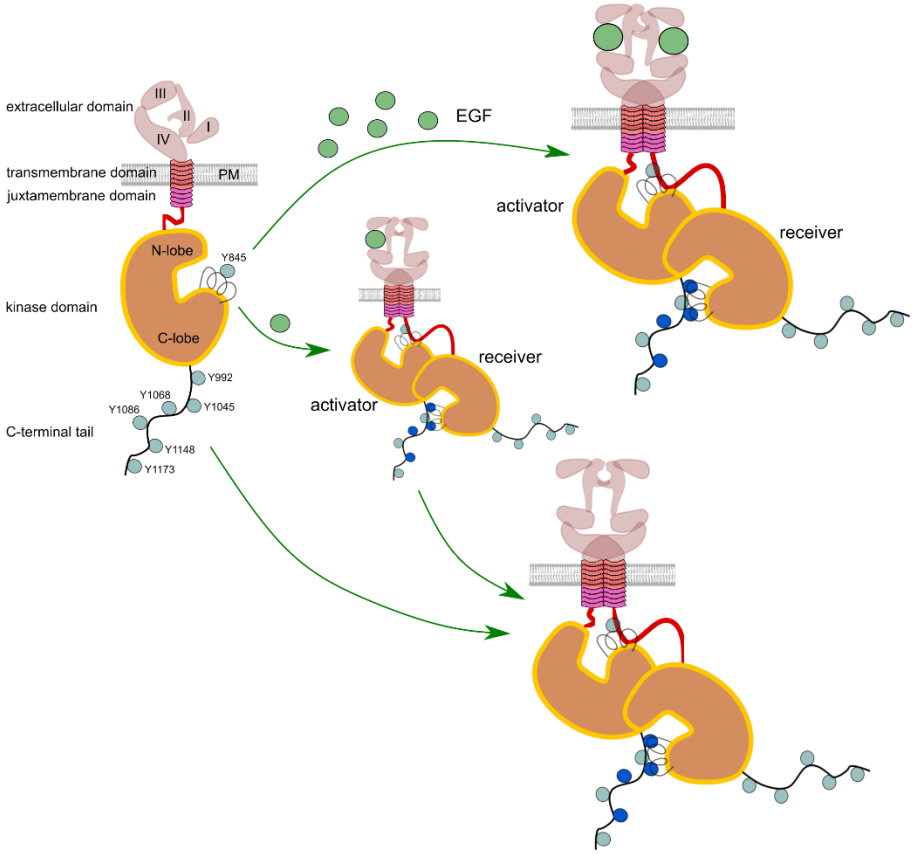

Figure 1: Domain structure and activation of EGFR

Human EGFR has 5 major structural components: an extracellular domain that interacts with ligand environment, a transmembrane domain that connects to cytosolic parts like juxtamembrane domain, tyrosine residues (cyan circles) containing kinase domain and a C-terminal tail. Upon EGF binding (green circles), the structural change induced in extracellular domain imparts conformational change in intracellular domains that results in asymmetric dimerization of two EGFR molecules. One of the receptors acts as an 'activator' that trans-phosphorylates the tyrosines (blue circles) on the partner 'receiver' receptor. At low concentrations of EGF, tyrosine residues are directly phosphorylated by a ligand bound activator or indirectly by ligandless-activated EGFR monomer.

The kinase domain of EGFR comprises of two lobes viz. C-lobe and N-lobe. In the ligand prompted mode of activation, C-lobe of one of the participating EGFR molecules (acting as an activator) interacts

with the N-lobe of the binding ally (serving as a receiver) to form a symmetric extracellular module and an asymmetric dimeric structure at the intracellular part (Figure 1, top right). In this mode of activation, conformational changes in the αC-helix on the N-lobe of the receiver helps to overcome the autoinhibitory interactions observed in monomers and the activation loop of the EGFR TKD is stabilized in the active kinase conformation. On the receiver's TKD, the catalytic cleft opens-up so as to ease the phosphor-transfer from ATP molecule to tyrosine residues[30]. The activation of the intracellular kinase domain results in the transphosphorylation of tyrosine residues (e.g., Y974, Y992, Y1045, Y1068, Y1086, Y1148, Y1173) on the C-terminal tail of the activator molecule within the EGFR dimer. Src homology 2 domain (SH2) or phosphotyrosine-binding domains (PTB) containing adaptor proteins are subsequently recruited to these phosphorylated sites to carry out further signal propagation[31].

Abundance of EGF in the extracellular environment results in EGFR ligand-binding saturation and yields an extracellular domain module configuration with a 2:2 EGF:EGFR stoichiometry[32,33]. However, in the physiological conditions where concentration of EGF is far from saturation, an asymmetrical extracellular domain module with a 1:2 EGF:EGFR stoichiometry and altered binding interface is likely to be adopted[34] (Figure 1, middle). These short-lived EGFR dimers act as catalytic intermediates where exchange of activated ligandless monomers can happen that can further trigger the cascade of the activation of ligandless monomers[35,36,5] (Figure 1, bottom right). Being in transient association with activated monomers, inactive EGFR monomers can undergo change in the kinase domain conformation. Phosphorylation of tyrosine-Y845 within TKD suppresses the intrinsic disorder in the αC-helix region by stabilizing the active conformation of the receptor[37,38]. The activation of receiver in this case relies on the recruitment of kinase Src on the signaling tyrosine site-Y1068 of the activator that subsequently activates Y845[39,40,41]. The autoinhibitory interactions could also be overcome in the absence of ligand binding due to thermal fluctuations, EGFR overexpression or acquisition of oncogenic mutations (e.g., L834R or T790M)[42].

1.1.3 EGFR signaling modulation by vesicular trafficking

Activation of EGFR followed by the recruitment of the signaling effectors propagate the PM originated EGFR activity to the cytoplasm. Subsequent invagination of the membrane, envelopes EGFR in vesicular structures and transports it from the PM towards the perinuclear areas[43,44,45]. Although EGFR undergoes continuous recycling even in the absence of ligand binding, the rate of internalization increases upon EGF treatment. Internalization of the EGFR signaling assembly is achieved by vesicular endocytosis in clatherin coated pits or clatherin independent manner. The clatherin mediated endocytosis has been reported to take place at low EGF concentrations whereas the clatherin independent mechanism is preferred at higher concentrations due to the saturation of the effector machinery associated with the prior[46].

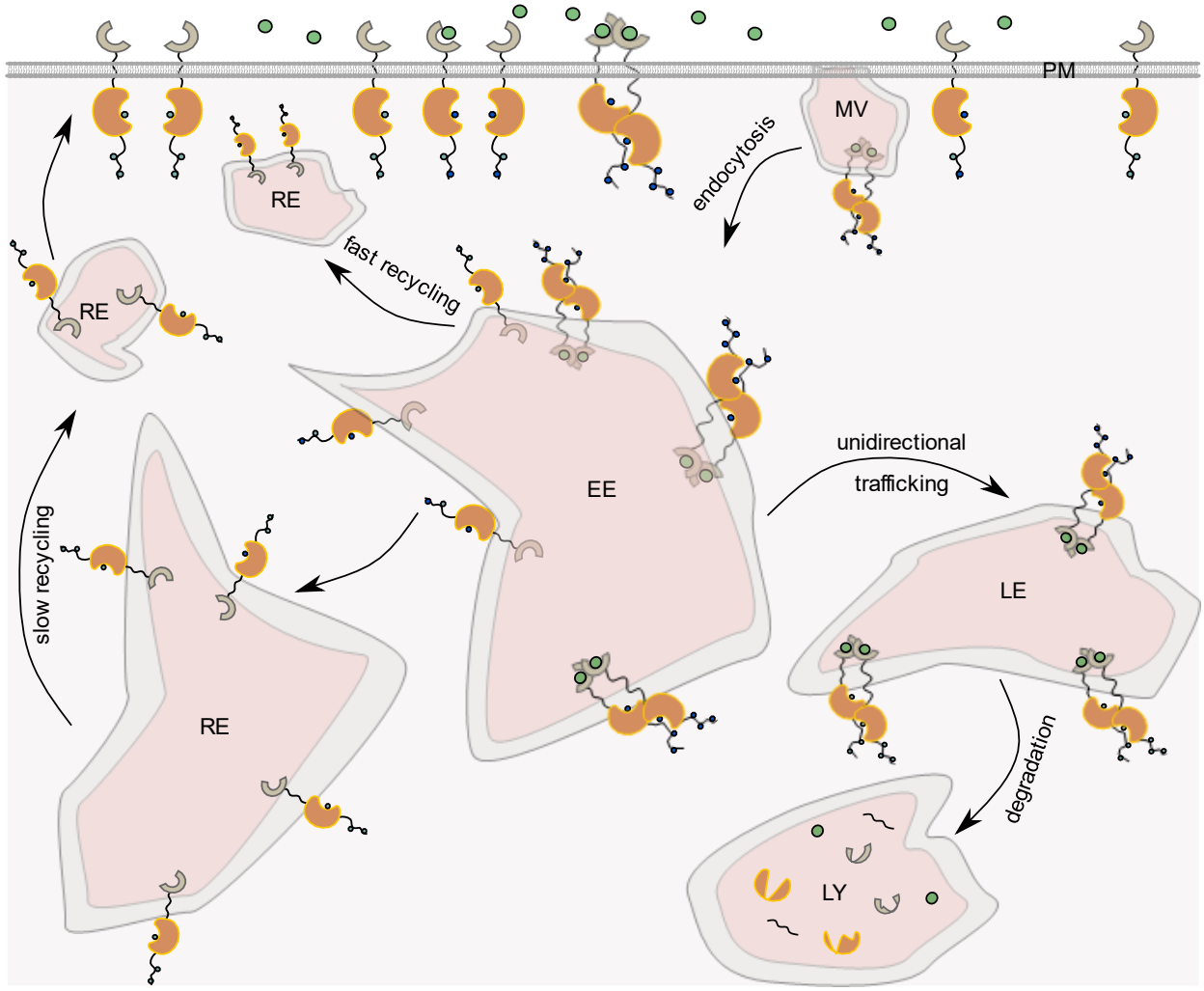

Figure 2: Vesicular trafficking of EGFR

Phosphorylated EGFR is internalized by endocytic machinery that carries the plasma membrane (PM) bound EGFR in membrane vesicles (MV) towards cytosol. EGFR is transported to early endosomes (EE) where depending on its monomeric or dimeric state, it is directed towards recycling endosomes (RE) or late endosomes (LE). The monomeric EGFR is recycled back to the PM from RE whereas EGF-bound dimers are subjected to the unidirectional path of ubiquitin-dependent degradation by moving them to lysosomes (LY).

The vesicular recycling system relies on the activation of PI3K that results in the Akt phosphorylation. Akt controls the intercompartmental transitions between endosomal species. By activating early endosomal effector PIKfyve (FYVEcontaining phosphatidylinositol-3-phosphate 5-kinase) it drives EGFR to early endosomes (EE). Further on, PIKfyve phosphorylates phosphatidylinositol-3-phosphate on the surface of vesicles to phosphatidylinositol-3,5-bisphosphate to aid their transition from the EE to the late endosomes (LE) or recycling endosomes (RE). Apart from the endocytosis Akt is proved to be necessary for the fusion of recycling vesicles from the RE to the PM[47,48]. The route of recycling or unidirectional degradation assigned to an activated EGFR depends on whether its tyrosine site Y1045 is phosphorylated. Since this site serves as a docking site for an adaptor protein called CBL, which being E3 ubiquitin-ligase marks the receptor for ubiquitination[49]. Phosphorylation of Y1045 requires dimerization of EGFR, making the ligand bound dimerized species undergo transitions from the EE to the LE and then to further degradation in lysosomes (LY). The site Y1045 does not undergo

phosphorylation on an active monomeric EGFR. Instead of undergoing ubiquitin driven degradation, monomeric EGFR recycles back to the PM after its EE to RE transition[50].

An important class of proteins that ensure the transport of the vesicles leaving one compartment and fusing to the next are Rab-GTPases[51]. However, their role extends beyond the mere compartmental segregation tags. Expression of these proteins can also alter the biogenesis of the endosomal compartments and the relative distributions of the intracellular proteins trapped in these compartments[52,53]. Most of the organelles participating in the endocytic machinery bear at least one Rab protein on their cytoplasmic face. Rab proteins cycle between GDP bound (inactive) form and GTP bound (active) form. This GDP-GTP exchange reaction is catalyzed by GEF proteins. The GDP-GTP cycle of Rabs complies with their association and dissociation from intracellular membranous structures[54].

Transport of EGFR by the Rab-positive endocytic machinery controls the duration of EGFR signaling in two ways; first, the sorting of EGFR species for recycling or degradation and second, bringing them in contact with dephosphorylating actions of cytosolic PTPs. The ER-associated, catalytically efficient PTP1B and TCPTP dephosphorylate internalized active EGFR mostly near perinuclear membranes[55,56]. The strong phosphatase activities of cytosolic and ER-PTPs make it difficult to imagine the signal propagation of EGFR on endosomes. Contrarily, EGFR is shown to signal on clatherin coated pits[57] and early endosomes[58]. One of the mechanisms that can prevent the immediate quenching of EGFR signaling is the spatial regulation of the catalytic activity of these cytosolic PTPs. Such a regulation is described for PTP1B, in terms of the spatial activity gradient across the ER from the PM-vicinal end to the perinuclear region[59]. This allows for the signaling of endosomal EGFR and accomplishes eventual dephosphorylation when it reaches the dense perinuclear ER.

1.2 Regulation of EGFR by protein tyrosine phosphatases (PTP)

1.2.1 Family of protein tyrosine phosphatases

The PTP genome consists of 107 encoded members distinguished by the active-site characteristic sequence (H/V)CX_5R(S/T), in which the presence of cysteine residue gives them the major enzymatic function. The family is divided into two major clusters: 31 classical phosphotyrosine (pTyr)-specific phosphatases and 68 dual specificity phosphatases (DSPs)[60,61].

According to their intracellular localization, classical PTPs are further sub-classified into transmembrane receptor PTPs (R-PTP) and cytosolic (non-transmembrane NT-PTP) PTPs. Amongst the transmembrane PTPs, 12 possess two catalytic domains (tandem domains), while the remaining contain only one catalytic phosphatase domain. In tandem-domain receptor PTPs, it is the plasma membrane adjacent domain D1 that displays major catalytic activity whereas the activity of the D2 domain (often terms as pseudo-domain) is accounted for its contribution to structural stability and intra-PTP interactions (e.g., homo-dimerization in RPTPα)[62,63,64]. The membrane association of R-PTPs endows some of its members functions similar to cell-adhesion molecules that can aid cell-cell communication and cell-matrix contact (e.g., PTPRκ)[65]. It also eases the establishment of interactions

with localization consorts like RTKs, that can result into the regulation of RTK activity at the PM like in the case of interaction between RPTPf and insulin receptor[66].

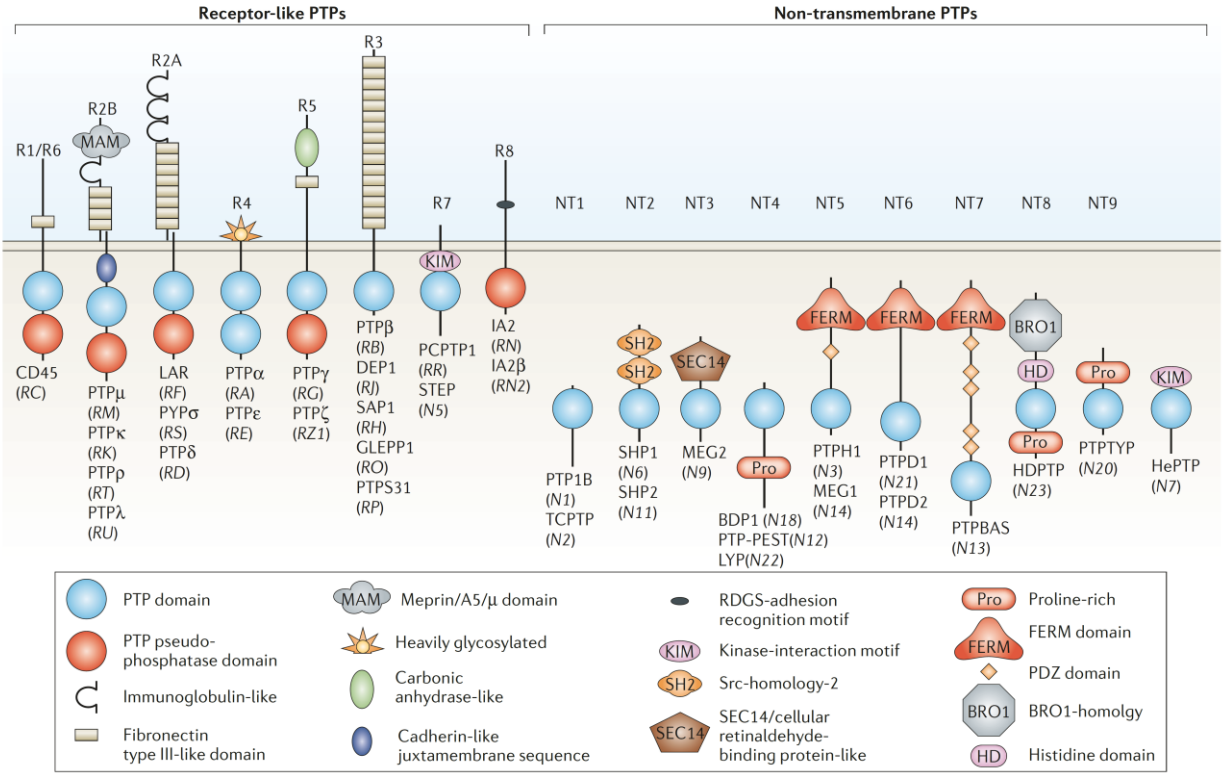

Figure 3: The domain structure of classical PTPs

Protein tyrosine phosphatases (PTPs) mainly classified into two major groups viz. receptor-like PTPs and non-transmembrane PTPs, are designated by their common name with gene name in the parenthesis. Basic structural subdomains are indicated in the inset. Reprinted from [61] with permission. Copyright © 2006, Springer Nature.

The cytosolic members of the family show localization that varies from the cytoplasm to endomembranes like ER and endosomes. They usually have a single catalytic domain possessing dephosphorylating potential. However, their non-catalytic domains regulate the localization of the PTP and thereby control the spatial selectivity and reach of the catalysis. Such a regulation is observed for ER-localized PTP1B and TCPTP. By virtue of their spatial position, these PTPs dephosphorylate endocytosed EGFR upon its ER-adjacent transference[55,56]. The non-catalytic residues are also proved to be crucial in the recognition of active sites on the substrate, like in the case of SHP2 that binds SH2-bound sites on PDGFR[67].

1.2.2 Catalytic activity of PTPs towards EGFR

The major amino acid residues that play a role in the catalytic activity of PTPs are P-loop located cysteine, which by virtue of the low pKa works remarkably good as a nucleophile and aspartate from the WPD-loop, that can act as acid/base depending on the context[68,69]. PTPs employ two step catalytic mechanism for EGFR dephosphorylation (Figure 4). The initial step is the nucleophilic attack of the catalytic cysteine on the phosphate group of the phosphotyrosine-kinase, accompanied by the proton donation of catalytic aspartate to the leaving group -OH to initiate the phosphorous-oxygen bond

cleavage. This gives rise to a thiophosphate intermediate, stabilized by arginine and dephosphorylated kinase substrate. The next step again relies on aspartate however its role as a general base; where it accepts a proton from surrounding water molecule (suitably positioned by glutamine) to facilitate the hydrolysis of phosphorous-sulfur bond. This rate limiting step results in the formation of free phosphate and recovery of active PTP-catalyst[70,71].

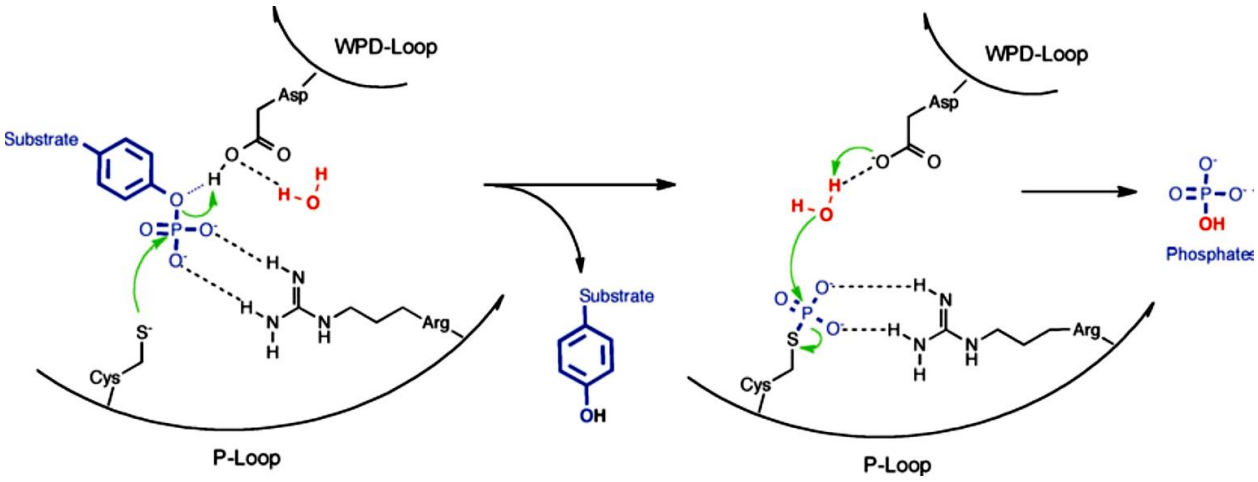

Figure 4: Catalytic mechanism of PTPs for phosphotyrosine dephosphorylation

Catalytic cysteine of PTP (enzyme) exerts nucleophilic attack on phosphorylated tyrosine of RTK (substrate), followed by aspartate induced consecutive proton donation and hydrolysis resulting in dephosphorylated RTK and free PTP. Reprinted from [71] with permission. Copyright © 2013, Springer Nature.

1.3 Regulation of PTPs by catalytic cysteine oxidation

1.3.1 Growth factor induced ROS production and localized signaling

Reactive oxygen species (ROS) encompass a group of highly active oxygen derived molecules like peroxides, superoxide, oxygen free radicals and nitric oxide. Due to their long-known involvement in oxidative stress derived neurodegenerative disorders[72] and DNA damage[73], these molecules have been looked upon as detrimental entities for a cell. However, the positive role of ROS generation emerged in the context of macrophages and neutrophils, where invading micro-organisms are eliminated by employing oxidative burst as an inflammatory mediator[74,75]. In these phagocytes, this was found to be accomplished by NADPH oxidase (NOX)-complexes situated at the PM interface responsible for ROS generation. Eventually, existence of such ROS producing enzymes (NOX family) was soon characterized in non-phagocyte cells playing analogous function of electron transfer across the membrane to convert environmental oxygen to superoxide.

The members of the NOX-complex family form a characteristic assembly of subunits typically consisting of essential cell membrane-based units and subsequently recruited cytosolic units upon activation (Figure 5). For example, the first characterized member of this family-NOX2 contains two major PM-based units: gp91-phox/NOX2 (β-unit)[76] , $p22^{phox}$ (α-unit)[77] and three cytosolic units: $p47^{phox}$, $p67^{phox}$, $p40^{phox}$ [78,79,80]. The PM based components exist in the form of a heterodimer which forms the catalytic core of the complex[77]. $p47^{phox}$ upon phosphorylation pulls along the cytosolic complex of the other

subunits and recruits them on $p22^{phox}$ to form a functional protein assembly at the PM[81]. The activation of the complex also requires recruitment of cytosolic G-proteins like Rac1 or Rac2; that convert to GTP-bound form from their Rho-GDI bound form to join the other subunits[82]. The activated complex aids the production of superoxide by transferring electrons from the cytosolic NADPH to oxygen on the luminal or extracellular region through hemes and flavins. In the case of PM-associated ROS production, superoxide anions react with superoxide dismutase and undergo protonation to yield H_2O_2 [83] followed by penetration through the PM via aquaporin channels or free diffusion. Six other isoforms of NOX2 (NOX1, NOX3-5, DUOX1-2)[84,85,86,87] have been characterized with homologous catalytic core to gp91-phox and subunits like NOXO1-NOXA1 instead of $p47^{phox}$-$p67^{phox}$. Interestingly, NOX1-4 share $p22^{phox}$ as an associate to their main catalytic unit, making it a non-redundant component to these complexes. NOX5 activation is shown to depend on cytosolic Ca^{2+}, but independent of $p22^{phox}$ or cytosolic subunits.

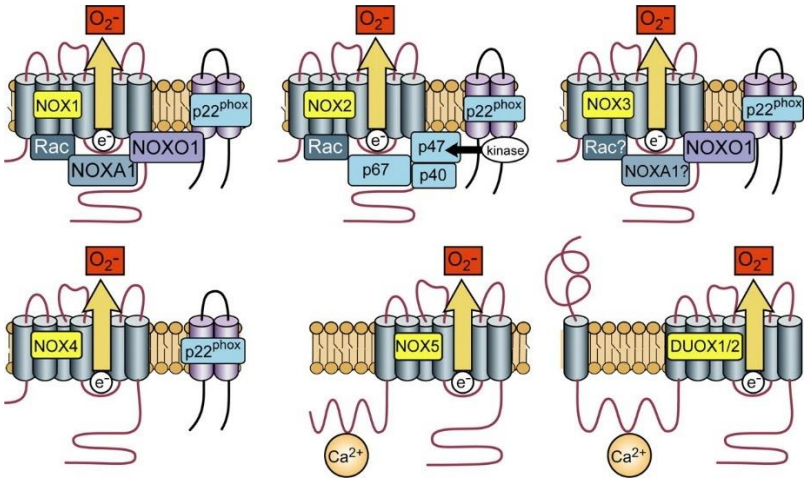

Figure 5: Protein assembly in NOX-complexes

Activation of NOX-complex requires assembly of main membrane bound units with cytosolic subunits. Reprinted from [88] with permission. Copyright © 2007, The American Physiological Society.

Cell cytosol contains a pool of antioxidants that can scavenge the intracellular ROS to maintain redox homeostasis. The cytosol harbors many of such enzymes differing widely in terms of their reaction mechanisms like thiol-based glutathione, peroxidases, thioredoxin[89,90,91] and non-thiol-based enzymes like catalase[92]. Glutathione (GSH), is the most abundant cellular thiol-based antioxidant; which carries out an important function of maintaining redox homeostasis by carrying out reduction of ROS as well as thiol–disulfide exchange reactions with oxidation regulated cysteine containing proteins. Glutathione (GSH) maintains its abundant reduced state in the cytosol under normal conditions and upon exposure to oxidizing agents like H_2O_2 gets oxidized to glutathione disulfide (GSSG). The oxidized form gets reduced back to glutathione upon reaction with NADPH, catalyzed by glutathione reductase (GR)[93].

The presence of such reducing surroundings makes it difficult to envision the survival of H_2O_2 to cause the protein oxidation. However, all of the characterized NOX-complexes are found to assemble on membranous structures like the PM, ER or endosomes. This gives them a niche to form a membrane vicinal compartment that confines the generated ROS and cause the oxidation of the membrane tethered proteins. Redox-active endosomes often termed as “redoxosomes”[94] have been characterized

to show localized oxidation like in the case of SHP2 that gets oxidized through PDGF induced activity of NOX1 and NOX4 on early endosomes[95]. Similarly, oxidation of ER based PTPP1B has been observed as a result of EGF treatment which exhibited reduced state upon treatment with exogenous antioxidant N-acetylcysteine (NAC)[96]. The redox regulation hubs are extensively found on the PM due to the extensive presence of ROS-generating NOX-assemblies as well as cholesterol-rich structures like lipid rafts[97]. Redox sensors like plasma membrane tethered HyPer have elucidated the presence of H_2O_2 microdomains upon activation of EGFR and PDGFR[92]. Such assemblies can promote the instantaneous oxidation of the PM-proximal proteins and facilitate the formation of the ROS gradient in the cytoplasm that can restrain the oxidation reactions spatially.

Additionally, the presence of NOX-assemblies on the PM also connects them with the activity of the growth factor sensing RTKs. This can bring about the phosphorylation of the NOX-associated subunits and Rac proteins to cause the activation of the complex. Such a mechanism of ligand-receptor binding dependent ROS production is demonstrated in the case of PDGFR and EGFR[98,99]; which is accomplished by the receptor phosphorylation induced NOX-activation that goes via the intermediate activation of PI3K and Rac[100,82]. The growth factor induced ROS production and its link to the amplification of RTK activity also points at the role of ROS in the regulation of PM associated PTPs[101].

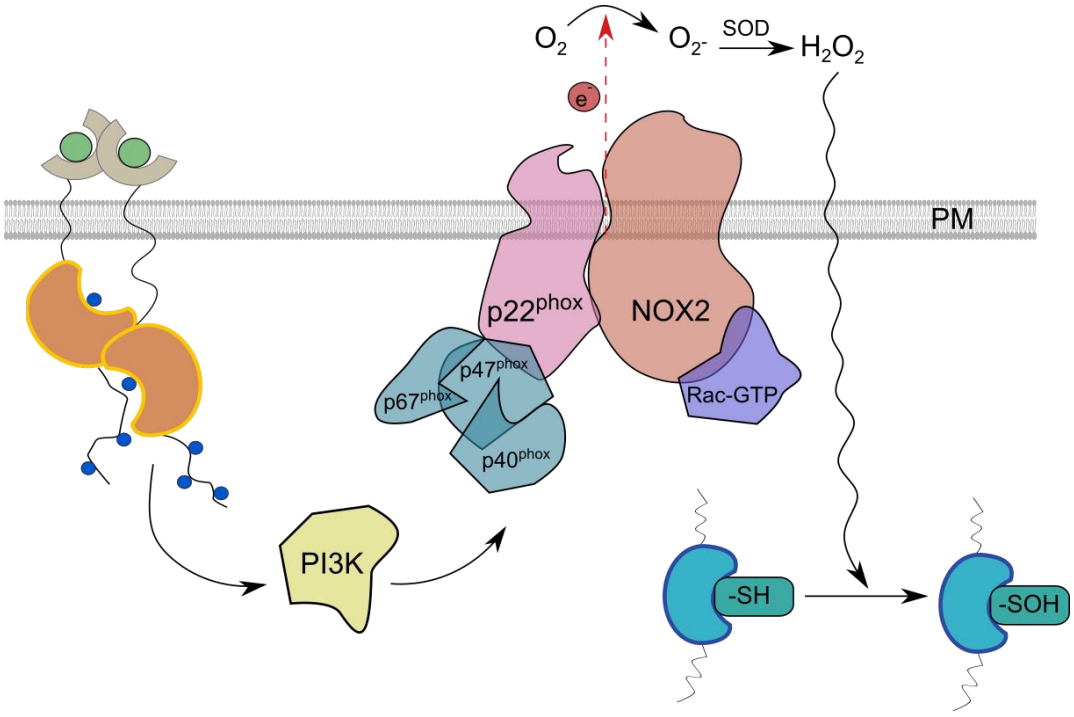

Figure 6: RTK dependent activation of NOX-assembly at the PM

Phosphorylation of RTK triggers the activation cascade that results in the recruitment of cytosolic subunits on plasma membrane (PM)-based main NOX-unit and $p22^{phox}$, leading to the formation of a functional NOX-assembly that converts extracellular O_2 to H_2O_2. Diffusion of H_2O_2 across the PM oxidizes the thiol containing proteins in the cell.

1.3.2 Reversible oxidation of PTPs as a means of signaling

Owing to the microenvironment around the catalytic cleft, the catalytic sites of PTPs harbor a cysteine with lower pKa (4-6) than most of the cysteines localized elsewhere on the protein structure[70]. This

makes the cysteine thiol (-SH) to attain thiolate form ($-S^-$) that leaves it highly susceptible to attack by ROS like H_2O_2 (Figure 7). The reaction with H_2O_2 initially converts the thiolates to sulfenic acid (-SOH)[102] and depending on the concentration of oxidizing agents it can further undergo oxidation to higher derivatives like sulfinic ($-SO_2H$) or sulfonic acid ($-SO_3H$)[103,104]. Subject to the surrounding amino acid residues in the catalytic cleft, the primary form of oxidation can obtain intramolecular disulfide (S-S) or sulfenyl-amide (S-N) state. The formation of intramolecular disulfide was observed in the case of PTEN due to the presence of a second cysteine residue within the active site[105]; whereas, PTP1B adapts the cyclic sulfenyl-amide form soon after getting oxidized to cysteine sulfenic acid[106]. Undergoing these conversions can restrict the further oxidation of the cysteine site to higher derivatives.

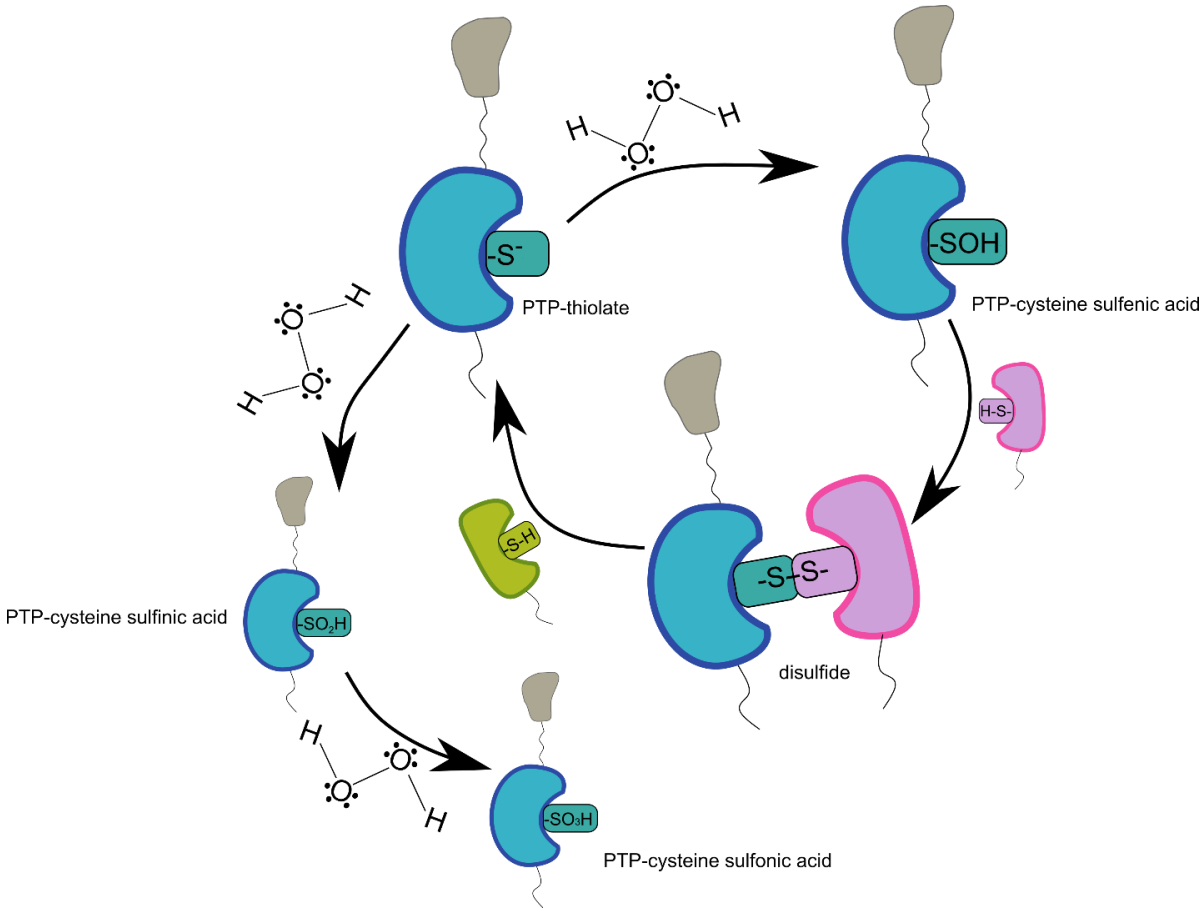

Figure 7: Cysteine oxidation in PTPs

Thiolate ion ($-S^-$) from the catalytic cysteine of protein tyrosine phosphatase (blue) upon exposure to moderate amount of H_2O_2 gets converted to sulfenic acid (-SOH). By reaction with reducing enzymes (magenta and green), this state can revert back to reduced thiol state. Higher concentrations of H_2O_2 result in formation of irreversible states like cysteine sulfinic acid ($-SO_2H$) and sulfonic acid ($-SO_3H$).

In physiological conditions, the thiolate site of PTP exerts nucleophilic attack on H_2O_2 produced in moderate amounts which usually makes it attain reversible cysteine sulfenic acid form. This results in the temporary inhibition of phosphatase activity since sulfenylated cysteine can no longer exert nucleophilic attack on the phosphorylated substrate. The oxidized forms like sulfenic acid, disulfide and sulfenyl-amide can revert back to the thiol state by reactions with the reducing enzymes in the cytosol. Thiol-based reducing enzymes like glutathione (GSH) react with the cysteine sulfenic acid of PTPs to

form an intermolecular disulfide. Finally, this complex reacts with systems like thioredoxin (Trx) to gain back the reduced-active PTP[93,107]. Due to the redox reversibility, cysteine modification to sulfenic acid possesses flexibility in the reaction networks over sulfinic and sulfonic acid forms that are irreversible. Moreover, the amino acids surrounding the catalytic cysteine and the overall structure of the catalytic loop can alter its susceptibility to oxidation, giving rise to different extent of regulation for different PTPs[106]. Such disparity in PTP oxidation can also depend on their localization due to variable exposure to the ROS sources and reducing enzymes.

The enhanced RTK activity upon treatment of cells with ROS sources or depletion of antioxidants hinted towards the activity regulation of PTPs by catalytic site oxidation. However, the direct evidence was lacking. The first few characterized members of the PTP family to indicate redox dependence were PTP1B[108,109], RPTPf and DUSP3[102]. PTP1B and RPTPf showed insulin-receptor activity dependent regulation of the catalytic cysteine. PTP1B also demonstrated EGF dependent oxidation. The high reactivity of catalytic cysteine with the micromolar level H_2O_2 and the formation of cysteine sulfenic acid was also proved with NBD-Cl trapping. Treatment with reducing agents like Dithiothreitol (DTT), β-mercaptoethanol and intracellular thiols like glutathione (GSH) could reverse the oxidized state to reduced thiol state in the case of all of these PTPs[102]. The rate of reduction by thiols is estimated to be 10-100 times slower than the rate of cysteine oxidation. The slower kinetics of reduction makes the cysteine specific reactions of transiently generated H_2O_2 possible even in the presence of high levels of reducing enzymes (1-10 mM intracellular glutathione).

1.3.3 Detection of the cysteine oxidation in PTPs

It has been well established that the oxidation of PTPs serves as a prominent mechanism for the regulation of their activity. However, to differentiate the oxidized fraction of PTPs from the reduced population has been a challenge. One of such initial approaches to differentiate these two pools consisted of the treatment of cell lysates with Iodoacetic acid (IAA) so as to selectively alkylate the thiolate anion of the active site cysteines in the reduced PTPs. Due to the sulfenic acid modification, the cysteines of oxidized PTPs do not undergo alkylation and remain intact. Following alkylation, the oxidized fraction of PTPs in lysates are analyzed by an in-gel phosphatase activity assay[110]. This approach was modified by the separation of oxidized and the reduced species by size exclusion chromatography followed by reduction of oxidized PTPs with reagents like DTT. These PTPs can then be subjected to treatment with biotinylated active-site directed compounds like iodoacetylpolyethylene oxide (IAP) or bromobenzylphosphonate (BBP) and purified by streptavidin pull-down and immunoblotting[111]. Considering the unique reaction properties of sulfur, a set of compounds were formulated like 5-mercapto-2-nitrobenzoic acid (TNB) and 7-chloro-4-nitrobenz-2-oxa-1,3-diazole (NBD-Cl); both of these compounds detect oxidized cysteines by yielding reaction products that show a characteristic absorbance maximum[112,113]. However, they require maintenance of anaerobic conditions to avoid the identification of false positives.

Alongside, the approaches based on dimedone (5,5-Dimethyl-1,3-cyclohexandion) started to emerge due to their ability to directly bind the cysteine sulfenic acid. Dimedone is a cyclic diketone that selectively exerts nucleophilic attack on the sulfenic acid form of oxidized cysteines whereas higher

irreversible forms are spared[114]. Due to its selectivity for reversible sulfenic acid, dimedone based probes gained importance in the signaling networks to detect the protein oxidation. However, the absence of spectral or affinity label selectivity associated with dimedone required the detection of this tag by laborious mass spectrometric approaches. This led to the synthesis of an array of dimedone based compounds that contain a structural modification to facilitate its detection. The first functional analogues of dimedone were reported by Poole *et al.* in 2005, including probes like dimedone warhead containing isatoic acid derived DCP-MAB or 7-methoxycoumarin tagged DCP-MAB[115]. The list was further enriched by fluoresceinamine based DCP-FL, rhodamine based DCP-Rho and biotin based DCP-bio that improved the ease of purification and detectability in polyacrylamide gels[116]. These probes expanded the detection range for the oxidized proteins albeit they had substantial disadvantages: (1) due to their bulkier tag/conjugation sizes they experienced hinderance to reach the catalytic clefts of proteins like PTPs, biasing their detection and (2) poor cell permeability and higher cell toxicity limited their applicability to purified proteins and cell lysates.

To overcome the probe permeability issues associated with the above molecules, an immunodetection-based approach was developed by formulating 2-Thiodimedone-Specific antibody (anti-hapten)[117]. This approach consists of the incubation of live-cells with dimedone that irreversibly traps the oxidized proteins without introducing post-lysis artefacts and their detection with the antibody (Figure 8). Usage of un-modified dimedone on one hand exhibits superior permeability to the encased cysteines in the catalytic cleft of proteins; however, it is not specific to the detection of certain protein of interest. The antibody probes all the proteins in the cells that underwent cysteine oxidation revealing its limitations in terms of protein specificity on western blotting and immunofluorescence. For an accurate detection, this approach still needs to be augmented with protein-specific immunoprecipitation or affinity separation.

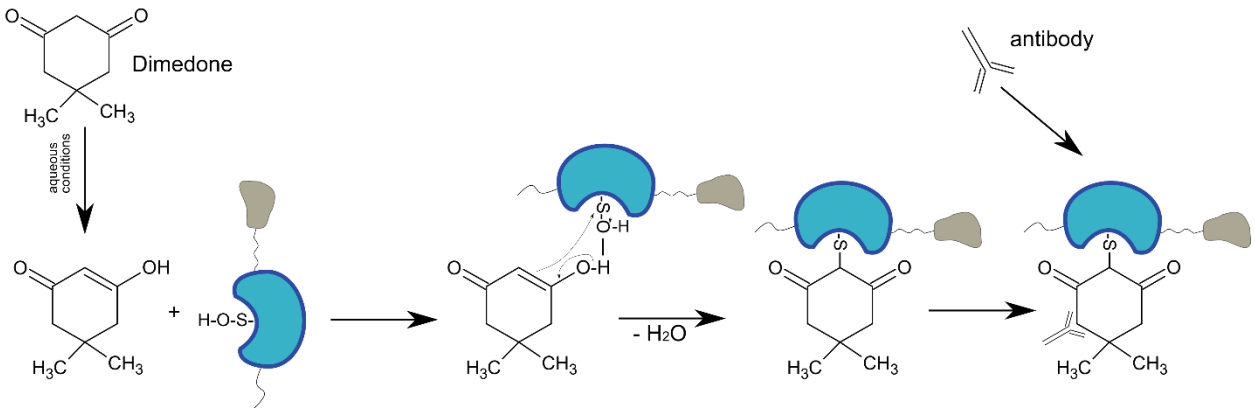

Figure 8: Detection of cysteine oxidation by anti-dimedone antibody

Nucleophilic attack of dimedone on cysteine sulfenic acid of oxidized protein (blue) yields chemoselective alkylation to convert it to a synthetic epitope that is recognized by an antibody.

However, most of the above-mentioned approaches still lacked the ability to directly report the protein oxidation by reaching cell compartments; giving rise to the dimedone derived probes based on azide- or alkyne-conjugation. These included azide-functionalized DAz-1,2 and alkyl-tail bearing DYn-1,2[118,119,120]. Owing to their small size they showed remarkable cell permeability and therefore

applicability for in-cell oxidation mapping purpose. These probes can be subjected to Staudinger ligation or Huisgen cycloaddition to couple them with purification tags or fluorescent labels. Among them, DYn-2 showed the highest conjugation yield upon reactions with azide derived tags and better sulfenic acid binding profile. DYn-2 could detect cysteine sulfenic acid modification on EGFR, PTP1B, PTEN, and SHP2 in response to EGF stimulation, in fixed cells upon fluorescent dye coupling[120]. On the lines of DYn-2, a range of alkyl-azide conjugable probes (like TD, PYD, PRD and BTD) were published that can detect cysteine sulfenic acid with varied reactivities and penetrability in the catalytic pocket[121]. Despite that, the tracking of protein oxidation in live-cells remains quite arduous, making it a challenging problem to tackle in order to understand the dynamics of reversible oxidation in cellular signaling. Therefore, it is important to develop novel imaging approaches that will enable spatiotemporal monitoring of protein oxidation.

1.4 Intracellular mapping of molecular dynamics with fluorescence microscopy

The perception of cell-level events like protein-protein interactions and molecular activities requires precise information on a single cell level. Population based techniques like western blotting or mass spectrometry have shortcomings due to their inability to distinguish single-cell level changes from the bulk sample properties. In this regard, live cell imaging provides a window to peek into the cell interior and also temporally monitor the intracellular transitions. However, in most of the cases the molecules or cellular organelles of interest have translucent properties that hinder their visualization. This difficulty has been overcome by the invention of fluorescent dyes and proteins that can be used to tag the specimen of interest.

The phenomenon of fluorescence consists of the absorbance of photons by molecular species to attain electronically excited states followed by its emission in nanoseconds by giving away energy. The emission of fluorescence that makes the fluorophore tagged biomolecules visible under the microscope is explained by a Jablonski diagram[122,123] (Figure 9A). Before absorbing the energy from a high frequency source, the electrons in the outermost orbital of the fluorophore reside in the ground state (S_0). Upon absorption of light, the electrons in the fluorophore are excited to higher energy level orbitals (either S1 or S2). This transition to an excited state occurs very rapidly (in femtoseconds). Absorbed energy is emitted in the form of vibrational relaxation and fluorescence emission. Thereby, the excited state electrons of the fluorophore return to their low-energy ground state. The absorption wavelength is typically shorter than the emission wavelength (the Stokes shift) or in the other words, the emitted photon has less energy than the absorbed photon (Figure 9B). The fluorescent molecules can be visualized by filtering out the excitation light without blocking the emitted fluorescence[122,123].

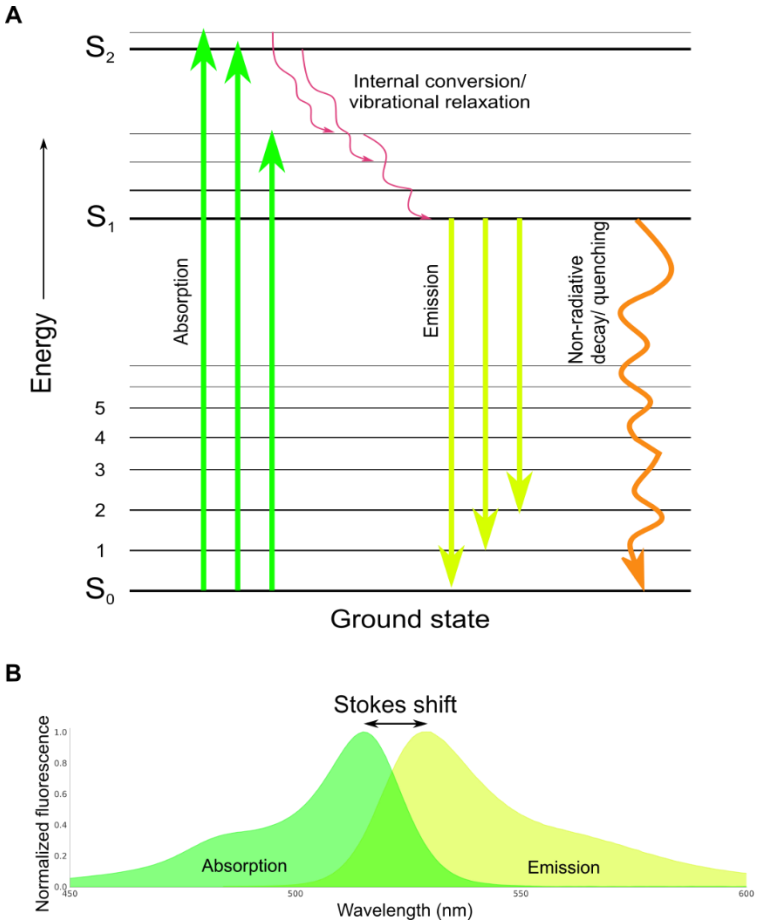

Figure 9: Fluorescence spectroscopy

(A) Jablonski diagram displaying the energy states of a fluorescent molecule. The molecule resides in the lowest energy ground state (S_0) before absorbing energy. After absorption of photo-energy (green arrows) electrons jump to higher energy states like S_1 and S_2. They lose energy by vibrational relaxations (red arrows) to attain low energy S_1 state and finally return back to state S_0 by fluorescence emission (yellow arrows). Electrons can also return back to the ground state by non-radiative decay (orange arrow). **(B)** Absorption (green) and emission (yellow) spectrum of mCitrine.

1.4.1 Fluorescence confocal microscopy for the visualization of biomolecules

The microscopy techniques have been improved to a great extent over the years in terms of increasing the contrast between the signal (information about the species of interest) to the background. Fluorescence microscopy, due to its competence to capture the signal associated with the sample under specific excitation, became a technique of choice for monitoring cellular affairs. Fluorescent microscopes are built on the principle of Stokes fluorescence, in which the specimen is illuminated with one wavelength and the emitted light is filtered to selectively capture the longer wavelength–shifted fluorescence.

The preferred design of fluorescence microscopes in cell-biological studies is epi-fluorescence based[122]. In this configuration apart from the usual role of imaging and magnifying the specimen, the microscope objective also serves as the condenser lens that illuminates it. This approach has advantages over the transmission light microscopes in terms of the reduced amount of reflected excitation light from the specimen that needs to be blocked. The excitation light and fluorescence

emission are separated by a beam splitter dichroic mirror to avoid their overlap in the light path. These dichroic mirrors are used along with an excitation filter to preselect the excitation wavelength and a notch filter that allows the routing of the longer wavelength light to the detector. One of the important components of fluorescent microscopes that can affect the image data quality are objectives, since they act as the source of light that excites the fluorescence in the specimen and the optical element that collects the fluorescence. The objective with high numerical aperture (NA) is preferred because it controls the resolving power and light efficiency of the objective, thereby increasing the number of photons collected[124,123].

However, the sample thickness of the specimen can still severely limit image quality due to increased out-of-focus light. A strategy to overcome this limitation was the laser-scanning confocal microscopy. The technique relies on the usage of a bright point source like lasers to sequentially scan the specimen and the emitted photons are optimally detected with a photomultiplier tube (PMT) or an avalanche photodiode (APD) or the combination of these two technologies: a hybrid detector (HyD)[125]. Confocal microscopy utilizes a pinhole aperture to withhold the out-of-focus light from reaching the detectors. It makes sure that the photons that reach the detector are exclusively from the focal point in the specimen where excitation light was focused. The image can be sequentially compiled in pixel-by-pixel format, by scanning through the sample and recording the fluorescence intensity at each location[124].

1.4.2 FRET-FLIM: a tool for studying molecular interactions

FRET is a process in which energy is transferred non-radiatively via long-range dipole-dipole coupling from an excited state donor molecule to the acceptor molecule without the absorption of fluorescence (by non-radiative transfer) from the donor to the acceptor. This can only happen if the distance between donor and acceptor is less than 10 nm, which goes beyond the resolution limits of the classical light microscope. Therefore, FRET can be utilized to determine the extent of molecular interaction or vicinity in recombinant proteins as well as in live cells[126,127].

Such a mode of energy transfer relies on the physical distance between the donor and the acceptor molecule, the overlap between the donor emission spectrum with the acceptor absorption spectrum and the relative orientation of the donor emission dipole moment and the acceptor absorption dipole moment. The efficiency of FRET (E_{FRET}) depends on the separation distance (r) between the donor-acceptor and the characteristic distance called Förster radius (R_0) that depends on the relative structural orientation of the involved species:

$$E_{FRET} = \frac{1}{1 + ({}^{r}/_{R_0})^6}$$

For effective energy transfer, R_0 should typically ranges from 2–7 nm; therefore, making FRET a suitable technique to study the biomolecular level interactions. Since it determines the length scale of the interaction it is a crucial parameter to consider while choosing a donor-acceptor pair.

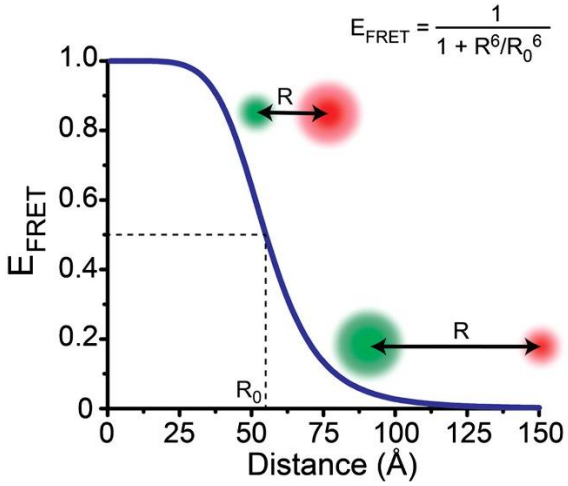

Figure 10: FRET efficiency as a function of donor-acceptor distance

A plot of the FRET efficiency (E_{FRET}) versus the distance (R) between a donor fluorophore (green) and an acceptor fluorophore (red) for the R_0 of 55 Å. When R < R0, E_{FRET} > 0.5; when R = R0, E_{FRET} = 0.5; and when R > R0, E_{FRET} < 0.5. Reprinted from [128]. CC BY 4.0.

The principle of FRET can be applied to live-cell imaging by combining it with a range of confocal microscopy-based techniques to quantify the molecular interactions. However, many of these techniques face drawbacks in terms of donor photobleaching and contaminated signal due to bleedthrough. Therefore, the measurement of FRET, based on the change in the fluorescence lifetime of donor was applied in the form of fluorescence lifetime imaging microscopy (FLIM)[127]. Since fluorescence lifetime measure is exclusively dependent on energy transfer from the donor molecule, it helps to overcome a lot of previously mentioned drawbacks associated with intensity-based techniques. The fluorescence lifetime (τ) is the average amount of time that a molecule spends in the excited state upon absorption of a photon of light. The presence of the acceptor causes donor to acceptor energy transfer and speeds up the return of the excited state electrons to the ground state. This is reflected in terms of the decreased fluorescent lifetime of the donor in the presence of the acceptor (τ_2) as compared to the donor alone lifetime (τ_1). FLIM enables the spatial mapping of FRET exhibiting biomolecules by recording their lifetime distribution in a cell. FRET efficiency can be expressed in terms of lifetimes:

$$E_{FRET} = \frac{\tau_1 - \tau_2}{\tau_1}$$

The measurement of fluorescence lifetime can be done in the frequency domain or in the time domain. In the frequency domain FLIM, the specimen is excited with sinusoidally modulated light with an angular frequency that is reciprocal to the fluorescence lifetime to be measured. Consequently, this leads to the re-emission of sinusoidally modulated fluorescence at the same frequency with a reduced relative modulation depth (M) and shifted phase (Δφ). These quantities can be used to calculate the phase-lifetime and the modulation-lifetime respectively. The fluorescence lifetime measurements can be carried out in the time domain as well. Here, the fluorescence lifetime is directly measured by the excitation of the donor fluorophore in the specimen with a short pulse of light. This results in the

fluorescence emission intensity profile that shows temporal exponential decay, from which the lifetime can be estimated[126].

Since the biological samples often have a mixture of multiple interacting molecular species, each resolvable volume element contains molecules in different biochemical states. Therefore, single lifetime estimates at each pixel of the sample image representing a single exponential do not suffice to accurately describe the complex decay. The lifetimes and fractions of each species should be resolved to obtained a multiexponential function[129]. This forms the basis of Fourier-based global analysis method of time-domain lifetime data (Figure 11). Here, the decay model is fitted as biexponential (based on varied proportions of interacting and non-interacting molecules) to estimate the populations and properties of interacting and non-interacting molecules (bound and unbound protein states) in cells[130]. The system is modelled as a mixture of two molecular species, free donor and donor-acceptor complexes, each with associated fluorescence decay characteristics. If the individual fluorescence decays are monoexponential, then their fluorescence kinetics can be precisely described by a biexponential fit.

In this method, single photon counting curves obtained as a function of time are extracted from several data sets containing donor-only samples and donor-acceptor samples. To increase the accuracy of fit, low photon intensity pixels are excluded from the analysis. Here, the parameters associated with the instrument response function (IRF) are extracted from the data itself (Fourier transform of the average of the data curves); thereby avoiding the use of separate reference measurements. The Fourier coefficient of the *n*th harmonic (R_i^n) is calculated for every pixel (i) from the histogram of photon counts for all the donor-only and donor-acceptor images. The distribution of $R_{n,1}$ of the donor-only data is estimated by a weighted mean and standard deviation of the real and imaginary parts. A straight line is fit through above threshold donor-acceptor points R_i^n using following equation[130]:

$$ImR_n^i = v_n ReR_n^i + u_n$$

The lifetimes τ_1 and τ_2 can be deduced from v_n and u_n as a function of the angular frequency of the excitation pulse (ω) and the chosen harmonic (n). From this, the fractional fluorescence intensities α^i of the interacting species (shorter lifetime) can be calculated in each pixel (i):

$$\alpha^i = \frac{n\omega(\tau_1 + \tau_2)ReR_n^i + (n^2\omega^2\tau_1\tau_2 - 1)ImR_n^i - n\omega\tau_2}{n\omega(\tau_1 - \tau_2)}$$

In comparison to the previously applied methods in the literature[131,132], above described method can be applied to low signal-to-noise ratio data, since all photon counts of multiple images are considered simultaneously. Therefore, Global analysis significantly improves the precision of lifetime estimations and enables the accurate quantitative understanding of biomolecular interactions.

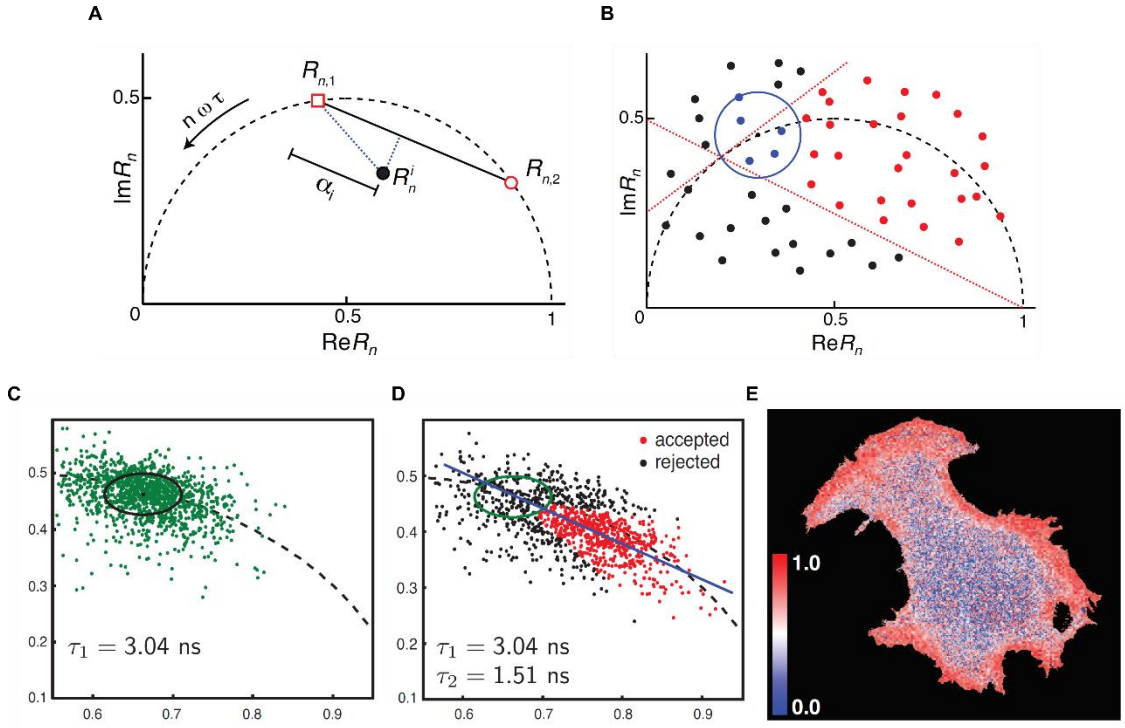

Figure 11: Global analysis of the FLIM data

(A) Phasor plot with the semicircle representing values of the monoexponential lifetimes and the straight-line representing possible mixtures of two monoexponential species. Global analysis estimates the straight line from the data and the intersections with the semicircle ($R_{n,1} and\ R_{n,2}$). For a random data point (R_n^i), the interacting fraction is given by the projected distance to $R_{n,1}$. **(B)** The imaginary parts of the first harmonic of the FLIM-data are plotted against the corresponding real parts. From donor-only data, a Gaussian distribution of the donor Fourier components is estimated and plotted as a blue contour. To filter the noise, points outside the red straight lines are rejected. Black circles: rejected points, blue circles: donor points, red circles: accepted points. **(C)** Phasor plot of experimental data showing donor-only (EGFR-YFP) estimated Gaussian distribution (green). **(D)** Phasor plot of data from donor/acceptor samples, with filtered points (red). The straight line represents a linear fit to the accepted data from which the two lifetimes are estimated. **(E)** The fraction of phosphorylated EGFR-YFP estimated by global analysis. Reprinted from [130]. Copyright © 2009 Optical Society of America.

1.5 EGFR-PTP interdependence

1.5.1 ROS mediated coupling between EGFR and PTPs

Ligand induced EGFR phosphorylation is a precursor to the activation of signaling molecules and secondary messengers responsible for diverse cellular functionalities. EGFR activity dependent ROS production and regulation of PTP activity by cysteine oxidation was independently well established by multiple studies as elaborated in previous sections. However, the direct evidence for the PTP oxidation mediated signal propagation of EGFR was lacking for a long while. In 2003, Reynolds *et al.* reported evidence of EGFR coupling to PTPs by ROS induced inhibition[101]. They demonstrated the involvement of PTP activities from the PM and the cytosol in maintaining the EGFR inactive state by treating cells with H_2O_2 to observe a rapid phosphorylation of EGFR on the PM as well as on the endomembranes as an effect of PTP inhibition. Conversely, when the cells were treated with EGF-attached beads, the phosphorylation was only observed at the PM leaving the endocytosed pool of EGFR inactive; indicating localized ROS production at the PM responsible for the inactivation of nearby PTPs. The microinjection

of catalase (H_2O_2 scavenger) to EGF treated cells hampered the spread of EGFR phosphorylation to varied proportions across the cell population as a function of catalase expression in the individual cells. The finding was substantiated by the treatment of cells with PTP inhibitors like pervanadate which resulted in the rapid phosphorylation of EGFR.

Further on, they proposed a model consisting of the EGFR-PTP reaction network to study the regulatory feedbacks in the system. The model was based on following assumptions: (1) EGFR phosphorylation is a bimolecular reaction between two receptors. Upon phosphorylation, the basal kinase activity (α_1) is enhanced by the factor (α_2/α_1). (2) The rate of PTP inhibition is proportional to the number of phosphorylated receptors since it is the principal species that causes EGF dependent PTP oxidation. The rate of PTP reduction is assumed constant. The reaction network was then transformed into chemical kinetic equations and solved for steady states in the absence of stimulus. The steady states were found to be dependent on three parameters: (1) the enhancement of kinase activity on receptor phosphorylation (α_2/α_1); (2) the ratio of maximal phosphatase activity to maximal kinase activity (P/K) and (3) the ratio of the maximal rate of phosphatase inhibition to the rate of phosphatase reactivation (I/R).

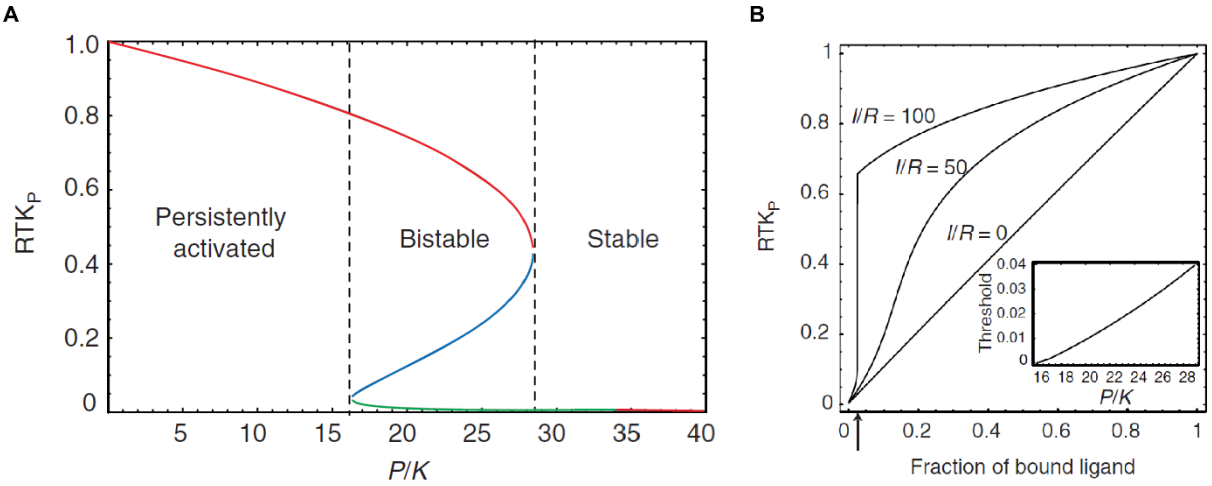

Figure 12: Theoretical prediction of RTK and PTP activity dynamics

(A) Fraction of phosphorylated RTK (RTK_p) as a function of relative PTP to RTK activity (P/K). Green (resting) and red (activated) lines are steady states, blue lines are unstable saddle point. The system is bistable in the zone where red and green lines coincide. Parameters: I/R = 100, $\alpha_2/\alpha_1 = 10$. **(B)** Calculated growth factor response curves for RTK activity at different coupling of PTP inhibition to RTK activation (I/R). Fraction of phosphorylated RTK (RTK_p) is plotted against fraction of ligand bound RTK. Reprinted from [101] with permission. Copyright © 2003, Springer Nature.

Such a system has been shown to adapt one of the following modes[2]: (1) a stable steady state at low phosphorylation of receptor (2) a stable steady state at high phosphorylation of receptor or (3) a bistable state, in which the phosphorylation of the receptor can be either high or low, depending on the starting conditions (Figure 12A). In a bistable state, a local perturbation (ligand stimulus) can trigger the system from a low to high (activated) state[101,133]. According to the model, a bistable state could be achieved in the system under consideration because the following minimum requirements were met: (1) the rate of maximal phosphatase inhibition exceeds the rate of phosphatase reactivation (I>R): the rate of PTP inhibition by hydrogen peroxide has been measured to be 10–100 times faster than the rate of

reactivation[102]; (2) kinase activity of the receptor increases on phosphorylation ($\alpha_2 > \alpha_1$): the catalytic activity of RTKs has been reported to be 3–100 times greater upon phosphorylation[134,135] and (3) the maximal PTP activity is greater than the maximal kinase activity (P>K): the catalytic activity of PTPs is 10–1,000 times higher than that of RTKs[136,137].

The model was further improved by introducing various levels of PTP inhibitions to study the effect of PTP-EGFR coupling strength on EGFR signal propagation. Thereby, EGF dose response curves were calculated for the system with different values of I/R with constant values of the other parameters (Figure 12B). At I/R equal to zero, no PTP inhibition was accomplished by EGFR activity dependent cysteine oxidation, and EGFR phosphorylation showed a graded response to EGF binding. At high I/R, the system operated in bistable regime and responded promptly, proving stronger coupling. The theoretical deductions were experimentally verified in EGFR expressing MCF7 cells, treated with ascending cumulative doses of EGF. A steep EGFR phosphorylation response was observed at a threshold of EGF binding, demonstrating the amplification of EGFR phosphorylation even at low ligand occupancy. However, the treatment of cells with NOX-inhibitor diphenyleneiodonium (DPI) intended to reduce the ROS produced by EGFR activation yielded linear phosphorylation response as a consequence of weaker coupling between EGFR and PTP. This study proposed the feedback loop between activities of EGFR and PTPs coupled through ROS production.

1.5.2 RPTPγ, RPTPη and TCPTP as major dephosphorylating activities against EGFR

Screenings based on bait-pray assays, enzymatic assays of purified proteins and biochemical assays of cell lysates have identified a number of PTPs that dephosphorylate EGFR. However, in order to determine the collective phosphorylation dynamics of EGFR it was necessary to characterize the primary regulatory interactions with PTPs. By using opposite genetic perturbations in terms of PTP expression levels (siRNA induced knock-down or ectopic expression), Stanoev *et al.* identified non-redundant PTPs that have the strongest effect on EGFR dephosphorylation[138]. Fluorescence microscopy to image phosphotyrosine levels of exogenous EGFR in MCF7 cells enabled the revelation of the causal interactions that lead to EGFR regulation.

After probing 55 PTPs, 5 PTPs performed optimally as negative regulators of EGFR phosphorylation considering the performance in both siRNA as well as ectopic expression-based screening (Figure 13). These were PM bound RPTP-α/γ/η (*PTPR-A/G/J*), ER-associated TCPTP (*PTPN2*) and cytosolic/nuclear localized DUSP3. Further analysis of the specific activities of these PTPs over the timeframe of EGFR signaling proved RPTP-γ/η and TCPTP as the strongest regulators of EGFR phosphorylation.

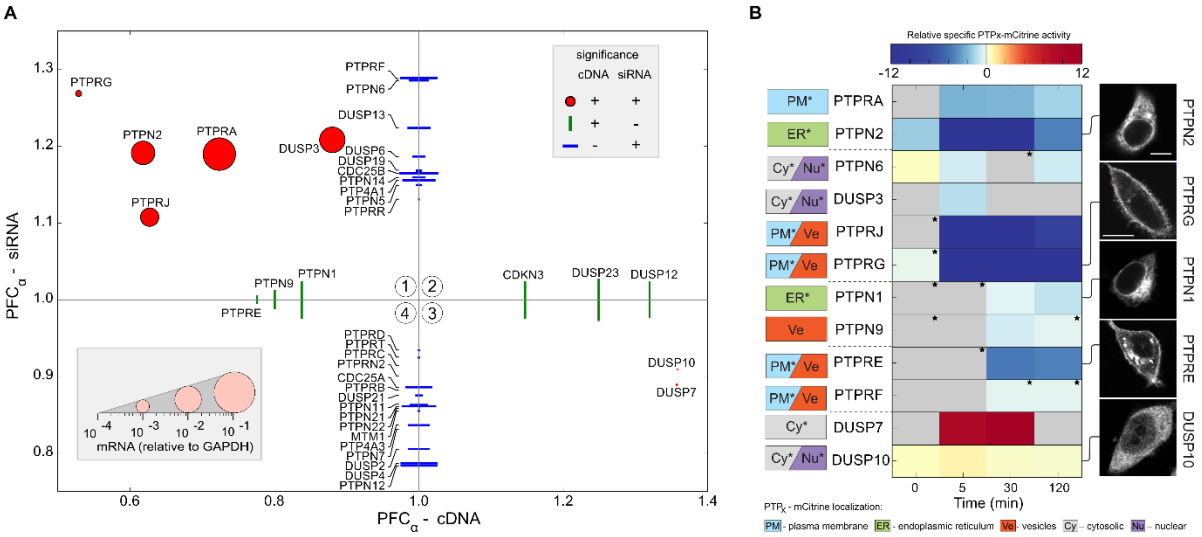

Figure 13: Identification of major PTP activities against EGFR

(A) Scatterplot showing median EGFR phosphorylation fold change (PFC) upon siRNA knockdown and ectopic expression of PTPs post 5 mins saturating EGF stimulus. Red dots indicate significant PFC upon both of the perturbations; blue lines and green lines only upon knockdown or ectopic expression respectively. **(B)** Relative specific PTP activities on EGFR at indicated time points upon pulsed saturating EGF treatment. Reprinted from [138]. CC BY 4.0.

1.5.3 Involvement of EGFR and PTPs in cancers

Since EGFR signaling is crucial to many metabolic processes and cell proliferation networks, it has also been a driver of tumorigenesis in plenty of lung and breast cancers. Most of these cancers exhibit incessant activation of EGFR as a consequence of overexpression, mutations/absence of the structural domains (e.g., L858R) or hampered inhibitory mechanisms that regulate the activation in healthy cells[139]. Examples of such conditions include head-neck squamous cell carcinoma, glioblastoma and non-small cell lung cancer (NSCLC); in which one or multiple mechanisms of EGFR regulation and signaling are hampered. Apart from mere EGFR activation dependence, these cancers are also accompanied by alteration in signaling dynamics that can lead to enhanced proliferation or survival. This has been observed in the colonies of NSCLC, where accelerated clathrin-mediated endocytosis by the activation of dynamin1 causes increased EGFR recycling and upregulated AKT signaling to result in cell survival[140]. In some of the cases, mutations in CBL binding tyrosine site 1045 (Y1045) on the intracellular EGFR domain alter the rate of EGFR degradation resulting in constitutive signaling[141]. Conversely, mutations can also be present in the extracellular domain (e.g., glioblastoma) leading to ligand-independent receptor activation[142].

The therapeutic approaches however have mostly centered around the direct restraining of EGFR activation by competitive binding at the ATP-binding pocket, hindrance to ligand binding with tyrosine kinase inhibitors (e.g., gefitinib and imatinib) or monoclonal antibodies (e.g., cetuximab and panitumumab). These methods have shown limited success in terms of reduced cell proliferation; however, in the long run they are often accompanied by drug resistant mutations[143]. The target directed approaches seem to fail also because of the ability of the cancer cells to reprogram the signaling events as an alternative to inhibitor-blocked signaling pathways. Many of these approaches look at the EGFR-mediated cell survival and proliferation as a sole linear signaling cascade that relies on the upstream

activation of the receptor and signal distribution to the downstream molecules. However, they disregard the active role of PTPs in the spatiotemporal coordination of EGFR response properties that decide the signaling fate. In this regard, PTPs present themselves as an interesting nevertheless untapped league for the therapeutic development in RTK-signaling associated cancers.

Amongst cytosolic PTPs, SHP2 plays a crucial role in RTK activation and therefore has been essential for transformation initiated by RTK mutation and amplification. It has been linked to PI3K activation and thereby Ras/ERK regulation. In the context of EGFR, SHP2 negatively regulates PI3K activation by dephosphorylating PI3K binding sites on GRB2-associated-binding protein 1 (GAB1). This can hinder the PI3K/Akt activity and therefore interfere with cell survival. In triple-negative breast cancer (TNBC) cell lines, *PTPN11* deficiency leads to decreased expansion and cell motility[144]. However, in conditions like Metachondromatosis (MC) splice-site mutations in *PTPN11* are observed[145]. ER-PTP-TCPTP is reported to be a major regulator of EGFR signaling duration. Evidently, deficiency of *PTPN2* gene has been associated with upregulated phosphorylation dependent signalling to promote growth and survival. TCPTP has been proved to be a tumor suppressor in T cell acute lymphoblastic leukemia (T-ALL)[146] and a few of the solid malignancies, like breast cancer[147]. R-PTPs like RPTPδ by its interactions with STAT3[148], RPTPρ with Paxillin[149], RPTPμ and RPTPκ by regulating β-catenin[150,151] have been shown to supress signaling associated with the mentioned oncogenes. Apart from its proven role in cell growth suppression, RPTPη has been also linked to negative regulation of VEGFR in endothelial cells by blocking cell proliferation and vascularization of tumors[152].

In the case of *PTPRG*, the associated chromosomal region (3p14-21) has been commonly found to be deleted in cancerous tissues[153,154]. Promoter methylation or loss of heterozygosity was also seen in primary gastric tumors, precancerous adenomas and hyperplastic polyps[155]; making it not only a candidate tumor suppressor but also a diagnostic marker worth investigation. Although the direct evidence for RPTPγ being a tumor suppressor is scarce, the role of RPTPγ in the regulation of EGFR signaling response is well established. RPTPγ has been shown to govern the ligand sensitivity of EGFR and might therefore play a key role in the malignancies that result from elevated EGFR activity. Such a regulation is observed in nasopharyngeal carcinoma (NPC), where RPTPγ controls the signaling from Y1068 and Y1086 sites on EGFR to restrict Akt activation and subsequent down-regulation of pro-angiogenic cytokines like VEGF, IL6 and IL8[156]. In childhood acute lymphoblastic leukemia (ALL), RPTPγ has been shown to suppress ERK1/2 phosphorylation caused by mutant RAS[157,158]. *PTPRG* methylation and gene silencing is frequently observed in pre-metastatic cells, suggesting its function in curbing the metastatic spread as well[156]. Considering its wide spanning involvement from adenoma stage to metastasis, frequent loss of expression in tumors and interregulation with one of most potent oncogenes-EGFR makes RPTPγ a crucial yet unexplored target for cancer therapeutics.

Objectives

As a result of their distinct cellular localizations and enzymatic interactions, PTPs act on different regulatory aspects of EGFR signaling. Two of the PTPs that are at the forefront of this regulation are RPTPγ and TCPTP[138]. PM-based RPTPγ shares a spatial compartment with EGFR and exhibits its catalytic activity towards the EGFR autocatalytic site. This presents it as a probable regulator of EGFR activation that can affect the sensitivity of EGFR towards the changes in the growth factor environment. Given the well-known role of EGFR as an oncogene and the observations about the lack of RPTPγ expression in tumor samples, it is fundamental to investigate how the interaction between RPTPγ and EGFR regulates the physiological response of EGFR to growth factors. However, around 2 orders of magnitude higher phosphatase activities of PTPs than kinase activities of RTKs[136,137] made us ask how RPTPγ suppresses EGFR activation and also let it signal to carry out normal cell growth functions? To understand how these opposed features are established on a molecular level is the main objective of the thesis.

I address the following aspects as a part of this research study:

1. A precursor to understanding the function of RPTPγ is to investigate whether there is a direct interaction between RPTPγ and EGFR that might form a basis of their mutual-regulation. The spatiotemporal and cell-compartmental nature of the interaction is investigated to establish its relation with EGFR activity.

2. The role of RPTPγ in the activation and growth factor response of EGFR is examined by inducing acute genetic perturbations in RPTPγ expression level. The goal here is to relate the RPTPγ expression with the changes in growth factor sensing and signaling of EGFR in the context of attaining tumorigenic properties.

3. Simultaneously it is crucial to identify the aspect of the regulation of RPTPγ by EGFR activation. Along these lines, the possibility of the redox regulation of RPTPγ is inspected. If such a regulation takes place, when and where does it happen? This requires development of a suitable imaging technique that can spatially differentiate the oxidized fraction of protein in a living cell.

4. How does the TCPTP expression affect the EGFR growth factor response, and whether the spatial spread of TCPTP results in differential regulation of its subpopulations depending on EGFR activity?

Taking these questions into account, we set out to explore the modes of mutual-regulation between EGFR-RPTPγ/TCPTP activities that maintain EGFR in ligand-perceptive mode as well as facilitate its signaling response to growth factors.

Materials and methods

3.1 Materials

3.1.1 Reagents

2'-deoxyadenosine-5'-triphosphate (dATP)	Invitrogen™ Life Technologies
2-Log DNA ladder	New England Biolabs
Acetic acid	Sigma-Aldrich®
Ampicillin sodium salt	SERVA Electrophoresis GmbH
Atto590azide	Atto Tec
Bromophenolblue	Sigma-Aldrich®
Chameleon® Duo Pre-stained Protein Ladder	LI-COR Biosciences
Complete, Mini, EDTA-free Protease Inhibitor, cocktail tablets	Roche Diagnostics
Copper (II) Sulfate (CuSO4) click chemistry grade	Jena BioScience
Dimedone	Sigma-Aldrich®
Dimethyl sulfoxide (DMSO)	SERVA Electrophoresis GmbH
Dithiothreitol (DTT)	Fluka® Analytical
DYn-2	Cayman chemicals
Epidermal growth factor (EGF)	Sigma-Aldrich®
Ethanol	J.T.Baker
Ethylenediaminetetracetic acid (EDTA)	Fluka® Analytical
FuGENE® 6	Promega
Glycerol	GERBU Biotechnik GmbH
Glycine	Carl Roth GmbH
Histofix	Carl Roth GmbH
Hoechst 33342	Thermo Fisher Scientific
Hydrogen peroxide (H_2O_2)	Merck
Isopropanol	J.T.Baker
Kanamycin sulfate	GERBU Biotechnik GmbH

Lipofectamine 3000	Thermo Fisher Scientific
Magnesium chloride $MgCl_2$	Fluka® Analytical
Methanol	AppliChem GmbH
N,N,N',N'-Tetramethylene-diamine (TEMED)	Sigma-Aldrich®
N-Ethylmaleimide (NEM)	Sigma-Aldrich®
Phosphatase Inhibitor Cocktail 2	Sigma-Aldrich®
Phosphatase Inhibitor Cocktail 3	Sigma-Aldrich®
Potassium chloride KCl	Fluka® Analytical
Sodium chloride (NaCl)	Fluka® Analytical
Tris(2-carboxyethyl) phosphin (TCEP)	Sigma-Aldrich®
Tris(benzyltriazolylmethyl)amine (TBTA)	Carl Roth GmbH
Tris-base	Carl Roth GmbH
Tris-HCl	J.T.Baker
Tritox X-100	SERVA Electrophoresis GmbH
Tween 20	SERVA Electrophoresis GmbH
UltraPure™ Agarose	Thermo Fisher Scientific

3.1.2 Buffers and cell media

DMEM/F12	Gibco® LifeTechnologies
DNA sample buffer	50% glycerol 0.1% Orange F 0.1 M EDTA
Dulbecco's Modified Eagle's Medium (DMEM)	PAN™ Biotech
Dulbecco's Phosphate Buffered Saline (DPBS)	PAN™ Biotech
Hank's Buffered Salt Solution (HBSS)	PAN™ Biotech
HT29 growth Media	Ham's F12 + 10 % FBS, 1 % NEAA and 1% L-Glutamine

HT29 starvation media	Ham's F12 + 0.5 % FBS, 1 % NEAA and 1% L-Glutamine
Ham's F12 culture media	PAN^{TM} Biotech
Imaging medium	DMEM without Phenol red + 25 mM HEPES
Intercept blocking buffer	LI-COR Biosciences
MCF10A growth Media	DMEM/F12 + 5% horse serum, 20 ng/ml EGF, 500 ng/ml hydrocortisone, 100 ng/ml cholera toxin and 10 µg/ml insulin
MCF10A starvation media	DMEM/F12 + 20 ng/ml EGF, 500 ng/ml hydrocortisone, 100 ng/ml cholera toxin and 10 µg/ml insulin
MCF7 growth Media	DMEM + 10 % FBS, 1 % NEAA and 1% L-Glutamine
MCF7 starvation media	DMEM + 0.5 % FBS, 1 % NEAA and 1% L-Glutamine
MOPS SDS running buffer	Thermo Fisher Scientific
OptiMEM	Gibco® LifeTechnologies
Paraformaldehyde (16%) EM-grade	Thermo Fisher Scientific
RIPA buffer	50 mM Tris (pH 7.5), 150 mM NaCl, 1 mM EDTA, 1%IGEPAL, 0.25% Na-deoxycholate
SOC medium	20 g/l Bacto-Trypton 5 g/l Bacto-yeast extract 0.5 g/l NaCl 2.5 mM KCl 10 mM MgCl2 20 mM glucose
TAE buffer	40 mM Tris-acetate 1 M EDTA 20 mM NaOAc
TBS	100 mM Tris-HCl

	150 mM NaCl
Wet transfer blotting buffer	25 mM Tris-base
	192 mM glycine
	20% methanol
XT sample buffer 4X	Bio-rad

3.1.3 Enzymes

High-Fidelity Restriction enzymes	New England Biolabs
Q5® High-Fidelity DNA Polymerase	New England Biolabs Inc.
T4-DNA ligase	Invitrogen™ Life Technologies
T4-DNA polymerase I	New England Biolabs

3.1.4 Analytical and purification kits

Micro BCATM Protein Assay Kit	Thermo Scientific
NucleoBond® Xtra Midi Plus EF	Macherey-Nagel
Nucleoseq Columns	Macherey-Nagel
Roti®-Prep Plasmid MINI	Carl Roth GmbH
ZymocleanTM Gel DNA Recovery Kit	Zymo Research

3.1.5 Antibodies

Primary antibodies:

Anti-Cysteine Sulfenic Acid	Merck
goat anti-GFP (ab6673)	Abcam
mouse anti-Akt (pan, 2920)	Cell Signaling Technology
mouse anti-ERK1/2 (Ab366991)	Abcam
mouse anti-GAPDH (CB1001)	Merck
mouse anti-GFP (632681)	Living colors, clonetech
rabbit anti-EEA1 (3288)	Cell Signaling Technology
rabbit anti-EGFR (4267)	Cell Signaling Technology

rabbit anti-phospho Akt (Ser473, 9271)	Cell Signaling Technology
rabbit anti-phospho EGFR (pY1068, 3777)	Cell Signaling Technology
rabbit anti-phospho ERK-1/2 (Thr/Tyr 202/204, 9101)	Cell Signaling Technology
rabbit anti-Rab11a (2413)	Cell Signaling Technology
rabbit anti-Rab7 (9367)	Cell Signaling Technology

Secondary antibodies for western blot:

IRDye 680 donkey anti-mouse IgG	LI-COR Biosciences
IRDye 680 donkey anti-rabbit IgG	LI-COR Biosciences
IRDye 800 donkey anti-mouse IgG	LI-COR Biosciences
IRDye 800 donkey anti-rabbit IgG	LI-COR Biosciences

Secondary antibodies for immunofluorescence:

Alexa Fluor 568 donkey anti-rabbit IgG	Life Technologies
Alexa Fluor 647 chicken anti-rabbit IgG	Life Technologies
Alexa Fluor 647 donkey anti-goat IgG	Life Technologies

3.1.6 Plasmids

CBL-mCherry	Encoding human c-CBL with C-terminally fused mCherry
EGFR-mCherry	Encoding human EGFR with C-terminally fused mCherry
EGFR-mCitrine	Encoding human EGFR with C-terminally fused mCitrine
EGFR-mTFP	Encoding human EGFR with C-terminally fused mTFP
pcDNA3.1+	Invitrogen

pSpCas9(BB)-2A-GFP (PX458)	Encoding Cas9 from S. pyogenes with 2A-EGFP
PTB-mCherry	Encoding human phosphotyrosine binding domain (PTB) with C-terminally fused mCherry
TCPTP-mCitrine	Encoding human TCPTP with C-terminally fused mCitrine
TCPTP-mTFP	Encoding human TCPTP with C-terminally fused mTFP
RPTPγ-mCherry	Encoding human RPTPγ with C-terminally fused mCherry
RPTPγ-mCitrine	Encoding human RPTPγ with C-terminally fused mCitrine
RPTPγ-mTFP	Encoding human RPTPγ with C-terminally fused mTFP
paGFP-RPTPγ	Encoding RPTPγ with C-terminally fused paGFP
tagBFP-Rab11a	Encoding human Rab11a with N-terminally fused tagBFP

3.1.7 Equipment

BD FACSAria™ Fusion Cell Sorter	BD Biosciences
Cell scraper	Sarstedt AG and Co.
Centrifuge (5415R and 5810R)	Eppendorf
Dynabeads™ Protein G for Immunoprecipitation	Invitrogen™ Thermo Fischer
DynaMag-2 magnetic rack	Thermo Fischer
Eppendorf safe-lock tubes	Eppendorf
Falcon tubes	BD Falcon™
Heatable magnetic stirrer IKMAG®RCT	IKA Labortechnik
Heating block	Grant Instruments
Immobilon-FL PVDF	Millipore, Merck KGaA

Infinity II Preparative LC-MSD System (1260)	Agilent Technologies
LabTek chambers (4-well and 8-well)	Nunc Thermo Fischer
Leica SP8 and FALCON	Leica Microsystems
Mini and Midi agarose gel chamber	Carl Roth GmbH
Mini Trans-Blot® Cell	Bio-rad
Multiskan Ascent Microplate Reader	Thermo labsystems
Nanodrop ND-1000 spectrophotometer	Peqlab Biotechnologie GmbH
NUAIRE™ Cellgard class II biological safety cabinet	Integra Biosciences
NUCLEODUR® C18 gravity column	Macherey-Nagel
NuPage™ 4-12% Bis-Tris Mini-Gel	Invitrogen™ Thermo Fischer
Odyssey Infrared Imager	LI-COR Biosciences
PCR cycler	Eppendorf
Pipetboy accu 2	Integra Biosciences
Tissue culture flask (T25, T75)	Sarstedt AG and Co.
Tissue culture plates (6-well, 24-well, 96-well)	Sarstedt AG and Co.
Typhoon Trio Variable Mode Imager	GE Healthcare
Vacuum centrifuge	Eppendorf
Vi-Cell™ XR cell viability analyzer	Beckman Coulter, Inc.
Western blot incubation boxes	LI-COR Biosciences
XCell Sure-Lock Mini-Cell Electrophoresis System	Thermo Fischer

3.1.8 Software

Cellpose	https://www.cellpose.org/
Fiji	http://fiji.sc/Fiji
GraphPad Prism 9	GraphPad Software Inc.
Inkscape	http://inkscpape.org
Leica Application Suite X	Leica MICROSYSTEMS
MATLAB R2016a-R2021a	Mathworks

DNASTAR Navigator v2.2.1.1	DNASTAR
Multiscan Ascent Software Version 2.6	ThermoElectron Coorperation
Python 3.4	Python Software Foundation
IGOR Pro 6.3	WaveMetrics

3.2 Methods

3.2.1 Molecular Biology

Polymerase chain reaction (PCR)

Amplification of the target DNA sequences was performed by using specific primer pairs in polymerase chain reaction (PCR) with Q5® High-Fidelity DNA Polymerase. For a total of 50 µl reaction mixture, the following reagents were mixed in a PCR tube maintained constantly over ice:

Reagent	**Volume (µl)**
5X Q5 reaction buffer	10
dNTPs (10mM)	1
Forward Primer (10 µM)	2.5
Reverse Primer (10 µM)	2.5
Template DNA (~10 ng)	X
Q5 High-Fidelity DNA Polymerase	0.5
Nuclease-free water	to 50 ul

Table 1: PCR batch reaction with Q5® High-Fidelity DNA Polymerase

The mixture was gently mixed and transferred to a PCR machine. The following thermocycling conditions were used:

Step/Cycle	**Temperature (ºC)**	**Time (s)**
Initial denaturation (1 cycle)	98	30
Denaturation (35 cycles)	95	10
Annealing	50-72*	20
Extension	72	30/kb
Final extension	72	120
Hold	4	-

Table 2: Thermocycling-protocol for Q5® High-Fidelity DNA Polymerase

*Annealing temperature depends on composition of nucleic acid bases in the primers of choice.

Agarose gel electrophoresis

Separation of the DNA-fragments by their nucleic acid size was performed by agarose gel electrophoresis. The gels were prepared with TAE buffer supplemented with DNA binding dye RedSafe™ DNA stain 5 µl/100 ml. The PCR-derived samples diluted in 10X loading buffer were loaded on 1%-2% (w/v) agarose gels. The gel electrophoresis was performed for 30 min at 120 V in a chamber filled with 1xTAE buffer. A 2-log DNA ladder was used for the size estimation of DNA fragments. The

DNA-fragments of interest were cut out from the gel and purified with Zymoclean™ Gel DNA Recovery Kit according to the manufacturer's instructions.

Restriction-digestion

To cut the double-stranded DNA at specific nucleotide sequences (restriction sites) High-Fidelity (HF®) restriction endonucleases were utilized. Restriction mixture (50 µl) was prepared in the following way and incubated for 3 h at 37 °C:

Reagent	**Volume (µl)**
CutSmart® Buffer (10X)	5
HF® restriction endonucleases	1/each enzyme
Template DNA (~5 µg)	X
Nuclease-free water	to 50 µl

Table 3: Restriction-digestion of a DNA-fragment

Dephosphorylation

Self-ligation of the digested vector was prevented by the dephosphorylation of its 5'-end. 1 µl of Calf Intestinal Alkaline Phosphatase (CIAP) was added to the digestion sample and incubated for 15 min at 37°C.

DNA-ligation

DNA-ligation was employed to obtain desired cloning product out of digested fragments along with an insert of choice (if needed). T4-DNA ligase was used to covalently connect the 3'-hydroxy- and 5'phosphate-ends of double-stranded DNA with two phosphodiester bonds to achieve DNA ligation. A ratio of 1:4 of vector DNA to insert DNA was used for the ligation reaction. The required amount of DNA insert was calculated as follows:

$$Amount\ of\ the\ insert\ (ng) = \frac{amount\ of\ the\ vector\ (ng) \times insert\ size\ (bp)}{vector\ size\ (bp)}$$

The calculated amount of insert DNA was mixed with the vector DNA, 4 µl of 1X T4-DNA ligase buffer, 1 µl of T4-DNA ligase and nuclease free water to get a total volume of 20 µl. The reaction mixture was incubated for 1 hr at the RT.

Site-directed mutagenesis

Site-directed mutagenesis was used to create targeted changes like insertions, deletions and substitutions in double-stranded plasmid DNA. Mutagenic primers and annealing temperatures were customized according to the requirement with NEBaseChanger™ tool (https://nebasechanger.neb.com/). Q5® Site-Directed Mutagenesis Kit was utilized according to the manufacturer's protocol.

Transformation of chemical competent *E.coli* and plasmid extraction

Amplification of the plasmid of interest or ligation product was done by transforming it into *E. Coli*. For transformation, 50 µl of chemical competent XL 10-Gold *E. Coli*. cells were thawed on ice. Ligation

product mixture (5 µl) or plasmid DNA (1 µl), along with 1.75 µl of 2.25 M DTT were added to the cells and incubated on ice for 30 min. Cells were subjected to heat-shock in a water heating bath for ~45 s at 42 °C and immediately placed on ice for 2 min. SOC medium (200 µl) was added and the cells were incubated at 37°C for 1 h in an incubator-shaker at 200 rpm. Cells were centrifuged for 1 min at 13000 rpm, the supernatant was discarded and the pellet was resuspended in 100 µl SOC media. For the ligation mixture, the whole cell suspension was plated on LB agar plates containing an appropriate antibiotic (ampicillin or kanamycin) for selection. For plasmid DNA transformation 50 µl cell suspension was used for plating. LB agar plates were incubated overnight at 37°C. Single cell colonies of *E. coli* were picked from LB agar plates and the bacterial cultures were grown overnight at 37°C and 200 rpm in 5 ml antibiotic supplemented LB media (mini plasmid preparation) or 200 ml (midi plasmid preparation). Plasmids were extracted from the *E. coli* suspension and purified with NucleoBond® Xtra Midi EF kit according to the manufacturers' protocol.

3.2.2 DyTo: probe for imaging oxidized proteins

Synthesis of DyTo

The DyTo probe used for the PTP cysteine oxidation experiments was synthesized by in-house labelling of Dyn2 with atto590azide by using copper-catalyzed azide-alkyne cycloaddition (CuAAC) reaction[159]. The click chemistry grade reagents were used for the reaction without checking further purity. Stock solutions were frequently checked for the presence of precipitates or discoloration. The Cu^{+} catalyst needed for the reaction between the terminal alkyne of DYn-2 and azide group of atto590 is obtained from the reduction of $CuSO_4$ (Cu^{2+}) by TCEP. Cu^{+} stabilizing ligand TBTA is used to protect the ions from undergoing oxidation in the reaction mixture and achieve regioselectivity.

The reaction mixture was prepared by the addition of the following reagents in the mentioned order:

Reagent	**Concentration**
Atto590azide (in DMSO)	6 mM
$CuSO_4$ (in H_2O)	40 mM
TCEP (in H_2O)	40 mM
TBTA (in DMSO)	20 mM
DYn-2 (in DMSO)	18 mM

Table 4: Synthesis of DyTo

Between the addition of the subsequent reagents the reaction mixture was vortexed. Before the addition of TBTA, the mixture was incubated for the 5mins. The reaction was performed in a 2 ml microcentrifuge tube at the final reaction volume of 900 µl. The reaction was allowed to proceed overnight in dark on a shaking platform at room temperature.

Purification of DyTo

Upon the completion of the reaction, DyTo was purified from the unreacted material and the by-products on mass-directed preparative HPLC (infinity prep II, Agilent Series 1260, LC-MSD) using reversed-

phase C18 column (VP10/125 5 µm) with a constant flow of 20 mL/min. Water/Acetonitrile system was used as eluent- Solvent A: H_2O+0.1% v/v TFA, solvent B: CH_3CN+0.1% v/v TFA.

The DyTo fraction obtained from the HPLC was subject to reduced-pressure evaporation to get rid of the solvents and obtain the final product as magenta powder. The product identity was verified on mass spectrometer integrated with HPLC system. DyTo was stored at -20°C for long term storage and stock solution was prepared in DMSO whenever required.

3.2.3 Mammalian cell culture

Cell maintenance and seeding

Breast cancer cell line MCF7 was cultured in Dulbecco's modified Eagle's medium (DMEM) supplemented with 10% fetal bovine serum (FBS), 2 mM L-Glutamine and 1% nonessential amino acids (NEAA). MCF10A, non-malignant breast epithelial cells were grown in DMEM/F12 supplemented with 5% horse serum, 20 ng/ml EGF, 500 ng/ml hydrocortisone, 100 ng/ml cholera toxin and 10 µg/ml insulin. Human colorectal adenocarcinoma derived HT29 cells were cultured in Ham's F12 culture medium supplemented with glutamine and 10% FBS. All cells were grown at 37°C in 5% CO_2 and regularly checked for mycoplasma.

The cells were grown in T75-culture flask until they attained 70-80% confluency. For cell splitting, the cells were washed with PBS and detached with Trypsin-EDTA treatment. After 10min incubation at 37°C, the reaction was neutralized by adding fresh growth media to the culture flask. The cell number was counted with cell viability analyzer. Cells were seeded to desired culture flasks or plates with cell-density as per the experimental requirements. They were serum starved for at least 6 hrs prior to the experiment with respective culture media containing 0.5% FBS.

Transient transfection

MCF7 cells were transfected 24 hours prior to the experiment with the intended cDNA expression using FuGENE6. HT29 cells were transfected with Lipofectamine 3000 and subjected to culture media change 7 hrs after transfection. The cDNA dilutions and incubation timings for the transfections were according to the manufacturer's guidelines.

3.2.4 Gene knockout with CRISPR-Cas9

Cloning backbone for CRISPR guide RNA sequences (sgRNA) containing Cas9 from S. pyogenes, pSpCas9(BB)-2A-GFP (PX458) was a gift from Feng Zhang[160]. The oligonucleotides containing sgRNA were designed using web-based Broad institute genetic perturbation platform (https://portals.broadinstitute.org/gppx/crispick/public). The sgRNA sequences used to create CRISPR KO cell lines are as follows:

PTPRG exon 7: 5'-TCCACTATTTCGCTACACGG-3'

PTPN2 exon 6: 5'-AGGGACTCCAAAATCTGGCC-3'

CYBA exon 2: 5'-GTAGGCACCAAAGTACCACT-3'

The sgRNAs were cloned into the BbsI site of the pX458 expression vector as described previously. MCF7 cells were plated into 6-well dishes and transfected with 2 µg pX458 construct containing required sgRNA using FuGENE6. Cells were FACS sorted 24hrs post-transfection using GFP expression and single cells were sparsely seeded into 15cm culture dishes. Single clone derived colonies were picked and expanded in suitable culture plates with ascending surface area for subsequent cell-split (96 well- 48 well- 12 well- 6 well - T75 flask). Gene knockout was evaluated by western blot analysis. The antibody against RPTPγ-anti-P4, polyclonal rabbit IgG was a gift from M. Vezzalini[161].

3.2.5 Protein biochemistry

Cell Lysis

Cells seeded in 6-well plates (2×10^5 cells/well) were transfected and treated according to the experimental requirements. After stimulation, cells plates were placed on ice boxes and lysed with in-house prepared RIPA buffer supplemented with N-Ethylmaleimide (NEM), Complete Mini EDTA-free protease inhibitor and phosphatase inhibitor cocktail 2-3. Lysates were collected in pre-cooled tubes and separated from the cell pellet by centrifugation for 15 min, 13,500 rpm at 4°C. For long-term storage, the tubes containing lysate supernatants were flash frozen by immersion in liquid nitrogen and stored at -80°C.

Determination of the protein concentration in the lysates

Protein concentration in the lysates was measured by colorimetric detection using Micro BCA™ Protein Assay Kit, according to the manufacturer's protocol. The samples were prepared in a 96-well plate in which 4 µl of lysate was mixed with 80 µl BCA reagent mix and incubated for 45 min at 37°C. Absorbance of the protein samples was measured at 562 nm on the Multiskan Ascent Microplate Reader and their concentrations were calculated by interpolating them on the standard curve.

Immunoprecipitation

For immunoprecipitation, equal amount (mass) of protein (~100-150 µg) from the lysates were precleared with 10 µl Dynabeads Protein G magnetic beads to reduce non-specific binding and subsequently incubated with pull-down antibody, goat anti-GFP (ab6673, 1:200), overnight at 4°C on a rotating wheel. Later, samples were treated with 25 µl Dynabeads Protein G magnetic beads for 2 hrs at 4°C on a rotating wheel for the pull-down. The beads were washed 4 times with RIPA buffer and proteins were eluted in denatured form with 1X XT sample buffer (and DTT for reducing conditions) by heating them for 10mins at 90°C.

Separation of proteins by SDS PAGE

Equal amount of protein (~15-20 µg) from each lysate samples was mixed with 1X XT sample buffer (and DTT for reducing conditions) and denatured by heating for 10mins at 90°C. To separate the proteins in the lysate according to their molecular weights, they were loaded on precast 4-12% NuPAGE or in-house prepared 10 well, 1.5mm thickness Bis-Tris polyacrylamide gels. The electrophoresis was carried out at 200V constant voltage in XCell Sure-Lock Mini-chambers filled with MOPS buffer.

Western blotting and in-gel fluorescence

After size separation, the proteins were transferred from the polyacrylamide gel to a PVDF membrane by electroblotting. The transfer was performed in a Mini Trans-Blot® Cell at 100V constant voltage for 1.5 hrs. The chamber was filled with in-house prepared wet transfer buffer. To prevent overheating of the assembly, cold packs were immersed in the chamber and transfer was performed under constant magnetic stirring. Next, the PVDF membrane was blocked in Licor intercept blocking buffer at the room temperature for 1 hr. The Membrane was incubated overnight with primary antibodies at 4°C on a shaking platform at experiment dependent dilution ratio in Licor intercept blocking buffer (~1:1000-1:5000). Three washing steps were performed on the membrane with TBS-T buffer at 10 mins of time intervals. The membrane was then incubated for 1 hr with specific secondary antibodies diluted (1:10000) in TBS and subsequently subjected to TBS-T washing as before.

For PVDF membrane, the blot was scanned with the Odyssey Infrared Imaging System at 700nm and 800nm. Post background subtraction, the integrated protein band intensities were obtained for the further analysis in FiJi software. The protein signals were normalized by dividing the intensities of phosphorylated or oxidized proteins to corresponding total protein intensities; in the case of co-IP, the intensities of co-IP proteins were divided by the corresponding IP proteins. To detect the in-gel fluorescence, Bis-Tris gel was imaged on Typhoon Trio Variable Mode Imager. DyTo containing Atto590 label was excited using 532 nm laser and the fluorescence emission was detected with 610/30 BP filter.

3.2.6 Immunofluorescence

Cells were grown in 4 or 8-well Labteks and transfected as per the experimental requirements. After stimulation, the cells were fixed with 4% EM-grade paraformaldehyde in TBS (v/v) for 10 min. Cells were subsequently permeabilized with 0.2% Triton X-100 (v/v) for 8 min. The samples were incubated with Intercept blocking buffer at room temperature to reduce stray background staining. Next, they were treated with primary antibodies overnight at 4°C. The following morning, secondary antibodies were applied for 1 hr at room temperature. Primary and secondary antibodies were diluted in Intercept (TBS) Blocking Buffer. Three washing steps with 5 mins interval were performed following fixation, permeabilization, primary or secondary antibody incubation with TBS.

The extent of co-localization of the endosomal marker proteins (EMP): Rab11a, EEA1 or Rab7 with the protein of interest (POI): RPTPγ-mCitrine or EGFR-mCherry was computed in FiJi by defining ROIs in two channels (a set of EMP and POI under consideration) by intensity thresholding. Post background subtraction, first intensity thresholded mask was created in EMP channel marked by immunostaining against EMP. The second mask was created similarly in the POI channel from the fluorescence. The first mask was converted to a binary image and multiplied with the second image mask to calculate the areal overlap between two channels. To compute the fraction of the POI that showed co-localization, the integrated intensity from the overlapped area was normalized to the total integrated intensity of POI in the whole cell.

3.2.7 Confocal Microscopy

For fluorescence imaging experiments cells were seeded on 8-well (1.5×10^3 cells/well) or 4-well (3×10^3 cells/well) labteks, 48 hrs prior to the experiment. Whenever required, cells were transfected before 24 hrs and serum starved for at least 6 hrs. Confocal images were acquired using a Leica TSC SP8 microscope (Leica Microsystems, Wetzlar, Germany) equipped with an environment-control chamber (Life Imaging Services) that maintained the surrounding temperature at 37°C. The imaging was done with HC PL APO CS2 1.4 NA 63x oil objective and the pinhole was set to 1.7 Airy units. The following excitation wavelengths were used for proteins with fluorescent fusion tags/ labels: 514nm for mCitrine, 561nm for mCherry and Alexa Fluor 568, 458nm for TFP, 405nm for BFP and DyLight 405, for Atto Tec 590, 640nm for Alexa Fluor 647. Fluorescence emission was detected by hybrid detectors (HyD) restricted to: 524 to 560 nm for mCitrine, at 571 to 620 nm for mCherry and Alexa Fluor 568, 468 to 485nm for TFP, 415 to 450nm for BFP and DyLight 405, for Atto590, 655 to 690 nm for Alexa Fluor 647. Images were recorded in frame-by-frame sequential scanning mode with 80Hz scanning frequency and 512×512 pixels in 12-bit format.

3.2.8 Fluorescence lifetime imaging microscopy (FLIM)

Fluorescence lifetime measurements of EGFR-mCitrine, RPTPγ and TCPTP-mCitrine were performed at 37°C on a Leica SP8 using a 63×/1.4 NA oil objective. To detect the time domain FLIM, SP8 was equipped with a fast lifetime contrast module (FALCON, Leica Microsystems). Due to very short system deadtime (1.5 ns) the SP8 FALCON was capable of measuring one photon per pulse with each detector, allowing FLIM imaging at confocal speed. This enabled the live cell FLIM-imaging with reduced motion blur associated with compartmental movements in cells. Excitation of mCitrine was achieved using a pulsed white light laser at a frequency of 20 MHz and wavelength of 514 nm. Detection of fluorescence emission was restricted to 525 to 560 nm with HyDs. The photon collection was split amongst 2-3 HyDs with an AcoustoOptical Beam Splitter (AOBS) so as to increase the efficiency of photon acquisition and speed up the FLIM-imaging. Photons were integrated for a total of approximately 15-20 seconds per image (~200-300 photons/pixel sum of all detectors) using the FALCON system.

The donor count cell images obtained from the microscope were thresholded above the background fluorescence. Global analysis of FLIM-FRET images was performed as described in section (1.4.2) by a custom program implemented in Python[130]. The analysis produced the images with spatial distribution of the fraction of FRET-exhibiting donor (α). The method was used for the lifetime data analysis of the EGFR phosphorylation (PTB-bound fraction of EGFR-mCitrine: α_p) and PTP oxidation experiments. (DyTo bound fraction of PTP-mCitrine: α_{oxi}).

3.2.9 Imaging of EGFR phosphorylation upon EGF stimuli

Cells were transfected with EGFR-mCitrine, PTB-mCherry and RPTPγ/TCPTP-mTFP or pcDNA3.1 in the cDNA expression ratio of 1:2:1 (total transfected cDNA for a 4 well labteks=0.44 µg). Increasing doses of EGF-Alexa647 (0-640 ng/ml) were administered at an interval of 1.5 mins by doubling the concentration between two subsequent doses. FLIM-images of EGFR-mCitrine (corresponding to its FRET towards pY1086/1148 bound PTB-mCherry) were recorded as described in section 3.2.8 and

fluorescence confocal images of PTB-mCherry and RPTPγ/TCPTP-mTFP were taken as per section (3.2.7), before the administration of the next dose. The fraction of the phosphorylated EGFR (α_p) at each dose for every cell was calculated as described in sections (1.4.2) and (3.2.8). The amount of EGF-bound EGFR for an individual dose (d) was calculated from the ratio of integrated fluorescence intensity of EGF-Alexa647 and EGFR-mCitrine at the plasma membrane as follows:

$$[EGF - EGFR]_{(d)} = \frac{EGF_{PM(d)}}{EGFR_{PM(d)}}$$

Following that, the fraction of EGF-bound EGFR at an individual dose (d) was calculated:

$$Fraction\ of\ [EGF - EGFR]_{(d)} = \frac{[EGF - EGFR]_{(d)} - [EGF - EGFR]_{(0)}}{[EGF - EGFR]_{(max)} - [EGF - EGFR]_{(0)}}$$

The term $[EGF - EGFR]_{(0)}$ corresponds to the point before the EGF treatment (as a correction for bleed-through, if there is any) and $[EGF - EGFR]_{(max)}$ corresponds to the saturation of EGF-binding.

3.2.10 Imaging of PTP-oxidation with DyTo-FRET/FLIM

Cells were transfected with RPTPγ/TCPTP-mCitrine, EGFR-mTFP and CBL-BFP in the cDNA ratio of 1:1:1. Cells were treated with EGF-Alexa647 or H_2O_2 and subjected to incubation with 0.5 mM DyTo. A similar experimental setup was followed as described in sections 3.2.7, 3.2.8 and 3.2.9 to record the FLIM images of RPTPγ/TCPTP-mCitrine and to compute the fraction of oxidized PTP-mCitrine (α_{oxi}).

3.2.11 Spatiotemporal maps of EGFR and RPTPγ translocation

Confocal images were obtained as described in section 3.2.7 at one-minute intervals and background corrected. The cells were masked using PM defined by RPTPγ-mCitrine channel and nuclei were identified with CBL-BFP channel. For each pixel in the cell space, the normalized radial distance was calculated from its distance from the PM and NM, as follows:

$$r = \frac{r_{PM}}{r_{PM} + r_{NM}}$$

The pixels were segmented in 10 bins based on their normalized distances. The mean fluorescence intensities were calculated in each segment for RPTPγ-mCitrine, EGFR-mCherry and EGF-Alexa647 to obtain their spatial distribution profiles at a given time point. For individual cells, this procedure was performed for all the time-points at which the images were captured. The spatial profiles obtained at consecutive time-points were concatenated to form a spatiotemporal map (STM) that depicts the dynamics of the protein under consideration upon a given EGF-Alexa647 treatment. STMs obtained from individual cells were combined to yield an average STM.

3.2.12 Fluorescence loss after photoactivation (FLAP)

FLAP experiments were carried out at 37°C on a Leica SP8 microscope using a 63×/1.4 NA oil objective. MCF7 cells were transfected with photoactivatable paGFP-RPTPγ and RPTPγ-mCherry. Whenever, the experiment required Rab11a expression promoted biogenesis of RE, additional co-

transfection with BFP-Rab11a was performed. Pre-photoactivation images were acquired for paGFP-RPTPγ and RPTPγ-mCherry using the 488 nm and the 561 nm excitation wavelengths respectively. paGFP was excited with the 405nm Argon laser at 80% power in 3 frames on a perinuclear region of interest (ROI) to induce photoactivation. This perinuclear patch corresponding to the RE was identified by the localization of RPTPγ-mCherry in steady state. In the post-activation step, fluorescence images for paGFP-RPTPγ and RPTPγ-mCherry were acquired with a time interval of 30s, using the 488 nm and 561 nm WLL laser at 10% power. At the end of the experiment an image of BFP-Rab11a was acquired with 5% 405-laser power.

Following background correction, fluorescence loss after photoactivation at the RE was quantified as the ratio of local paGFP-RPTPγ to RPTPγ-mCherry fluorescence, to account for the changes in the structure and intensity in the ROI. Fluorescence gain on the PM was quantified as the ratio of local (cell periphery) paGFP-RPTPγ to RPTPγ-mCherry fluorescence.

Results

4.1 Interaction between EGFR and RPTPγ

4.1.1 Preferential interaction of RPTPγ with monomeric EGFR

To establish the basis of mutual regulation between RPTPγ and EGFR, we set out to decipher (1) whether there is a direct structural interaction between RPTPγ-EGFR? and (2) does this interaction depend upon EGF-binding to EGFR? For the experimental purpose, we chose breast cancer derived MCF7 cells that express low endogenous levels of EGFR (10^3 receptors/cell)[162] to avoid EGFR overexpression induced spurious activation or mis-localization artefacts.

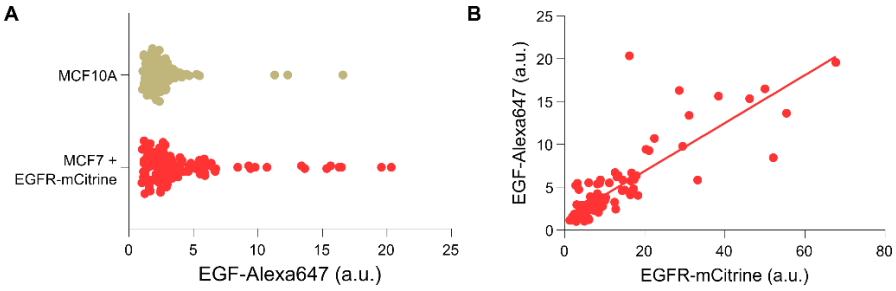

Figure 14: EGFR ectopic expression levels in MCF7 compared to endogenous expression in MCF10A

(A) Average EGF-Alexa647 binding to the endogenous EGFR in MCF10A cells (beige) in comparison to the binding level distribution for exogenous EGFR-mCitrine expressing MCF7 cells (red). **(B)** Distribution of EGF-Alexa647 binding levels as a function of EGFR-mCitrine expression levels in MCF7 cells. N=3, n>75 cells.

We exogenously expressed EGFR to match the expression levels in MCF10A (Figure 14) along with RPTPγ-mCitrine in 1:1 stoichiometric plasmid ratio. In these cell lysates, we carried out the immunoprecipitation of RPTPγ-mCitrine and probed for the extent of EGFR that gets pulled-along (Figure 15) as an effect of EGF or H_2O_2 treatment induced conformational changes or site-modifications. Strong interaction between EGFR and RPTPγ-mCitrine was observed in the absence of EGF treatment and it persisted when the cells were treated with the sub-saturating EGF-Alexa647 (5 and 20ng/ml). The interaction was substantially lost upon the administration of saturating EGF-Alexa647 (160 and 320ng/ml). The interaction between EGFR and RPTPγ-mCitrine prior to the EGF exposure hinted at the pre-existing regulation between them; that might have a probable role in the regulation of EGFR activation. The presence of interaction in the absence of EGF stimulus or at its low concentrations with the subsequent loss at higher EGF doses proved the preferential interaction of RPTPγ with the monomeric EGFR over EGF binding induced-EGFR dimers. The presence of EGFR pull-down in H_2O_2 treated as well as in the cells expressing catalytic cysteine mutant RPTPγ^{C1060S}-mCitrine proved that the interaction is independent of the cysteine oxidation or substrate trapping.

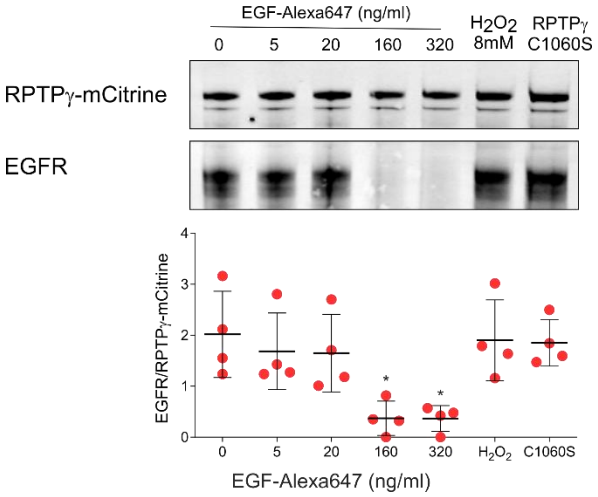

Figure 15: Direct interaction between EGFR and RPTPγ

Western blot and quantification showing co-immunoprecipitation of EGFR (lower blot) with RPTPγ-mCitrine (upper blot). The lysates were obtained from MCF7 cells expressing EGFR and RPTPγ-mCitrine, after 10 mins treatment with indicated concentration of EGF-Alexa647 (lane 1-5), 8mM H_2O_2 (lane 6) or cells expressing trapping mutant RPTPγ^{C1060S}-mCitrine. RPTPγ-mCitrine or RPTPγ^{C1060S}-mCitrine was pulled-down with anti-GFP antibody. Mean±SD, N=4, *P<0.05: unpaired two-tailed t-test.

4.1.2 EGF dependent spatiotemporal dynamics of EGFR and RPTPγ

Next, we explored the spatiotemporal nature of the interaction between EGFR and RPTPγ as an effect of growth factor stimulated vesicular dynamics. We exploited previous knowledge about EGFR endocytosis to drive the system in distinct activation and trafficking modes[46,50]. Combinations of pulsed/sustained and sub-saturating/saturating EGF-Alexa647 stimuli were created to have a control on the dimerization of EGFR as well as its recycling or degradation. After subjecting to the growth factor treatment, EGFR-mCherry and RPTPγ-mCitrine expressing MCF7 cells were imaged to track the localization of the respective species over the period of 2 hrs. The acquired information about their distributions over the cell space was plotted as a function of the radial distance and time as 3D spatiotemporal maps (STMs) to comprehend the relative changes in the concentrations of EGFR-mCherry and RPTPγ-mCitrine (Figure 16).

Prior to growth factor treatment, EGFR-mCherry and RPTPγ-mCitrine both retained PM localization with sparse presence on endosomes. After sustained (S-EGF) stimulus with 20 ng/ml EGF-Alexa647 (sub-saturating), both of the species underwent vesicular internalization, signified by the decrease in their PM fluorescence and increased fluorescence intensity on emerging endosomes in the cytosol (Figure 16A). Post initial internalization, RPTPγ-mCitrine was seen to shortly return back to the PM. The relative gain in the recycled amount of RPTPγ-mCitrine over the internalized fraction could be accounted to the retrograde trafficking of EGF induced internalized RPTPγ-mCitrine along with material pre-existing in the recycling endosomes (Figure 16A, right STM). EGFR-mCherry showed a gradual return to the PM (Figure 16A, left STM), accounting to the continuous recycling of EGFR-monomers induced by the sub-saturating low EGF treatment (Figure 16A, left STM top inset).

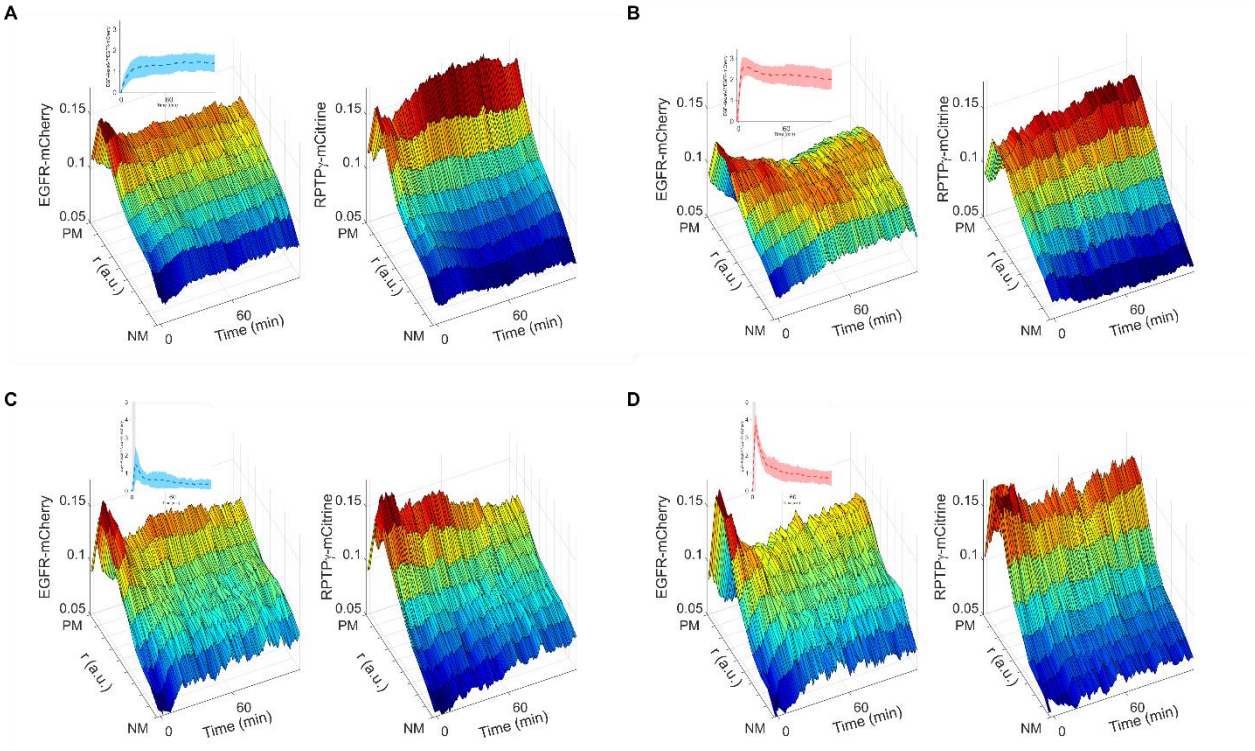

Figure 16: Spatiotemporal distribution of EGFR and RPTPγ interaction as a function of EGF treatment

Average spatial-temporal maps (STM) showing the changes in the distributions of EGFR-mCherry (left) and RPTPγ-mCitrine (right) upon EGF-Alexa647 sustained stimulus of 20ng/ml (**A**, S-EGF, N=2, n=13 cells) or 160ng/ml (**B**, S-EGF, N=2, n=14 cells); 5mins pulsed stimulus of 20ng/ml (**C**, 5P-EGF, N=4, n=18 cells) or 160ng/ml (**D**, 5P-EGF, N=3, n=18 cells) to MCF7 cells. The STMs were constructed from the single cell confocal images recorded at 1-min interval depicting the fluorescence intensities of EGFR-mCherry and RPTPγ-mCitrine as a function of radial distance from the nuclear membrane (NM) and the time after stimulus. The inset in EGFR-mCherry STMs shows the average PM distribution of the EGF-bound EGFR (EGF-Alexa647/EGFR-mCherry).

Conversely, when treated with 160 ng/ml S-EGF, a major fraction of EGFR-mCherry quickly achieved a ligand induced dimeric state (Figure 16B, left STM top inset) that forced it to divert its endocytic route and undergo unidirectional-trafficking instead. The continuously depleting fraction of EGFR-mCherry from the PM was observed to relocate to the perinuclear area (localization of late endosomes and lysosomes; Figure 16B, left STM). Whereas, RPTPγ-mCitrine steadily regained the PM localization after internalization (Figure 16B, right STM). At sub-saturating S-EGF condition, the early endocytic profiles of EGFR-mCherry and RPTPγ-mCitrine at the PM showed marked temporal resemblance (Figure 16A). On the other hand, the treatment with saturating S-EGF caused EGFR-mCherry to undergo continuous internalization without PM-return whereas RPTPγ-mCitrine showed recycling to the PM after internalization at early time points (Figure 16B). These observations substantiated our prior conclusion about the interaction of RPTPγ with monomeric EGFR (Figure 15).

To create a situation favorable to high EGFR-monomer formation, we stimulated cells with a 5 min pulse of 20 ng/ml (Figure 16C) or 160 ng/ml (Figure 16D) EGF-Alexa647 (5P-EGF). In both of these cases, similar to sub-saturating S-EGF situation, the profiles of EGFR-mCherry and RPTPγ-mCitrine at the PM mirrored in the temporal dynamics by exhibiting a decline at the initial time points after the EGF pulse followed by the repopulation at the PM. However, at 20 ng/ml 5P-EGF, the fluorescence intensities of

EGFR-mCherry and RPTPγ-mCitrine declined at the PM post 60 mins of EGF pulse (Figure 16C) as opposed to the other condition in comparison. Nevertheless, in all the mentioned cases, spatiotemporal dynamics of RPTPγ-mCitrine coupled strongly with the EGF-binding dependent vesicular trafficking of EGFR.

4.1.3 Vesicular recycling of RPTPγ via Rab11a-positive route

To elaborate the spatial route opted by RPTPγ on the lines of growth factor dependent vesicular transport, we monitored the endocytosis of RPTPγ and EGFR. MCF7 cells were transfected with RPTPγ-mCitrine, EGFR-mCherry, CBL-BFP and subject to EGF-DyLight405 treatment. Growth factor induced changes in the localization of RPTPγ-mCitrine, EGFR-mCherry were traced in early endosomes (EE), recycling endosomes (RE) and late endosomes (LE) with immunostaining against the marker proteins EEA1, Rab11a and Rab7 respectively.

At early time points post EGF-DyLight405 stimulus, EGFR-mCherry showed abundant entry to the EEs with a small fraction of RPTPγ-mCitrine exhibiting EEA1-positive EE localization (Figure 17A). The amount of EGFR-mCherry and RPTPγ-mCitrine present in the EEs decreased after 15 mins. Prior to growth factor stimulus, RPTPγ-mCitrine and EGFR-mCherry both showed co-localization with Rab11a-positive RE (Figure 17B, top row), highlighting the constitutive interaction between them. The interaction was lost upon treatment with 160ng/ml of EGF-DyLight405 (Figure 17B, bottom row) at which the influx of RPTPγ-mCitrine towards the RE increased whereas the fraction of EGFR-mCherry in the RE decreased (Figure 17B, profiles). After prolonged growth factor treatment, the majority of EGFR-mCherry along with EGF-DyLight405 (dimerized EGFR-mCherry) localized on Rab7-positive LE (Figure 17C) and RPTPγ was observed to regain PM localization with no entry to LE (Figure 17C). The loss of EGFR-mCherry from Rab11-positive RE upon EGF-DyLight405 treatment was compensated by its gain on Rab7-positive LE (Figure 17B; Figure 17C, profiles). On the other hand, a fraction of RPTPγ-mCitrine showed increased RE localization that declined at later time points and reflected in terms of concomitant gain at the PM. This showed distinct trafficking routes for RPTPγ-mCitrine and EGFR-mCherry after the treatment with saturating dose of EGF (160ng/ml). EGF-bound dimerized EGFR-mCherry followed the EE to LE route leading to unidirectional traficking[50]; whereas RPTPγ-mCitrine after a short entry to EEs recycled back to the PM via Rab11a-positive REs.

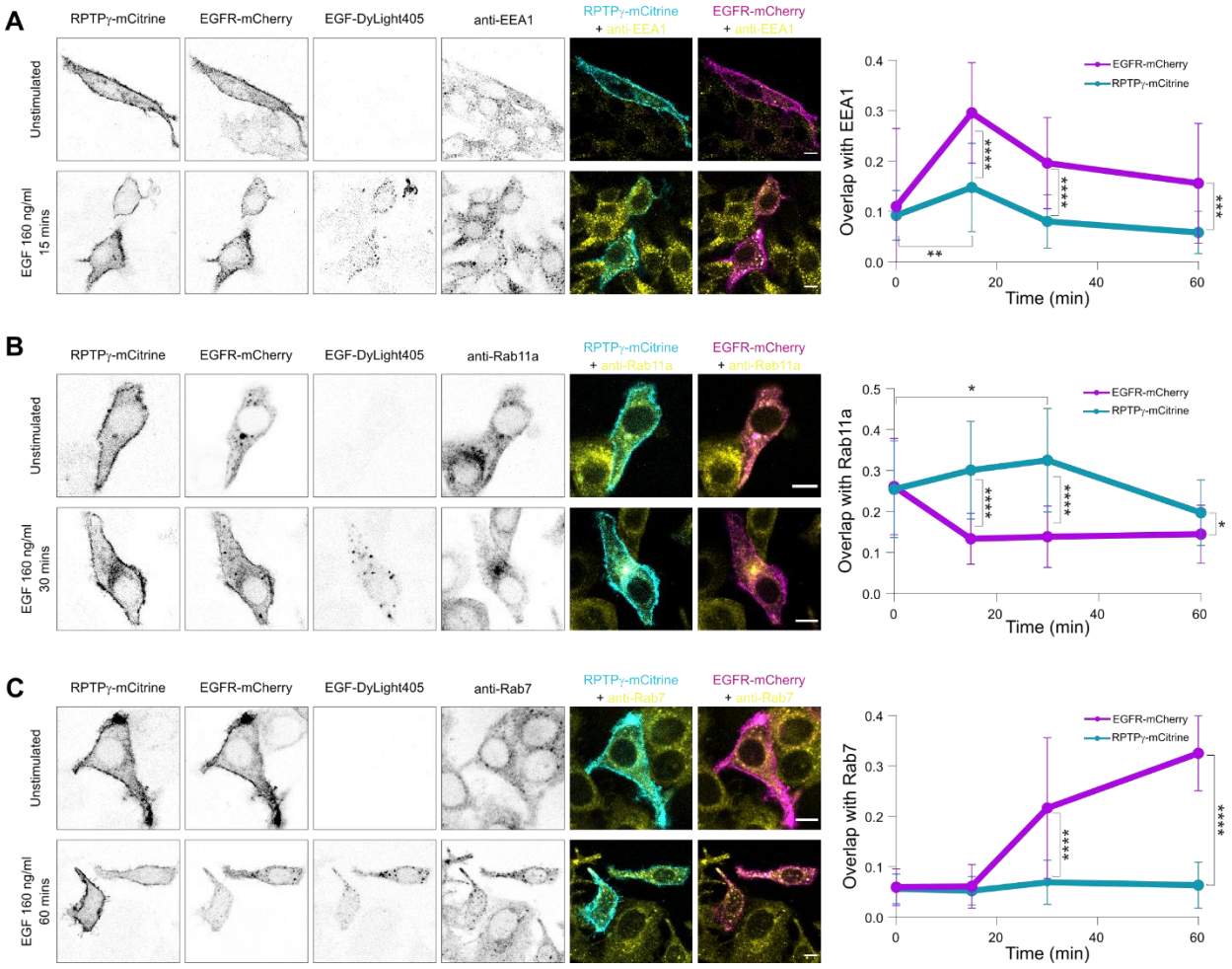

Figure 17: Endocytic recycling route of RPTPγ

(A) On the left: fixed-cell confocal images showing the spatial distribution of RPTPγ-mCitrine, EGFR-mCherry, EGF-DyLight405 along with EEA1-immunostaining for early-endosome (EE) marking, in the absence of (top row) and post EGF-DyLight405 stimulus (bottom row). Columns 5 and 6 show the overlay of EEA1-marker immunostaining with RPTPγ-mCitrine (cyan-yellow) or EGFR-mCherry (magenta-yellow) respectively. Scale bar-10μm ; On the right: Temporal profiles constructed from the above-described data indicating areal overlap between EGFR-mCherry (magenta profile) or RPTPγ-mCitrine (cyan profile) with EEA1-positive EE. **(B)** Analogous to (A), with immunostaining against recycling-endosome (RE) marker Rab11a**. (C)** Analogous to (A), with immunostaining against late-endosome (LE) marker Rab7. For each condition in **(A-C)**: N>3, n=25-30, *P<0.05, **P<0.01, ***P<0.001, ****P<0.0001: unpaired two-tailed t-test.

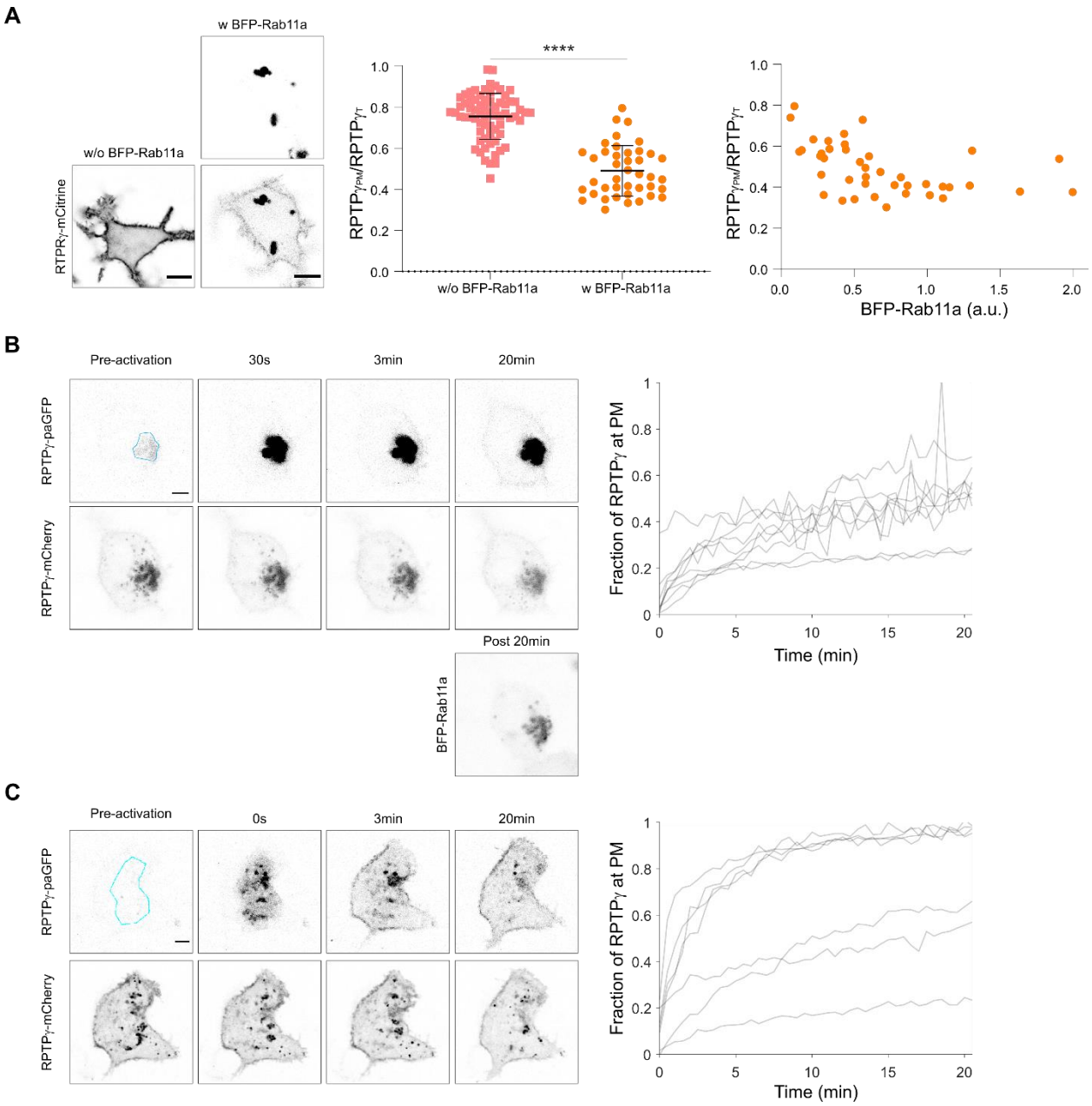

Figure 18: Recycling of RPTPγ through Rab11-positive endosomes

(A) on the left: live-cell images showing the steady state localization of RPTPγ-mCitrine in MCF7 (column 1) and the localization shift upon ectopic co-expression of RE biogenesis enhancer BFP-Rab11a (column 2). Scale bar-10μm. Corresponding quantification (middle, N=3, n>40, ****P<0.0001: unpaired two-tailed t-test). On the right: Graph showing fraction of PM localized RPTPγ-mCitrine as a function of BFP-Rab11a expression level variability across sampled cells. **(B)** On the left: Fluorescence loss after photoactivation (FLAP) of paGFP-RPTPγ (top row) on the recycling endosome (blue perinuclear area in pre-activation image) in live-MCF7 cells co-expressing RPTPγ-mCherry (middle row) and BFP-Rab11a (last row). Scale bar-5μm. On the right: corresponding quantification showing the return of RE relocated RPTPγ to the PM. On right: single cell profiles showing the rerouted fraction of RPTPγ on the PM from the RE. N=3, n=9 cells. **(C)** Images and quantification from the analogous FLAP experiment like (B) without BFP-Rab11a ectopic expression. N=3, n=7 cells.

The observation on the trafficking of RPTPγ-mCitrine to Rab11a-positive RE was further strengthened by the drastic shift of its steady state localization from the PM to the perinuclear RE, upon ectopic

expression of BFP-Rab11a (Figure 18A: left and middle panel). The increased biogenesis of RE in this case resulted into proportionate inflow of RE migrated RPTPγ-mCitrine as a function of BFP-Rab11a expression level (Figure 18A: right panel). Furthermore, we explored whether the RPTPγ situated on the RE can recycle back to the PM. We performed fluorescence loss after photoactivation (FLAP) with photoactivatable GFP fused RPTPγ (paGFP-RPTPγ) transfected in MCF7 cells along with RPTPγ-mCherry and BFP-Rab11a (Figure 18B). The presence of RPTPγ in newly formed Rab11a-induced REs was marked by RPTPγ-mCherry in the perinuclear region. In these regions, excitation of paGFP-RPTPγ caused decrease in paGFP-RPTPγ fluorescence whereas gain of paGFP-RPTPγ on the PM was observed over the duration of 20mins. This showed the recovery of RE situated RPTPγ to the PM, in the absence of growth factor stimulated vesicular trafficking. In order to avoid ectopic Rab11a induced perturbation, we performed the FLAP experiment without the BFP-Rab11a expression to cells and recapitulated the return of RPTPγ from the RE to the PM (Figure 18C). However, the relative recovery of RPTPγ was higher in this case as compared to the exogenous Rab11a situation due to the increased trapping of RPTPγ caused by ectopic-Rab11a induced increase of RE formation.

4.2 The effect of RPTPγ on EGFR phosphorylation

4.2.1 Absence of RPTPγ results in uncontrolled EGFR signaling

Furthermore, we explored whether the interaction between RPTPγ and EGFR has an effect on growth factor response and signaling properties of EGFR system. To study the effect of the RPTPγ expression on EGFR activity, CRISPR-Cas9 mediated knock-out (KO) of RPTPγ (*PTPRG*) was carried out in MCF7 cells (MCF7-RPTPγ-KO) and the phosphorylation of EGFR-activity allied signaling molecules was probed by immunoblotting so as to compare the changes in the relative activity levels with MCF7 cells (Figure 19). In these cell lysates EGFR signaling associated tyrosine site-1068 (Y1068) was observed to be phosphorylated without the treatment of cells with EGF. This showed the growth factor independent activation of EGFR as a consequence of the lack of RPTPγ derived regulation (Figure 19A). MCF7 cells, on the other hand, showed phosphorylation of Y1068 only upon EGF stimulus. Pre-activation of EGFR in MCF7-RPTPγ-KO cells was also reflected by the growth factor independent activation of signaling regulators- Akt (Figure 19B) and ERK 1/2 (Figure 19C), which are associated to cell migration and proliferation. Conversely, MCF7 cells showed AKT and ERK 1/2 phosphorylation only after EGF induced activation.

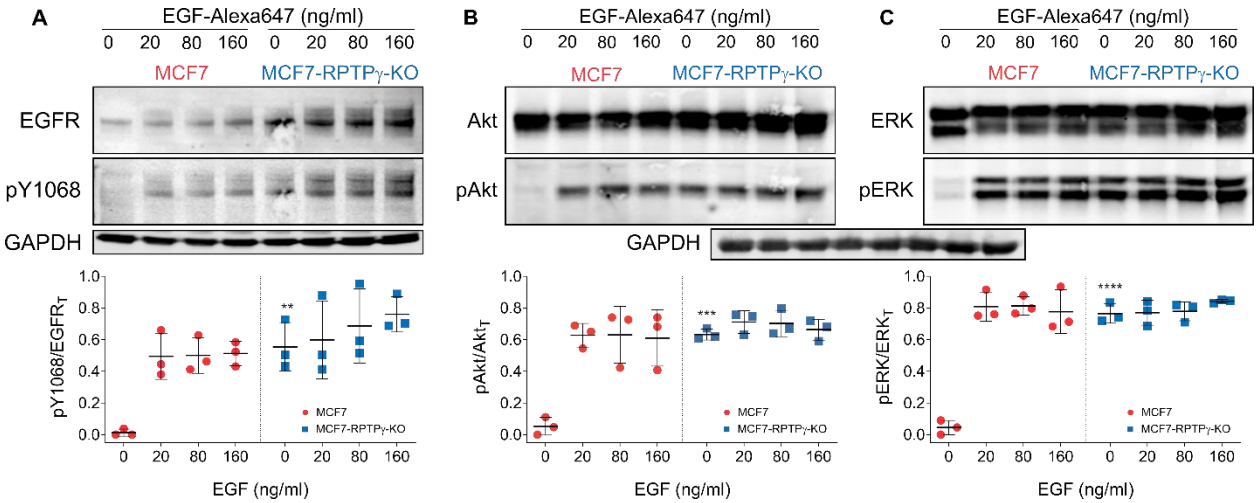

Figure 19: Active EGFR signaling in the absence of RPTPγ

(A) Representative western blots (top) and corresponding quantifications (bottom) comparing the EGFR phosphorylation levels at tyrosine 1068 (pY1068) in MCF7 (red) to MCF7-RPTPγ-KO (blue) cells upon indicated treatment of EGF-Alexa647 (0-160 ng/ml) for 5 mins. **(B and C)** Analogous to (A) for phosphorylation levels of Akt (pAkt) and ERK1/2 (pERK). GAPDH bands for each blot lane serve as corresponding loading controls. For each condition, the fraction of phosphorylated protein over total expressed protein is indicated as mean±SD, N=3, *P<0.05, **P<0.01, ***P<0.001, ****P<0.0001: unpaired two-tailed t-test against MCF7 no-EGF condition.

Pre-activation of EGFR was also observed in colorectal cancer derived HT29 cells that lack the RPTPγ expression as a result of promoter methylation[154]. Lysates derived from these cells showed phosphorylated Y1068 on endogenous EGFR in the absence of EGF treatment (Figure 20A). To examine whether the EGFR activation has been indeed affected by the lack of RPTPγ, we expressed RPTPγ-mTFP in HT29 cells and performed immunostaining against phosphorylated Y1068 (pY1068). In comparison to HT29 WT cells, the cells expressing RPTPγ-mTFP showed significantly decreased fraction of pY1068-positive stained EGFR, proving the rescue of activated EGFR-system in these cells by RPTPγ-mTFP expression (Figure 20B).

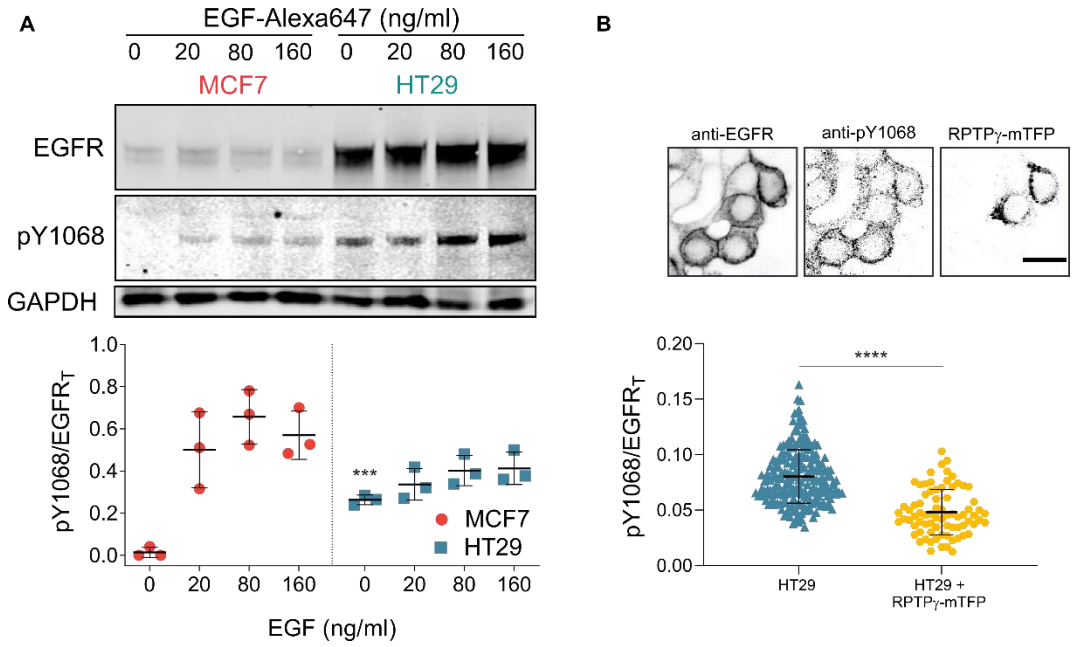

Figure 20: EGFR signaling in RPTPγ devoid CRC-HT29 cells

(A) Representative western blots (top) and corresponding quantifications (bottom) comparing the EGFR phosphorylation levels at tyrosine 1068 (pY1068) in MCF7 (red) to HT29 (blue) cells upon indicated treatment of EGF-Alexa647 (0-160 ng/ml) for 5 mins. GAPDH bands for each blot lane serve as corresponding loading controls. The fraction of phosphorylated protein over total expressed protein is indicated as mean±SD, N=3, ***P<0.001: unpaired two-tailed t-test against MCF7 no-EGF condition. **(B)** Top panel: fixed-cell confocal images for the immunostained endogenous EGFR (left), EGFR phosphorylation at tyrosine 1068 (middle: pY1068) and RPTPγ-mTFP fluorescence (right) in HT29 cells in the absence of EGF stimulus. Scale bar: 10μm. Bottom panel: corresponding quantification showing the decrease in pY1068 upon RPTPγ-mTFP expression. N=3, n>75 cells, ****P<0.0001: unpaired two-tailed t-test.

4.2.2 Activity of RPTPγ governs the growth factor response of EGFR

Next, we investigated how RPTPγ affects the growth factor concentration dependent phosphorylation response of EGFR. Therefore, we performed single cell cumulative EGF-dose experiment in which we treated MCF7 cells with ascending concentrations of EGF-Alexa647 (0-640 ng/ml) at the interval 1.5 mins (Figure 21B). Cells were transiently transfected with EGFR-mCitrine up to the average endogenous EGFR level in MCF10A cell line (Figure 14) along with phosphotyrosine-binding domain (PTB-mCherry), that upon phosphorylation of EGFR-mCitrine binds to the phosphotyrosines 1086/1148[163,164] and probes resulting EGFR-mCitrine phosphorylation. To quantify the fraction of phosphorylated EGFR, we measured the FRET between EGFR-mCitrine and PTB-mCherry by recording the decrease in the fluorescence lifetime of EGFR-mCitrine upon PTB-mCherry binding (Figure 21A). The fraction of phosphorylated EGFR-mCitrine (α_p) was estimated with the global analysis[130] and the EGF dose dependent profiles for α_p at the PM were constructed for individual cells (Figure 21C: left). In order to overcome the cell-to-cell variability associated with EGF-concentrations readout, we calculated the ratio of EGF-Alexa647 to EGFR-mCitrine fluorescence at individual EGF doses and normalized it to the same at the saturating dose of EGF to obtain the fraction of EGF-bound EGFR corresponding to the administered EGF concentration (Figure 21C: middle). We utilized the above calculation to interpret the phosphorylation responses in terms of the relative contribution of the

monomeric or dimeric receptors by plotting the fraction of phosphorylated EGFR-mCitrine (α_p) as a function of the fraction of EGF-bound EGFR (Figure 21C: right).

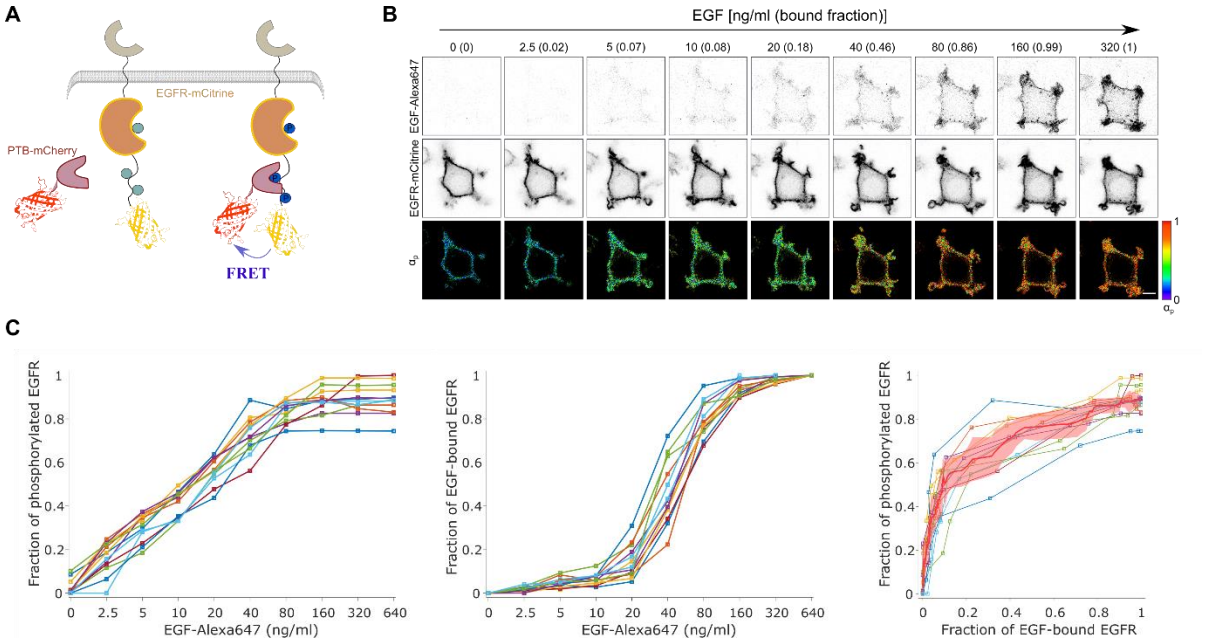

Figure 21: Quantitative single-cell imaging of EGFR phosphorylation by PTB-FLIM

(A) Schematic of PTB-FLIM approach for quantitative imaging of EGFR phosphorylation. In the absence of EGFR-mCitrine phosphorylation (left: cyan circles), PTB-mCherry doesn't get recruited and upon phosphorylation of EGFR-mCitrine (right: blue circles), binding with PTB-mCherry results in FRET between the involved species. **(B)** Representative confocal images of EGF-Alexa647 (top row), EGFR-mCitrine (middle row) and its phosphorylated fraction (bottom row) obtained by FRET-FLIM, from a single cell phosphorylation response series for MCF7 cells. Cells were stimulated with cumulative ascending doses of EGF-Alexa647 (0-640 ng/ml) at an interval of 1.5 mins. **(C)** Left: single cell phosphorylation profiles obtained from the EGF-dose response, middle: estimated fraction of EGF-binding to EGFR-mCitrine for each cell, right: single cell phosphorylation responses as a function of EGF-binding for each cell under consideration (thin lines) calculated with the profiles obtained from the left and the middle plots, along with the moving medians from single cell profiles (solid red line) and median absolute deviations (shaded bounds).

Prior to growth factor treatment, EGFR-mCitrine predominantly showing PM-localization maintained the unphosphorylated state in MCF7 cells and exhibited a graded response to increasing doses of EGF-Alexa647 stimulus (Figure 21B, C; Figure 22C: red). On the other hand, EGFR-mCitrine steady state localization in MCF7-RPTPγ-KO cells, was intracellular and characterized to be substantially ER associated (Figure 22A). These cells showed pre-activation of EGFR-mCitrine and retained the highly active state upon administration of EGF-Alexa647; showing the hampered growth factor responsiveness in the absence of RPTPγ even when the cells attained normal EGF-binding (Figure 22B; Figure 22C, blue). Similarly, HT29 cells exhibited phosphorylated EGFR-mCitrine prior to EGF stimulus and hardly any increase upon treatment with EGF-Alexa647 (Figure 22C, brown). Next, we attempted to rescue the system by exogenously expressing RPTPγ-mTFP in MCF7-RPTPγ-KO cells. As an effect of RPTPγ-mTFP expression, the localization of EGFR-mCitrine was restored to the PM and its phosphorylation showed close to nil basal level (Figure 22D) in these cells. Upon administration of increasing doses of EGF-Alexa647, EGFR-mCitrine phosphorylation did not elevate until the ligand

occupancy of 15-20% was accomplished (~20ng/ml of EGF-Alexa647) and showed a prompt switch-like activation when that threshold was reached (Figure 22C, yellow).

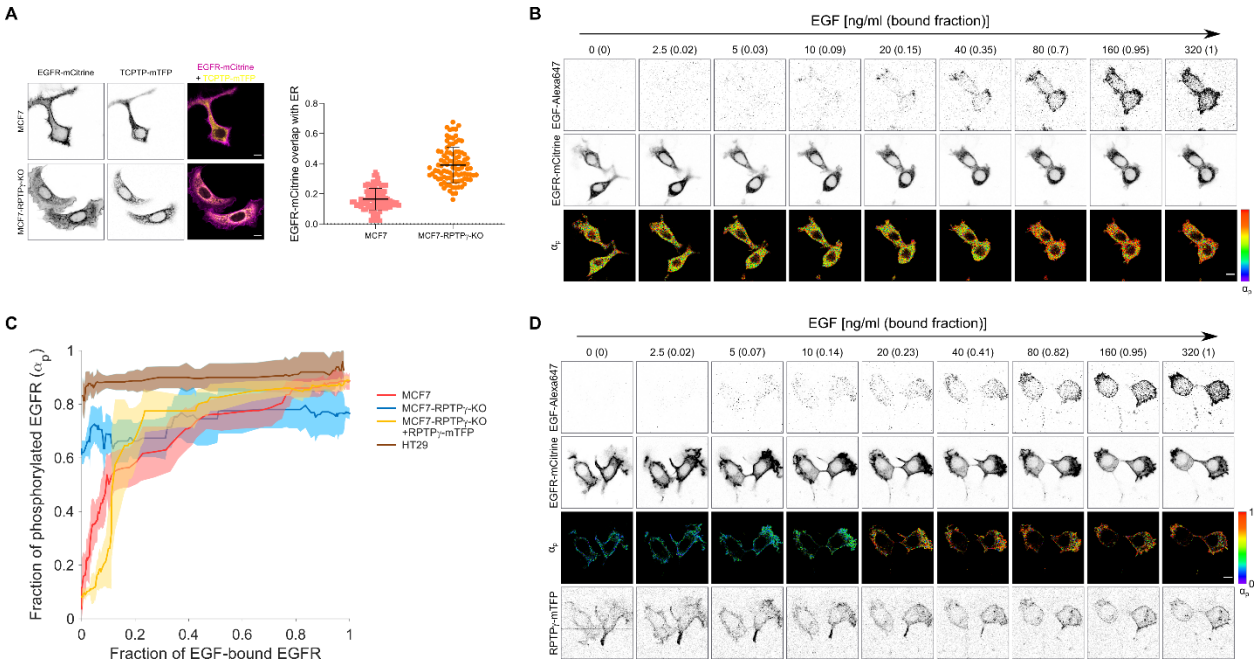

Figure 22: Effect of RPTPγ expression level on EGFR growth factor response

(A) Left: confocal images comparing the steady state localization of EGFR-mCitrine (left column) in non-EGF treated MCF7 cells (top row) to MCF7-RPTPγ-KO cells (bottom row). EGFR-mCitrine localized on the endoplasmic reticulum (ER) is identified by co-expression of TCPTP-mTFP as an ER-marker. Right: quantification of the areal overlap of EGFR-mCitrine fraction with ER-marker in comparison to the total expression level. N=3, n>50 cells. Scale bar-10μm. **(B)** Representative confocal images of EGF-Alexa647 binding (first row), EGFR-mCitrine (second row) with its phosphorylated fraction (α_p, third row) obtained from PTB-FLIM data for MCF7-RPTPγ-KO cells, when subject to treatment with ascending EGF-Alexa647 doses (0–320 ng/ml) at 1.5min interval. Scale bar-10μm. **(C)** EGFR-mCitrine phosphorylation single-cell response profiles to cumulative EGF-Alexa647 doses in MCF7 cells (red profile, N=3, n=13 cells), MCF7-RPTPγ-KO cells (blue profile, N=3, n=14 cells), MCF7-RPTPγ-KO with RPTPγ-mTFP co-expression (yellow profile, N=4, n=13 cells) and HT29 (brown profile, N=3, n=12 cells). Solid lines: moving medians from single cell profiles; shaded bounds: median absolute deviations. **(D)** Analogous images to (B) for MCF7-RPTPγ-KO cells with RPTPγ-mTFP expression (fourth row).

4.3 EGFR activity dependent oxidation of RPTPγ

4.3.1 Catalytic cysteine of RPTPγ undergoes EGF dependent oxidation

Subsequently, we explored whether the oxidation of RPTPγ is a probable mechanism that regulates its phosphatase activity and thereby allows for the growth factor dependent EGFR signaling. As discussed earlier (1.3.1), EGF dependent activation of EGFR triggers the assembly of NOX-complexes resulting in ROS production. To explore whether this can serve as a means for the catalytic activity regulation of RPTPγ, we probed the EGF dependent catalytic cysteine oxidation of RPTPγ. The initial step was to check if RPTPγ-mCitrine at all undergoes oxidation under the established sources of ROS like H_2O_2 on cell-population level. The concentration of H_2O_2 was selected in a range such that it could not generate higher oxidation products like sulfinic or sulfonic acid and the oxidation of RPTPγ was detectable in cysteine sulfenic acid form. We subjected MCF7 cells transfected with RPTPγ-mCitrine and EGFR to a

10 mins treatment of 4mM H_2O_2 and incubation with 5 mM dimedone to detect the oxidized state of RPTPγ-mCitrine. Oxidation was visualized by an antibody against dimedone-tagged sulfenic acid on a western blot (Figure 8). Since dimedone binds to all the proteins that undergo oxidation to sulfenic acid, the antibody proved to be inadequate to offer the specificity against oxidized RPTPγ alone. Therefore, by using antibody against GFP we immunoprecipitated RPTPγ-mCitrine from the lysates and subjected it to immunochemical detection (Figure 23).

The approach enabled us to detect the catalytic cysteine oxidation of RPTPγ-mCitrine upon H_2O_2 treatment. Next, we treated the cells with a saturating concentration of EGF-Alexa647 (160 ng/ml) and observed RPTPγ-mCitrine oxidation significantly above the basal level, proving its EGF dependence. To check the involvement of NOX-complexes in this occurrence, cells were pre-incubated with 10 µm flavoprotein inhibitor diphenyleneiodonium chloride (DPI) for 30mins. RPTPγ-mCitrine oxidation dropped significantly in this case affirming the NOX-routed RPTPγ oxidation as a result of EGF induced EGFR activation. Specificity of dimedone was verified by the incubation of cells with mere DMSO vehicle (without dimedone) in which oxidation RPTPγ-mCitrine was not detected. Cells expressing cysteine to serine mutated construct RPTPγ^{C1060S} –mCitrine did not undergo oxidation upon treatments with H_2O_2 or EGF-Alexa647, establishing the catalytic cysteine of RPTPγ as a target of intracellular ROS mediated activity regulation (Figure 23A).

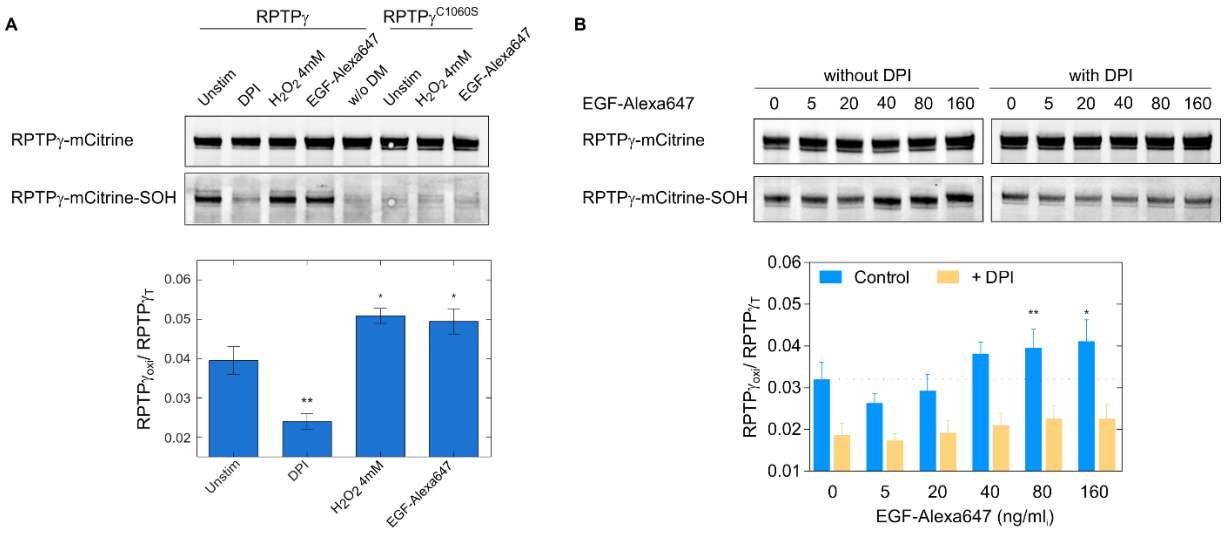

Figure 23: EGF-dependent oxidation of RPTPγ

Representative western blots and quantification for the oxidized fraction of RPTPγ-mCitrine. Cell lysates were obtained from MCF7 cells and stimulated with indicated stimulants for 10 mins; for DPI condition cells were pre-incubated for 30mins. **(A)** RPTPγ-mCitrine (lane 1-5) or RPTPγ^{C1060S}-mCitrine (lane 6-8) was pulled-down with an anti-GFP antibody (upper blot) and the oxidation of RPTPγ-mCitrine (lower blot) was detected with an anti-sulfenic acid antibody against dimedone conjugate. N=4, means±SEM. **(B)** Lysates without DPI treatment (left blot section; blue bar plots) and with DPI pre-treatment (right blot section; yellow bar plots) representing pulled-down RPTPγ-mCitrine (upper blot) and the oxidized fraction of RPTPγ-mCitrine (lower blot) detected as described in (A). N=5, means±SEM. *P<0.05, **P<0.01: calculated against unstimulated condition.

To decipher the coupling between EGFR activation and RPTPγ oxidation, we performed an EGF-dose response experiment to probe oxidation of RPTPγ with dimedone (Figure 23B). Cell populations were treated with concentrations of EGF-Alexa647 ranging from 0-160 ng/ml followed by incubation with dimedone. A minor level of RPTPγ-mCitrine cysteine oxidation was observed in serum starved cells which remained plateaued for lower doses. The oxidation peaked at the dose of 20 ng/ml and retained the high magnitude for subsequent EGF-doses. This switch-like trend of RPTPγ-mCitrine oxidation was absent when the cells were treated with DPI; additionally, the oxidation in this case was significantly lower as compared to the non-treated cells at all the EGF concentrations.

4.3.2 Imaging of oxidized RPTPγ in live cells by DyTo

The biochemical assay described above could aptly show the possibility of RPTPγ catalytic cysteine oxidation. However, it lacked the ability to spatially track the oxidized protein and posed limitations in terms of detecting localized protein oxidation on a single cell level. To overcome these issues, we developed a live-cell imaging approach that can spatially resolve the fraction of oxidized protein of interest. The imaging probe suitable for such a purpose was designed based on the following aspects: it should be - (1) able to trap the oxidized cysteine sulfenic acid from the protein of interest, (2) cell membrane permeable albeit maintain cell viability and (3) fluorescence labelled to aid specificity for imaging.

Therefore, we formulated a probe containing nucleophilic cysteine sulfenic acid binding moiety DYn-2 coupled to cell-permeable Atto590-azide by Cu-based click reaction (Azide-alkyne Huisgen cycloaddition)[159]. DyTo can irreversibly bind to the cysteine sulfenic acid residues of oxidized proteins and avail their imaging at the desired spatiotemporal position by receiving FRET from the mCitrine-tagged oxidized protein (Figure 24A). To validate the performance of DyTo in the detection of protein oxidation, we treated RPTPγ-mCitrine and EGFR expressing MCF7 WT cells with the producers of ROS like H_2O_2 or EGF-Alexa647 and probed the resultant cysteine oxidation with DyTo. On a western blot, DyTo showed a strong signal signifying its binding with oxidized of RPTPγ-mCitrine when the cells were subject to 8mM H_2O_2 or 160ng/ml EGF-Alexa647 and did not show binding when the cells were treated with either bare Atto590-azide (uncoupled to Dyn2 nucleophile) or they expressed cysteine site mutated form RPTPγ^{C1060S} –mCitrine (Figure 24B).

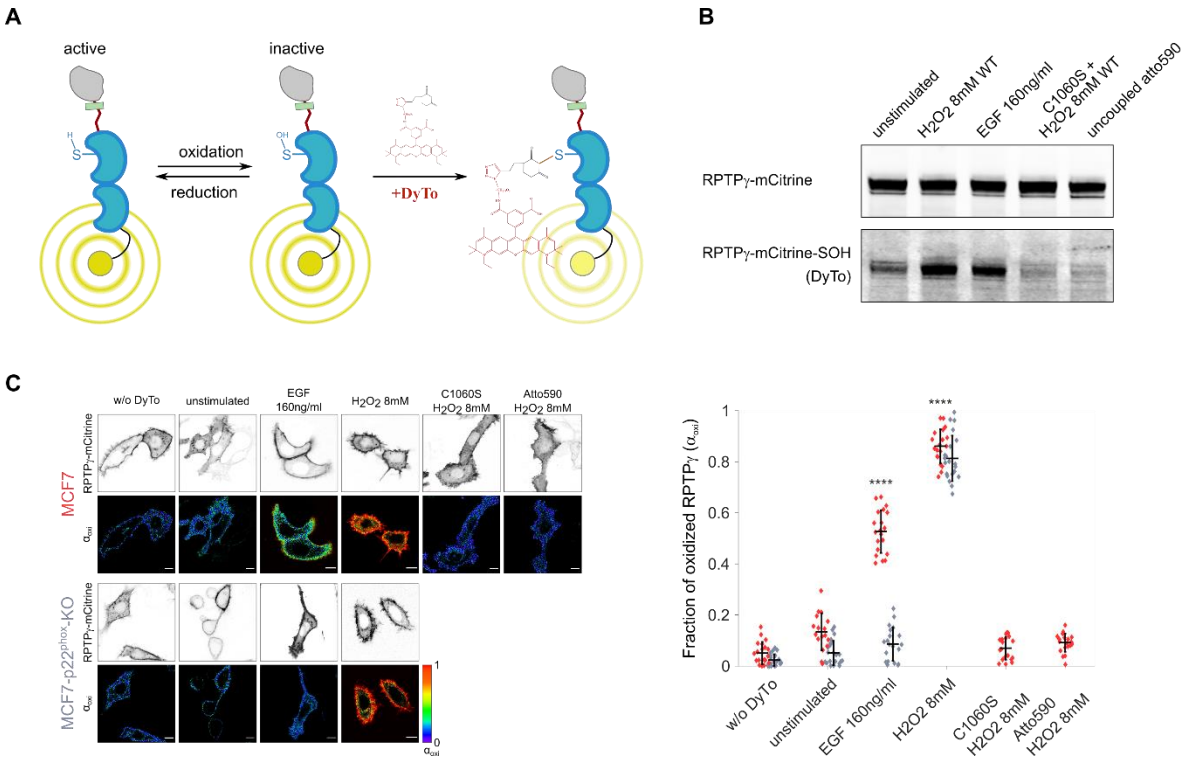

Figure 24: Performance validation of DyTo in imaging oxidized RPTPγ

(A) To detect thiol (-SH) oxidation of the protein of interest (blue unit) in its sulfenic acid (-SOH) form, dimedone derived DyTo probe was formulated and utilized in FLIM-FRET approach for the quantitative live-cell imaging of -mCitrine tagged oxidized protein upon its binding with atto590 label bearing DyTo. **(B)** Western blot characterizing the detection of oxidized RPTPγ-mCitrine (-SOH) by DyTo (bottom row) from total immunoprecipitated RPTPγ-mCitrine (top row). MCF7 cells were treated with indicated stimulant for 10 mins, with incubation with 0.5mM DyTo for last 5 mins. RPTPγ-mCitrine (lane 1-3, 5) or RPTPγ^{C1060S}-mCitrine (lane 4) were pulled-down with anti-GFP antibody. Lysates in lane 5 were treated with nucleophile uncoupled atto590-azide. **(C)** Representative images and quantification for the fraction of oxidized catalytic cysteine (α_{oxi}, bottom rows) of RPTPγ-mCitrine or RPTPγ^{C1060S}-mCitrine (top rows) for MCF7 cells (red) and MCF7-p22^{phox}-KO cells (gray). Oxidation was probed in live cells with DyTo or uncoupled Atto590-azide, upon treatment with EGF (160ng/ml) or H_2O_2 (8mM). Scale bar-10μm. mean±SD, N=3, n=15-18 cells per condition, ****P<0.0001: unpaired two-tailed t-test.

Thereafter, we explored the applicability of DyTo as an acceptor in a mCitrine-donor-based FRET assay, to image the oxidized RPTPγ in living cells (Figure 24C). We treated MCF7 cells expressing EGFR-mTFP and RPTPγ-mCitrine with ROS sources H_2O_2 or EGF-Alexa647 for 10 mins followed by an incubation with 0.5 mM DyTo for the last 5 mins. By applying FLIM to estimate the FRET between RPTPγ-mCitrine and DyTo, we quantified the relative fraction of DyTo bound oxidized RPTPγ-mCitrine (α_{oxi}) by global analysis[130]. When subject to 160 ng/ml of EGF-Alexa647, the PM-bound fraction of RPTPγ-mCitrine showed higher oxidation as compared to the reduced state in non-EGF treated cells (Figure 24C: MCF7, third column). Irrespective of its localization, oxidation of RPTPγ-mCitrine was observed to be strongest upon treatment with 8 mM H_2O_2 (Figure 24C: MCF7, fourth column). No FRET was detected in the cells expressing catalytically impaired mutant RPTPγ^{C1060S}–mCitrine post 8 mM H_2O_2 treatment, proving catalytic cysteine (C1060) indeed being the target of reversible oxidation (Figure 24C: MCF7, fifth column). Incubation of cells with uncoupled atto590-azide (lacking DYn-2

moiety to bind -SOH) in place of DyTo failed to detect oxidation to prove the specificity of FRET being measured by this approach (Figure 24C: MCF7, sixth column).

Since the EGF induced ROS production depends on the EGFR phosphorylation mediated activation of NOX-complex-associated proteins, we examined the effect of the absence of active NOX-complex on the oxidation of RPTPγ-mCitrine. We carried out the CRISPR-Cas9 induced knock-out of $p22^{phox}$ (*CYBA*), an essential subunit for ROS generating NOX 1-3 complexes in MCF7 cells and proceeded to image the oxidation of RPTPγ with DyTo. In the absence of $p22^{phox}$, RPTPγ-mCitrine oxidation did not exhibit EGF dependent increase (Figure 24C: MCF7-$p22^{phox}$-KO, third column) as observed in MCF7 cells, substantiating the necessity of the active NOX complex for RPTPγ oxidation at the PM. Upon treatment of the cells with 8 mM H_2O_2, oxidation of RPTPγ-mCitrine levelled to the oxidation in the case of MCF7 WT cells proving that the CRISPR-Cas9 induced deletion specifically perturbed the $p22^{phox}$ associated ROS-production (Figure 24C: MCF7-$p22^{phox}$-KO).

4.3.3 NOX-activity associates redox regulation of RPTPγ to EGFR activation

After establishing EGFR activity directed ROS production as an activity regulating mechanism for RPTPγ, we further explored how the EGF-binding induced EGFR phosphorylation couples to the oxidation response of RPTPγ. We addressed it by treating RPTPγ-mCitrine and EGFR-mTFP expressing MCF7 cells with a range of concentrations of EGF-Alexa647 (0-160ng/ml) for 10mins and monitoring the oxidized fraction of RPTPγ-mCitrine with DyTo (Figure 25A). Similar to the trend observed by immunochemical assay (Figure 23B), RPTPγ-mCitrine exhibited a basal reduced state for EGF-Alexa647 administration lower than 20 ng/ml and spiked upon treatments with 20-160 ng/ml (Figure 25A: 3-6, blue markers in profile). Oxidation of RPTPγ-mCitrine upon EGF-Alexa647 treatments, took place exclusively at the PM leaving the cytosolic fraction sparingly oxidized. Intriguing spatial variation was exhibited by oxidized RPTPγ-mCitrine in terms of the difference between the oxidized fractions on the PM and the endosomes (Figure 25A: blue markers versus orange markers). This proved that, EGF induced ROS production remains PM-localized and results in the oxidation of PM-bound RPTPγ-mCitrine specifically.

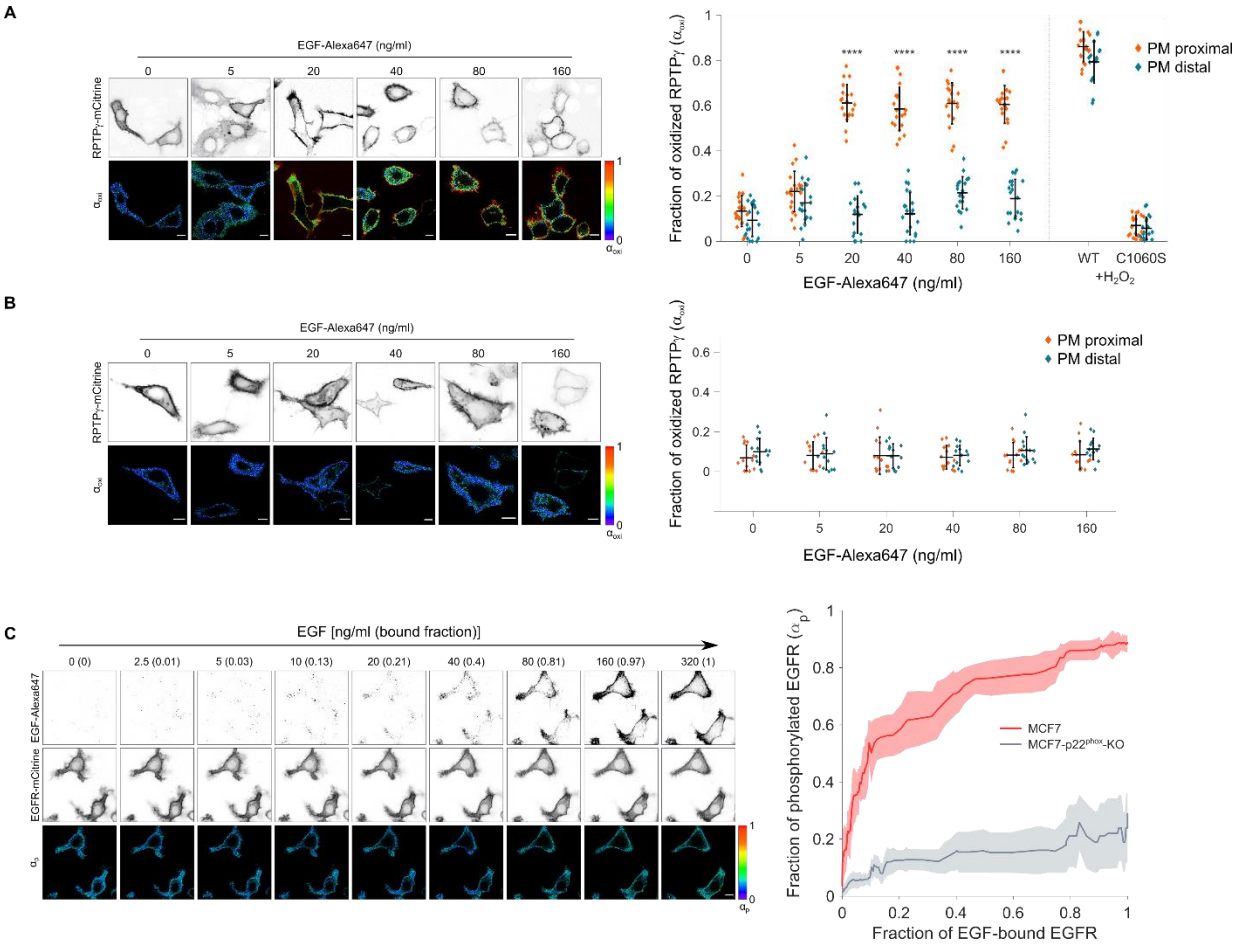

Figure 25: EGF-induced NOX-activity fundamental to oxidation of RPTPγ and activation of EGFR

(A) Left: confocal images of live-MCF7 cells showing RPTPγ-mCitrine (top row) and its oxidized fraction (α_{oxi}, bottom row), estimated using DyTo-based FRET-FLIM approach. Discreate sets of cells were treated with doses of EGF-Alexa647 (0-160 ng/ml) for 10 mins and incubated with 0.5 mM DyTo for the last 5 mins. Scale bar - 10μm. Right: single cell quantification depicting spatially resolved PM-proximal (orange) and PM-distal (blue) oxidized fraction from cells expressing RPTPγ-mCitrine or RPTPγ^{C1060S}-mCitrine upon treatments with EGF-Alexa647 or H_2O_2. mean±SD, N=3, n=13-15 cells per condition, ****P<0.0001: unpaired two-tailed t-test comparing PM-proximal and PM-distal fractions. **(B)** Analogous spatial mapping of RPTPγ-mCitrine oxidation to (A) for MCF7-p22^{phox}-KO cells and corresponding quantification. mean±SD, N=3, n=13-15 cells per condition. **(C)** Left: representative confocal images of EGF-Alexa647 binding (first row), EGFR-mCitrine (second row) with its phosphorylated fraction (α_p, third row) estimated from PTB-FLIM analysis for MCF7-p22^{phox}-KO cells (gray), when subject to treatment with ascending EGF-Alexa647 doses (0–320 ng/ml) at 1.5min interval. Scale bar-10μm. N=3, n=12 cells. Solid lines: moving medians from single cell profiles; shaded bounds: median absolute deviations.

To examine the effect of the lack of PM-based NOX-activity on EGF-induced RPTPγ regulation, we probed the EGF dose response of RPTPγ oxidation in MCF7-p22^{phox}-KO cells. Here, as opposed to the MCF7 cells, RPTPγ-mCitrine remained absolutely reduced and failed to register any oxidation response upon EGF-Alexa647 administration (Figure 25, B). The absence of p22^{phox}-associated NOX complexes resulted in the lack of ROS generation at the PM and therefore, the catalytic cysteine oxidation of RPTPγ was abolished. Next, we explored how the redox regulation RPTPγ activity affects the growth factor response of EGFR? We probed single cell EGF dose responses (as described in section 4.2.2) in MCF7-p22^{phox}-KO cells to trace the EGFR phosphorylation profiles as an effect of the lack of PM-bound

ROS generating assembly (Figure 25, C). Upon EGF treatment, EGFR-mCitrine phosphorylation did not elevate and maintained a reclined profile. Even after the EGFR-mCitrine reached EGF binding saturation (>100ng/ml of EGF-Alexa647), phosphorylation of EGFR-mCitrine hardly showed increase. This proved the inhibition of RPTPγ by oxidation is crucial for the ligand dependent activation of EGFR. Moreover, the activity of $p22^{phox}$-associated NOX-complex emerged as a regulatory switch between RPTPγ catalytic regulation and EGFR response.

4.3.4 RPTPγ oxidation is temporally regulated by ligand dependent EGFR activation and vesicular trafficking

After establishing the EGF induced spatial regulation of RPTPγ oxidation, we explored whether the redox cycle of RPTPγ is affected by the ligand dependent EGFR activation and vesicular trafficking. As demonstrated in section 4.1.2, we specifically subjected the system to desired activation dynamics and the choice of trafficking route by tailoring the magnitude and the duration of EGF stimulus. To map the temporal aspect of oxidation, we treated RPTPγ-mCitrine and EGFR-mTFP expressing MCF7 cells with EGF-Alexa647 and incubated with DyTo 5 mins before the timepoint of interest (Figure 26 and Figure 27). When subject to 5 min pulse (5P-EGF) or sustained stimulus (S-EGF) with 20ng/ml EGF-Alexa647, RPTPγ-mCitrine showed a sharp increase in the oxidation 10 min post stimulus (Figure 26A; B: top left). The oxidized state prolonged until 15 min, indicating continuous ROS production at the PM due to the autocatalytically activated EGFR-mTFP monomers at low EGF dose in both of these cases. As observed before, oxidation was PM-localized and the endosomal fraction was reduced (Figure 26A, B: bottom left). However, comparing these two cases, the oxidation profiles at the PM diverged after 15 min. Upon treatment with the 5P-EGF, RPTPγ-mCitrine recouped the basal reduced state (Figure 26A; B: top left); whereas, S-EGF resulted in maintaining a high level of oxidized fraction at the PM (Figure 26C; D: top left).

To explain this distinction, we quantified the fraction of EGFR-mTFP on the PM relative to the total EGFR-mTFP expression in the whole cell (Figure 26 B and D: bottom right) as well as the corresponding ratio of EGF-Alexa647 to EGFR-mTFP at the PM for each time point (Figure 26 B and D: top right). At a sub-saturating dose of EGF-Alexa647 such as 20 ng/ml, only a fraction of phosphorylated EGFR-mTFP achieved dimerization. The majority of EGFR-mTFP remained in the form of autocatalytically activated ligand-less monomers that continued to endocytose and recycle back to the PM, aptly reflected in terms of the fraction of EGFR present at the PM for both 5P-EGF (Figure 26 B: bottom right) and S-EGF (Figure 26 D: bottom right). However, in S-EGF situation, the continuous availability of EGF in the surrounding environment retained a persistent EGFR-mTFP activity by ensuring the ligand-binding to recycled EGFR-mTFP (Figure 26 D: top right). Maintenance of a steady fraction of active EGFR at the PM was achieved by constant recycling and EGF-binding that resulted in sustained ROS production by NOX-complex; which retained a steady high level of RPTPγ-mCitrine oxidation (Figure 26 D: top left). The fraction of RPTPγ-mCitrine in the cytosol stayed reduced with a minor increase in oxidation on the timescale of the increased endocytosis of EGFR-mTFP (Figure 26 B, D: bottom left).

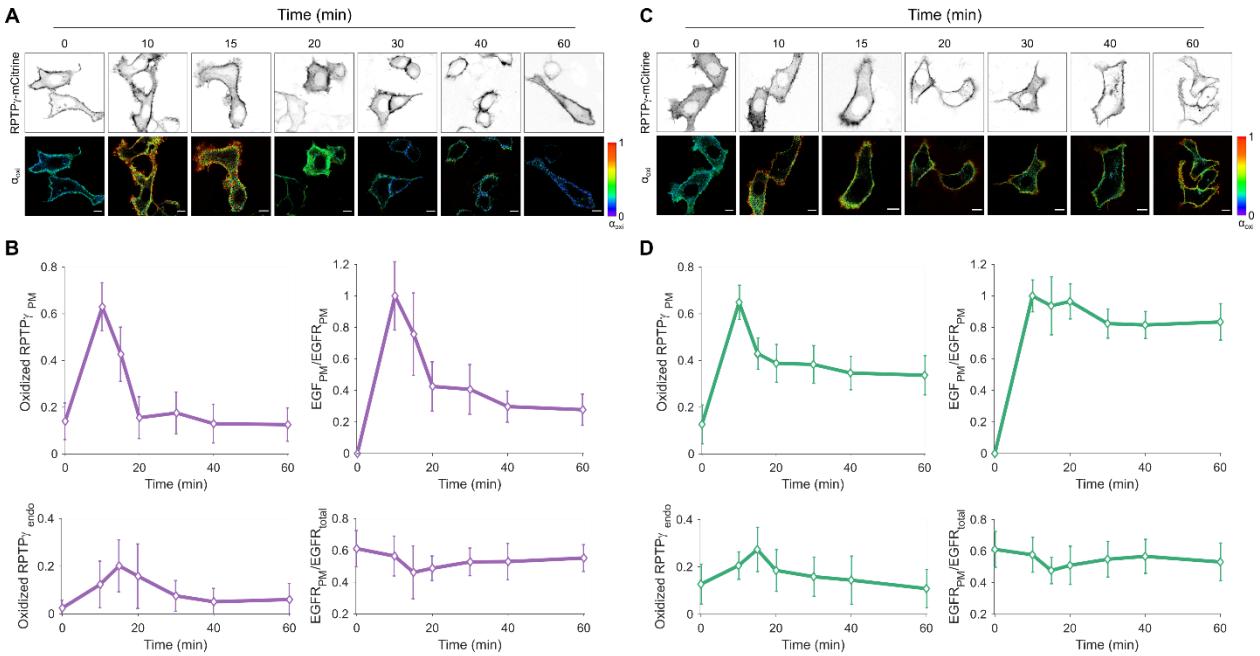

Figure 26: Temporal mapping of RPTPγ oxidation at sub-saturating EGF stimulus

(A) and (C): Representative confocal images depicting the temporal dynamics of RPTPγ-mCitrine oxidation in response to 5 mins pulse (5P-EGF, **A**) or sustained (S-EGF, **C**) treatment with 20 ng/ml EGF-Alexa647. Upper row: RPTPγ-mCitrine fluorescence images and lower row: the fraction of oxidized RPTPγ-mCitrine imaged with DyTo-FLIM. Scale bar-10μm. (**B) and (D):** Corresponding quantifications to (A and C). Top left: the fraction of oxidized RPTPγ-mCitrine at the PM, Bottom left: the fraction of oxidized RPTPγ-mCitrine on the endosomes. Top right: the ratio of EGF-Alexa647 to EGFR-mTFP fluorescence intensity at the PM, normalized at the 10min time point. Bottom right: fraction of EGFR-mTFP at the PM. N=3, n=18-23 cells per time point.

Despite the high dose of EGF, oxidation profile at saturating pulse of EGF-Alexa647 (5P-EGF 160ng/ml) exhibited a similar trend to the analogous sub-saturating condition, owing to the shorter duration of stimulus (Figure 27 A, B: top left). The oxidation profile of RPTPγ-mCitrine justified its dependence on EGF-pulse induced recycling of EGFR-mTFP; that nevertheless did not maintain its long-term activity due to the depletion of EGF-Alexa647 (Figure 27 B: top and bottom right). However, a sustained treatment with saturating EGF-Alexa647 (S-EGF 160ng/ml) resulted in attainment of basal reduced state by RPTPγ-mCitrine after a peak of oxidation, unlike its sub-saturation analogue (Figure 27 C, D: top left). This could be accounted to the unidirectional trafficking of EGFR-mTFP accomplished at the sustained saturating stimulus (Figure 27 D: bottom right). Sustained external supply of EGF-Alexa647 in the media resulted in the dimerization of the majority of EGFR-mTFP causing its PM-available fraction to continuously decline. This actuated into the loss of EGFR activity dependent ROS production at the PM.

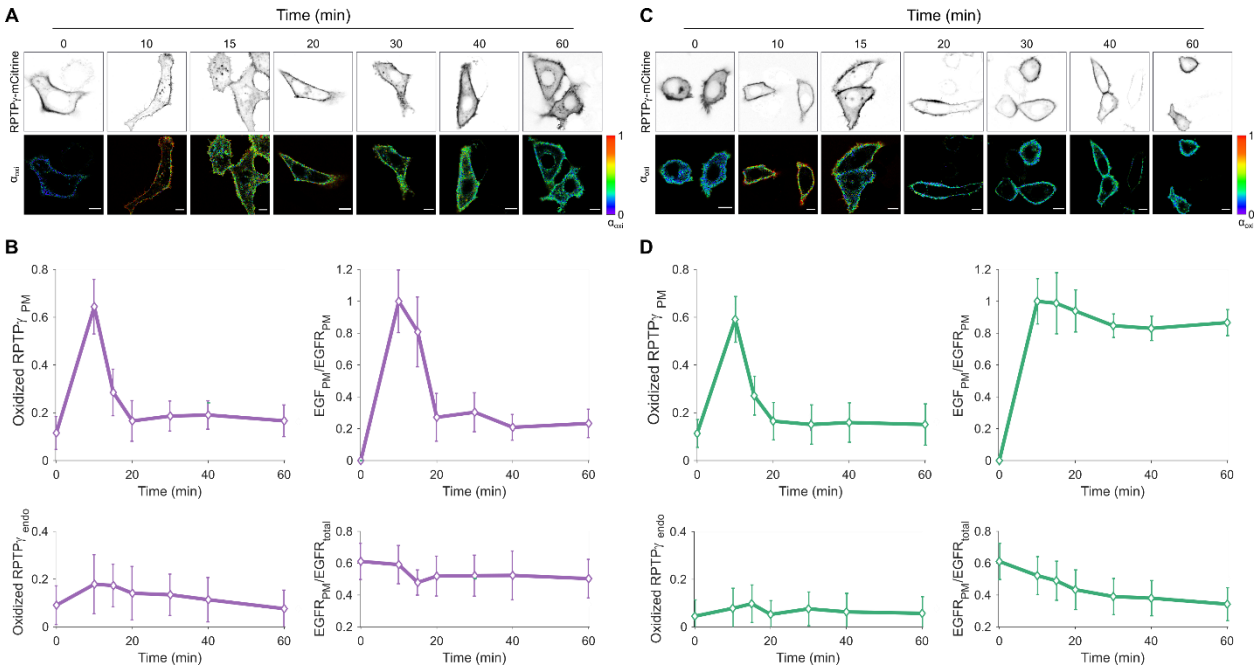

Figure 27: Temporal mapping of RPTPγ oxidation at saturating EGF stimulus

(A) and (C): Representative confocal images depicting the temporal dynamics of RPTPγ-mCitrine oxidation in response to 5 mins pulse (5P-EGF, **A**) or sustained (S-EGF, **C**) treatment with 160 ng/ml EGF-Alexa647. Upper row: RPTPγ-mCitrine fluorescence images and lower row: the fraction of oxidized RPTPγ-mCitrine imaged with DyTo-FLIM. Scale bar-10μm. **(B) and (D):** Corresponding quantifications to (A and C). Top left: the fraction of oxidized RPTPγ-mCitrine at the PM, Bottom left: the fraction of oxidized RPTPγ-mCitrine on the endosomes. Top right: the ratio of EGF-Alexa647 to EGFR-mTFP fluorescence intensity at the PM, normalized at the 10min time point. Bottom right: fraction of EGFR-mTFP at the PM. N=3, n=18-23 cells per time point.

4.4 TCPTP supplements the regulation of EGFR signaling response

4.4.1 EGFR growth factor response is modulated by TCPTP

In addition to the major phosphatase activity of RPTPγ, ER-associated TCPTP has been demonstrated to exhibit its catalytic activity on monomeric as well as dimeric EGFR. It regulates the duration of EGFR signaling by dephosphorylating the endocytosed EGFR upon their encounter in the perinuclear region[138]. Therefore, we set out to investigate the effect of TCPTP expression level on the EGFR growth factor sensitivity and overall response profile. We created CRISPR-Cas9 induced KO of TCPTP (*PTPN2*) in MCF7 cells (MCF7-TCPTP-KO) and performed previously described (section 4.2.2) single-cell EGF-Alexa647 dose response experiments to probe EGFR phosphorylation (Figure 28).

TCPTP-KO resulted in the higher basal level of EGFR-mCitrine phosphorylation before the administration of EGF-Alexa647 (Figure 28 A, B: green). However, in comparison to MCF7-TCPTP-KO, the pre-EGF stimulus fraction of phosphorylated EGFR-mCitrine observed in MCF7-RPTPγ-KO cells was superior (Figure 22C: blue). Even if MCF7-TCPTP-KO cells showed pre-activation, EGFR-mCitrine phosphorylation showed a response to increasing binding of EGF-Alexa647 as opposed to the hampered response in MCF7-RPTPγ-KO case. The exogenous expression of TCPTP-mTFP to MCF7-TCPTP-KO cells rescued the system by resetting the EGFR-mCitrine phosphorylation to the initial levels comparable to MCF7 cells. The rescued cells showed a steep EGFR-mCitrine phosphorylation profile

upon increasing EGF doses and the final magnitude attained by phosphorylation response was less than MCF7 WT (Figure 28 C, B: magenta).

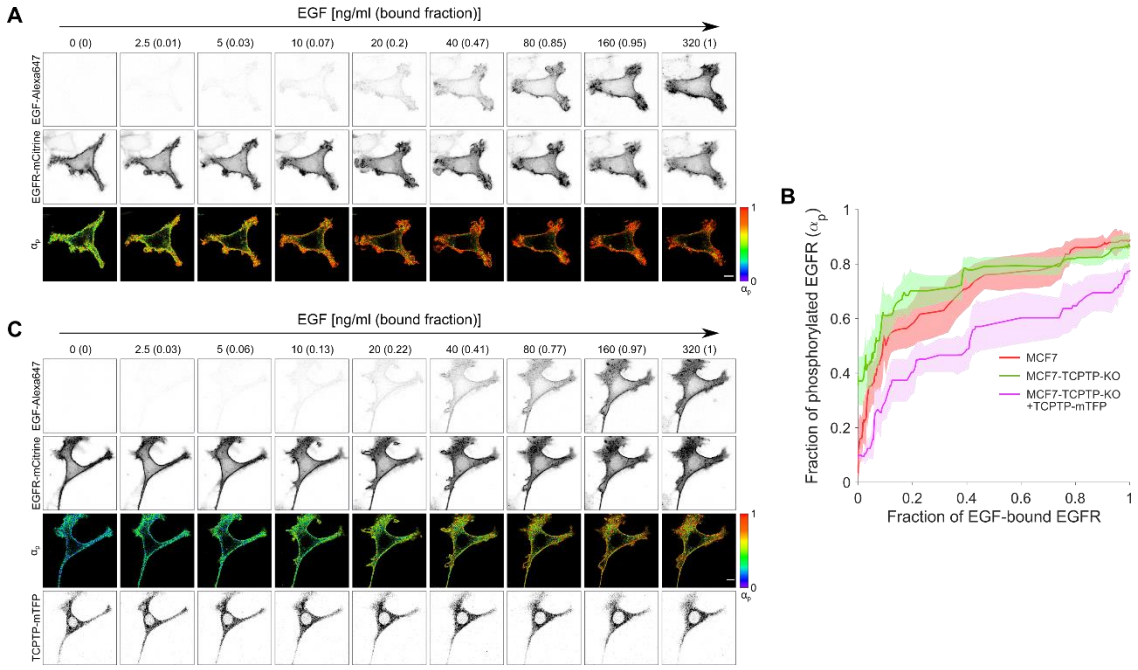

Figure 28: Effect of TCPTP expression level on EGFR growth factor response

(A) Representative confocal images of EGF-Alexa647 binding (first row), EGFR-mCitrine (second row) with its phosphorylated fraction (α_p, third row) obtained from PTB-FLIM analysis for MCF7-TCPTP-KO cells, when subject to treatment with ascending EGF-Alexa647 doses (0–320 ng/ml) at 1.5 min interval. Scale bar-10 μm. **(B)** EGFR-mCitrine phosphorylation single-cell response profiles to cumulative EGF-Alexa647 doses in MCF7 cells (red profile, N=3, n=13 cells), MCF7-TCPTP-KO cells (green profile, N=3, n=14 cells), MCF7-TCPTP-KO with TCPTP-mTFP co-expression (magenta profile, N=3, n=13 cells). Solid lines: moving medians from single cell profiles; shaded bounds: median absolute deviations. **(C)** Analogous images to (A) for MCF7-TCPTP-KO cells with TCPTP-mTFP expression (fourth row).

The above observations highlight the role of TCPTP in maintaining the inactive state of EGFR at the PM by making sure that the continuously recycling EGFR monomers undergo dephosphorylation before they reach the PM. Additionally, it also functions as a modulator of overall EGFR signaling response by exhibiting its catalytic activity (prominent in exogenous expression case) on ligand activated EGFR (Figure 28 B: magenta).

4.4.2 Oxidation of TCPTP exhibits spatial variance at saturating EGF

On the lines of EGFR activity dependent RPTPγ oxidation, we investigated whether this mechanism of EGF induced ROS could regulate the catalytic cysteine activity of TCPTP as well (Figure 29). To begin with, we applied the dimedone based approach to detect the oxidation of TCPTP-mCitrine on IP-western blot of cell lysates obtained from MCF7 cells expressing TCPTP-mCitrine and EGFR (similar to section 4.3.1). Although TCPTP showed a moderate constitutive oxidation of catalytic cysteine, it did not follow EGF treatment dependent increase (Figure 29A: blots and quantification in blue bars).

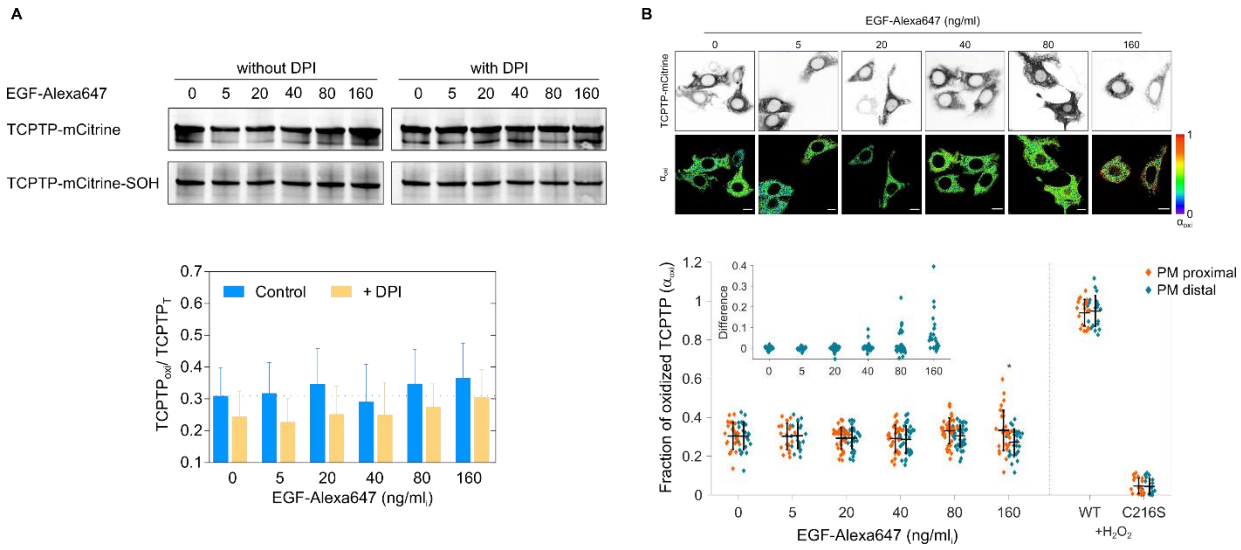

Figure 29: EGF dependence of TCPTP oxidation

(A) Representative western blots and quantification for the oxidized fraction of TCPTP-mCitrine. Cell lysates were obtained from MCF7 cells and stimulated with indicated stimulants for 10 mins; for DPI condition cells were pre-incubated for 30mins. TCPTP-mCitrine was pulled-down with anti-GFP antibody (upper blot) and the oxidation of TCPTP-mCitrine (lower blot) was detected with an anti-sulfenic acid antibody against dimedone conjugate. N=4, means±SEM. **(B)** Left: confocal images of live-MCF7 cells showing TCPTP-mCitrine (top row) and its oxidized fraction (α_{oxi}, bottom row), estimated using DyTo-based FRET-FLIM approach. Discreate sets of cells were treated with doses of EGF-Alexa647 (0-160 ng/ml) for 10 mins and incubated with 0.5 mM DyTo for the last 5 mins. Scale bar - 10μm. Right: single cell quantification depicting spatially resolved PM-proximal (orange) and PM-distal (blue) oxidized fraction from cells expressing TCPTP-mCitrine or TCPTP ^{C216S}-mCitrine upon treatments with EGF-Alexa647 or H_2O_2. The inset in the quantification is showing the difference between PM-proximal and PM-distal fractions of oxidized TCPTP-mCitrine mean±SD, N=3, n=18-21 cells per condition, *P<0.05: unpaired two-tailed t-test comparing PM-proximal and PM-distal fractions.

Considering the limitations of population level readout of western blot, we further probed into the oxidation of TCPTP on a single-cell level by DyTo-based FRET-FLIM approach (similar to section 4.3.2). The individual sets of MCF7 cells expressing TCPTP-mCitrine and EGFR-mTFP were treated with doses of EGF-Alexa647 (5-160 ng/ml) and the cysteine oxidation was probed with DyTo. Similar to the previous observations, TCPTP-mCitrine showed a basal high oxidized fraction of catalytic cysteine in untreated case and the constitutive uniform level of oxidation at the low concentrations of EGF-Alexa647 (Figure 29B). Conversely, at saturating doses (80 and 160 ng/ml), the extent of oxidation started to vary across the spatial span of ER. The oxidized fraction of TCPTP-mCitrine proximal to the PM was significantly higher than the perinuclear fraction after the administration of 160 ng/ml EGF-Alexa647 (Figure 29B: plot inset).

The EGF dependence of TCPTP oxidation was restricted to saturating doses at which most of the PM associated EGFR was in ligand bound dimeric form. Unlike RPTPγ oxidation that showed strong coupling with active-EGFR monomers, TCPTP demonstrated dependence on EGFR dimeric form to achieve redox regulation of PM-proximal subpopulation.

Discussion

5.1 RPTPγ is an essential regulator of EGFR growth factor response

Many of the EGFR studies in literature consider EGFR dimers as the prominent functional units that are responsible for downstream signaling. Such an outcome requires treatment with saturating EGF (>100 ng/ml) to get majority of EGFR in active dimerized state. Contrarily, in the physiological conditions the concentration of EGF in paracrine milieu is in the range of 0.1-20 ng/ml[165]. At this concentration, most of the EGFR are in unliganded monomeric state, a few as mono-ligand bound dimers and scarcely as double-ligand bound dimers[34]. It has been demonstrated that under physiological conditions autocatalytic activation of EGFR monomers is necessary for triggering the system activation[50]. This activation mechanism drives the system to attain fast activation even at the low concentrations of EGF but leaves it susceptible to the autonomous activation by minute conformational fluctuations. Considering the prior knowledge about the regulation of the autocatalytic site of EGFR by RPTPγ[138], we hypothesized the role of RPTPγ in suppressing the spurious activation of EGFR and investigated the effect of RPTPγ expression on the growth factor sensing of EGFR.

5.1.1 RPTPγ maintains EGFR in low activity state and prevents it from attaining unconstrained signaling

The phosphatase activity of RPTPγ was revealed to be the central regulator of EGFR activation. Knock-out of *PTPRG*/RPTPγ in MCF7 cells resulted in the ligand independent constitutive activation of EGFR (Figure 19). Since these cells express a very low amount of EGFR, overexpression-induced aberrant activation of EGFR cannot account for such an anomaly. MCF7 cells with an intact RPTPγ expression, responded only upon exogenous EGF administration whilst maintaining an inactive state in the absence of EGF perturbation. This proves the essential role of RPTPγ in enabling the system to sense the physiologically-relevant changes in the growth factor environment. The basis of this regulation can be explained by the positions of above-described cases in the 3D bifurcation diagram derived from causality between of EGFR and PTPs (Figure 30). The 3D bifurcation diagram theoretically predicts the phosphorylation dynamics of EGFR at the plasma membrane depending on the relative expression levels of RPTPγ-EGFR and the extent of EGF-binding. In the absence of RPTPγ the system is positioned on the extreme left in the pre-activation zone, characterized by the complete activation of EGFR irrespective of EGF stimulus. Lack of inhibitory phosphatase activity on autocatalysis leaves EGFR vulnerable to attaining ligand-independent active conformation induced by random fluctuations.

The pre-activated state of the system was evident from the constitutive activity of EGFR that propagated further to the ligand-independent phosphorylation of ERK1/2 and Akt. The involvement of these critical signaling kinases in cell migration and proliferation[6] made the RPTPγ mediated regulation significant in terms of refraining EGFR from manifesting tumorigenic properties. Cancer cells like HT29 bearing endogenous lack of RPTPγ exhibited similar pre-activation of EGFR signaling (Figure 20). However, we could rescue the system with exogenous expression of RPTPγ by lowering the extent of pre-activation significantly. These results are in line with the correlational evidence in literature for the lack of RPTPγ

associated with tumor samples[153,154]. Notably, the expression of RPTPγ is also shown to regulate the activation of EGFR-Y1068/Akt[156] in NPC and ERK1/2 in ALL[157,158]. RPTPγ expression induced rescue of the system demonstrates the direct function of RPTPγ in securing EGFR to a low phosphorylation state. Thereby, we prove that RPTPγ acts as a major regulator of EGFR ligand-sensing that can potentially function as a tumor suppressor in association to EGFR signaling.

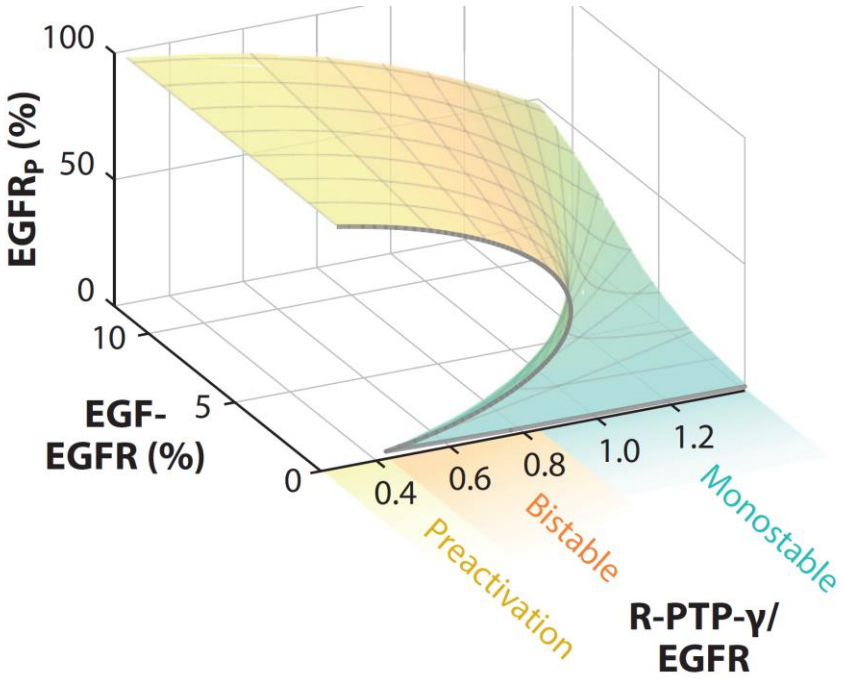

Figure 30: 3D bifurcation diagram of EGFR-RPTPγ network

Three-dimensional bifurcation diagram depicting the dependence of EGFR phosphorylation (% EGFRp) on the relative levels of RPTPγ and EGFR on the plasma membrane (R-PTP-γ/EGFR) and the fraction of ligand-bound EGFR (% EGF-EGFR). Reprinted from [5] with permission. Copyright © 2020 by Annual Reviews.

5.1.2 RPTPγ ensures prompt phosphorylation response of EGFR

The expression level of RPTPγ was found to be one of the most important factors that not only controls the pre-growth factor activation of EGFR but it also alters the way EGFR responds to different concentrations of EGF. The lack of RPTPγ either by knock-out in MCF7 cells or intrinsically in HT29 cells results in hampered growth factor sensing albeit the ligand binding kinetics remained similar to MCF7 WT cells (Figure 21C, Figure 22D). Since the system was already in a high-activity state prior to growth factor stimulus, the phosphorylation of EGFR remained constitutively high even after the treatment of supersaturating doses of EGF. The ectopic expression of RPTPγ to MCF7-RPTPγ-KO cells restored the coupling between EGFR-RPTPγ by moving the system to the bistable region of the 3D bifurcation diagram (Figure 22C: yellow, Figure 22D, Figure 30). Due to the enzymatic regulation by RPTPγ on the autocatalysis, EGFR maintained a low-inactive state and responded in a switch-like manner upon attaining critical EGF binding to EGFR (~18-20%). An important facet of EGFR-RPTPγ interaction is to maintain the system in a low-activity state and allow for its full activation at very low

EGFR ligand occupancies. At these conditions, prompt activation of the system is accomplished by autocatalytically activated EGFR monomers. This emphasizes the major role of EGFR monomers in achieving efficient system activation as opposed to the commonly described fundamental role of EGFR dimers. By coupling with autocatalysis, EGFR-RPTPγ interaction forms a central network motif that stages the system at criticality and allows for its optimal sensing of physiological growth factors[138,166].

These results are in line with the previously demonstrated regulation of EGFR response as a function of RPTPγ expression[138]. Although the study showed, pre-activation of EGFR upon siRNA induced knock-down (KD) of RPTPγ, the phosphorylation levels of pre-activated EGFR varied across the cell-population to a greater extent (0-90%). The variability was accounted to the non-uniform degree of RPTPγ-KD due to the limitations associated with siRNA (functioning on mRNA stage), which we overcame by the application of genetic level robust deletion by CRISPR-Cas9-KO. The lack of expression uniformity across the single cell derived colonies along with the clear readout for the fraction of phosphorylated EGFR by PTB-FLIM approach, increased the accuracy of relating the EGFR phosphorylation directly to the induced genetic perturbation in RPTPγ.

Additionally, RPTPγ-KO demonstrated an implication of RPTPγ expression on the regulation of EGFR at structural interaction level. EGFR-mCitrine could not attain its usual PM localization in MCF7-RPTPγ-KO cells, reported here for the first time in association with the loss of RPTPγ. A majority of EGFR-mCitrine in the absence of RPTPγ was found to be associated with the ER and only a small fraction was on the PM (Figure 21A). Probable hypotheses for this mis-localization could be the requirement of RPTPγ for EGFR to emerge from the ER post its synthesis or the necessity of its interaction with RPTPγ to keep EGFR on the PM. The PM localization of EGFR was restored upon the expression of RPTPγ to these cells, proving the consequences of RPTPγ expression on EGFR growth factor sensing as well as on its subcellular localization. Such pre-activation and mis-localization of EGFR was reported to take place when the extracellular domain (ECD) of EGFR was deleted[167]. This was attributed to the lack of autoinhibitory interactions in intracellular domains as a consequence of the absence of ECD-PM interactions that resist the attainment of active conformation. On the similar lines, presence of such interactions between EGFR and RPTPγ on the level of ECDs or other structural domains might be responsible for maintaining PM-localization of EGFR and its EGF-responsiveness.

5.2 Oxidation of RPTPγ enables EGFR activation at the PM

The strong phosphatase activity of RPTPγ upholds its prime role in the suppression of EGFR activation. However, the way it allows for the EGFR activation upon a certain threshold of EGF binding requires a coupling mechanism that inhibits RPTPγ activity and facilitates simultaneous signal propagation by EGFR. Considering the ultrasensitive nature of the regulation, we explored whether the EGF induced ROS production is responsible for controlling the catalytic activity of RPTPγ.

5.2.1 DyTo-FLIM for the live-cell imaging of oxidized RPTPγ

By using dimedone based IP-WB, we demonstrated that the catalytic cysteine of RPTPγ undergoes EGF dependent oxidation. However, it could not provide spatial information on single cell spatial landscape of RPTPγ oxidation that was necessary to decipher the relation between EGFR activity cycle and RPTPγ regulation. Considering the success of the dimedone based approaches in exhibiting their specificity for the detection of cysteine oxidation, we chose its derivative DYn-2 as a nucleophilic moiety for the formulation of an in-house probe. For live cell imaging, DYn-2 was coupled to atto590 by azide-alkyne cycloaddition to yield DyTo. Although DyTo binds to all the molecules that exhibit cysteine sulfenic acid modification to separate the oxidized proteins from the reduced pool, it does not specifically target a single protein of interest. Therefore, we tagged the protein of interest (here, RPTPγ) with mCitrine and utilized FRET-FLIM approach to spatially resolve the oxidized fraction. mCitrine due to its pH stability, monoexponential fluorescence decay profile and spectral overlap with atto590 turned out to be an excellent choice as a donor molecule for accurate quantification of interacting species. The extent of the binding of DyTo to cysteine sulfenic acid of RPTPγ-mCitrine mirrored the fraction of oxidized RPTPγ by attaining decreased donor lifetime.

The DyTo-based approach not only detected the oxidized RPTPγ in living cells but also enabled the spatial mapping of RPTPγ oxidation (Figure 24A). Probing the oxidation of the protein of interest in a live-cell has been a topic of curiosity over the past few years considering the implications of redox-signaling in cellular processes[168,169]. However, most of the techniques used previously had limited applicability to selectively trace the dynamics of intracellular protein oxidation due to their lack of single cell level resolution and unsuitability for the live-cells[116]. The attempts to obtain spatial information on the protein oxidation rely on fixed cell imaging that may introduce experimental artefacts[120]. The topic was also featured in *Science Signaling* editorial in which the tyrosine phosphatase oxidation from the perspective of regulatory mechanism as well as detection method was mentioned to be one of the most awaited developments in the signaling field[170]. In that context, we present DyTo-FLIM as a novel live-cell imaging technique that can provide real-time spatial dynamics of an oxidized protein.

The resolution offered by DyTo enabled us to image the RPTPγ oxidation taking place at the PM in response to EGF, distinctly separated from its cytosolic reduced fraction (Figure 24C, Figure 25A). By elucidating the spatial aspect of RPTPγ oxidation, we established that the EGF induced ROS production is localized specifically near the PM and regulates the catalytic activity of RPTPγ by reversible cysteine oxidation. Such a localized redox-regulation of PTPs by growth factor induced ROS is described for SHP2 on early endosomes[95]. Notably, for the first time, we demonstrate EGF dependent localized ROS production that causes RPTPγ oxidation in live cell.

5.2.2 Redox-coupled RPTPγ and EGFR establish a toggle switch interregulation

Using live-cell RPTPγ oxidation imaging, we uncovered the mechanism of RPTPγ oxidation as a function of EGFR activity. At low concentrations of EGF, RPTPγ retained its catalytically active-reduced state whereas upon reaching a threshold concentration of EGF, RPTPγ rapidly attained catalytically

inactive-oxidized state (Figure 25A). The EGF response profiles of RPTPγ oxidation and EGFR phosphorylation (Figure 22 B, C: yellow) showed analogous ultrasensitivity at critical EGF-binding (~20 ng/ml EGF, corresponding to 18-20% EGFR occupancy). Such coherence in response dynamics proves strong regulatory coupling between RPTPγ and EGFR activities (Figure 31). By causing inhibition of RPTPγ catalytic functionality, EGF induced ROS serves as a signaling molecule that promotes EGFR signaling at the PM. RPTPγ does not undergo catalytic cysteine oxidation and keeps exerting its strong phosphatase activity to prohibit EGFR autocatalysis until it reaches a ligand occupancy at which a burst of ROS is generated. ROS production results in RPTPγ oxidation that releases the inhibitory check of RPTPγ on EGFR autocatalytic site and triggers its robust activation. This mutual-regulation gives rise to a toggle switch network topology that generates system properties such that the spurious activation of EGFR is suppressed with RPTPγ enzymatic activity, and its prompt growth factor response is ensured with EGFR kinase activity dependent RPTPγ inhibition.

Referring to the 3D bifurcation diagram (Figure 30), it might occur that exogenous expression of RPTPγ to low RPTPγ-expressing MCF7 cells should shift the system more towards the monostable region (to the right) from the bistable region. However, the EGFR phosphorylation profiles demonstrated sharper EGF dose response for exogenous RPTPγ expressing cells than MCF7 WT cells. The sharper-switch like response indicates the bistable nature of the system and even tighter coupling (Figure 12B), meaning the shift towards bistability. Such a system dynamics could be explained by the regulation of RPTPγ by oxidation[101]. Since the rate of RPTPγ inhibition by cysteine oxidation depends on EGFR kinase activity mediated ROS production, it shows the coupling strength between these two regulatory species. One of the criteria that needs to be fulfilled for bistability is that the rate of inactivation of PTPs should exceed their rate of reactivation. According to mass action kinetics, the rate of RPTPγ oxidation increases as the expression level of RPTPγ goes higher, which strengthens the coupling. Moreover, the exogenous expression of RPTPγ can saturate the endocytic machinery[171]. This lowers the recycling rate of RPTPγ resulting in its higher steady state retainment on the PM. Therefore, by coupling with the catalytic activity of RPTPγ, the ROS regulated toggle switch gives rise to ultrasensitive response properties of EGFR.

5.2.3 EGFR activation relies on NOX-activity induced RPTPγ oxidation

We show that, EGF induced ROS production at the PM takes place via the activation of NOX-complexes. $p22^{phox}$- a common non-redundant subunit of NOX1-3, served as an essential factor that controls the ROS generation at the PM. In cells devoid of $p22^{phox}$, the EGF dependent oxidation of RPTPγ was completely abolished (Figure 25B). Concomitantly, the treatment with increasing concentrations of EGF could hardly activate EGFR in these cells (Figure 25C), justifying the toggle switch interregulation. The previous studies that attempted to relate EGF induced ROS with the oxidation of PTPs and activation of EGFR were based on non-specific strategies to block the NOX-activation e.g., usage of inhibitors like DPI[101,138]. Although, the NOX-inhibition was shown to decrease the EGF dependent oxidation of RPTPγ and oppose the autocatalytic activation of EGFR; it still could

not abolish the NOX-activity completely and the extent of effect was variable across the cell population. Such artefacts are often associated with the varied cell-to-cell efficacy associated with inhibitors, that are completely avoided by CRISPR-Cas9 induced genomic deletion, used in the current study.

We further show that, for the activation of EGFR, oxidation of RPTPγ is a crucial step that withholds the phosphatase activity of RPTPγ and allows for the EGFR kinase activity to take over. In the absence of active NOX-complex, the lack of ROS production keeps RPTPγ in a constitutive active catalytic state and thereby obstructs the EGFR activation upon growth factor binding. Interestingly, even upon treatment with saturating concentrations of EGF to achieve maximum dimerization, the phosphorylation of EGFR failed to register remarkable increase in MCF7-$p22^{phox}$-KO cells as compared to MCF7 cells. This unfolded a novel feature of RPTPγ redox regulation that extends the toggle switch beyond the activity of EGFR monomers to the activity regulation of EGFR dimers. The level of acute regulation exhibited by NOX-complexes proved their function as crucial regulators of EGFR activation that can block the EGFR signal propagation.

Elevated intracellular ROS accumulation is often observed in cancer cells that can make these cells resistant to external stresses and adapt their metabolism to promote cell proliferation and survival[172,173]. In HER2-amplified breast cancers, ROS is shown to promote conversion of fibroblasts into highly migrating myofibroblasts by inducing chemokines like CXCL12[174]. Amplified mitochondrial ROS generation is observed to be essential for KRas-dependent cell proliferation and tumorigenesis[175]. On the similar lines, inflammation induced cell adaptation to higher ROS levels can affect the response properties of the EGFR-PTP system. In these circumstances, PTPs regulating EGFR activation and signaling can undergo cysteine oxidation and attain catalytically inactive forms. The lack of dephosphorylating activities on EGFR can drive it to pre-activation state and cause its aberrant signaling activation. This can lead the system to lose its ability to sense and respond to the physiological growth factors. Such a system can stay in the mode of constitutive signaling which can further contribute to tumorigenesis by activating proliferation and migration inducing mechanisms. However, apart from the ROS production the extent of ROS induced abnormalities caused in the system can strongly depend on the antioxidant landscape in the cell and its vesicular trafficking machinery, which are often altered in diametrically opposite ways in different malignancies.

In recent years, NOX-induced ROS production has been described in a positive light due to its major role in immune cells like neutrophils that attack invading pathogens in the blood stream. NOX-assembly in neutrophil-phagosomes leads to production of a burst of high concentrations ROS, that causes breakdown of engulfed pathogens. In addition, these cells need ROS for the generation and release of neutrophil extracellular traps (NETs) containing antimicrobial peptides. Evidently, prominent presence of NETs is found near inflammation sites whereas mutations in NOX-associated genes are linked with an inability to form NETs and higher susceptibility to bacterial and fungal infections[176,75]. As opposed to the bulk production of ROS in these phagocytes, here we demonstrate highly localized ROS generation by NOX-complexes. In contrast to slow diffusing cytosolic proteins, ROS (like H_2O_2) have much larger diffusion coefficients, thereby they can propagate information rapidly via diffusion. The PM-bound NOX-complexes act as a source of ROS whereas a vast pool of antioxidants in the cytosol acts as a sink by

participating in scavenging-reactions with ROS. This generates a descending spatial gradient of ROS concentration and an ascending gradient of PTP activity from the PM to the cytosol[177]. This is aptly reflected from the results showing high EGF-dependent oxidation of the PM-proximal fraction of RPTPγ and TCPTP in comparison to their PM-distal subpopulations. Such a gradient of ROS also provides an explanation for the spatial signal propagation of EGFR. On one hand it facilitates the quick activation of EGFR at the PM by the oxidation of PTPs and on the other hand it controls the signaling of EGFR in the cytoplasm by maintaining high activity of PTPs. The radial length and the steepness of the gradient depends on the local concentrations of ROS and antioxidants, which dictate the local balance between EGFR and PTP activities resulting in the regulation of the temporal scale of EGFR signaling. These findings prove the essential role of PM-localized ROS in regulating localized protein activities and demonstrate the function of ROS as signaling molecules that can fine-tune the regulatory networks in non-phagocytic cells. Moreover, the mechanism of EGFR activity dependent ROS production as a means of propagating EGFR-signaling, presents it as a self-referencing system[177] and contributes further to our knowledge of RTK-ROS interaction.

5.3 Vesicular recycling spatially organizes oxidation-reduction and phosphorylation-dephosphorylation cycles

Depending on the EGF concentration, EGFR on the PM can attain varied proportion of monomeric or dimeric population. EGFR monomers undergo recycling via Rab11-positive RE whereas EGF-bound dimers take the path of unidirectional degradation via Rab7-positive LE[50]. Vesicular trafficking establishes interactions of active EGFR to ER-PTPs like TCPTP, which regulate the duration of signaling by dephosphorylating the endocytosed monomeric and dimeric EGFR[138]. However, the endocytic route of RPTPγ and its involvement in the regulation of endosomal EGFR was still unknown. We studied the aspects of vesicular trafficking to map the causal interactions between EGFR-RPTPγ/TCPTP and explored the dynamic nature of the interregulation.

5.3.1 TCPTP modulates the EGFR signaling response

Single cell phosphorylation response experiments showed that, the knock-out of *PTPN2*, resulted in the pre-activation of the system, although EGFR phosphorylation increased further upon high dose EGF treatment and showed a steep response profile (Figure 28B: green). The pre-stimulus active state of EGFR highlighted the function of TCPTP in maintaining the low activity level of EGFR. Such constrain on the system could be accounted to the role of TCPTP in dephosphorylating the constitutively recycling EGFR monomers and assuring their deactivation upon their return to the PM[138]. The lack of spatially established negative feedback from TCPTP forced the system to stay active, substantiating its regulatory function in attaining system reversibility. The re-introduction of TCPTP to the knock-out cells, reverted the EGFR activity to a basal low level. Additionally, the maximum attainable EGFR phosphorylation settled at lower level of saturation plateau (Figure 28B: magenta) than in MCF7 cells (Figure 28B: red), upon exogenous TCPTP expression. This demonstrated another important function of TCPTP, that is to modulate the phosphorylation of EGFR due to its catalytic interaction with dimeric EGFR formed at higher EGF concentrations.

Since the ER distribution of TCPTP spans from the perinuclear envelope to near the PM, we also examined the aspect of EGFR activity dependent regulation of TCPTP as a consequence of PM-localized ROS production. Previously, the lack of a suitable single cell technique prevented us from obtaining the information on the spatial regulation of TCPTP oxidation. With DyTo-live cell imaging, a spatially segregated population of highly oxidized TCPTP was observed in the vicinity of the PM at saturating EGF concentrations whereas a low-uniform level of oxidation was maintained at low doses (Figure 29B). The constitutive mild-oxidation of TCPTP might be one of the factors that contribute to the signaling of the endocytosed phosphorylated EGFR. Such a spatial organization of enzyme-substrate interaction can build a gradient of EGFR signaling that prevents its immediate signal quenching and allows for cytoplasmic signal propagation[59]. The extent of oxidation is a key factor that can contribute to the timeframe of EGFR signaling. In its active state, TCPTP situated on the PM-vicinal part of ER can engage in similar regulatory function as RPTPγ by forming a double negative feedback causality and hindering the activation EGFR. Higher oxidation of this fraction at saturating concentrations of EGF can prevent it from exerting its catalytic activity on EGFR and promote signaling at the PM.

5.3.2 RPTPγ interacts with monomeric EGFR

By immunostaining against the endosomal compartmental markers, we found that RPTPγ traffics through Rab11-positive endosomes (Figure 17B and Figure 18). Irrespective of the growth factor stimulus, RPTPγ was seen to reserve the route of vesicular recycling and completely renounce the passage through Rab7-positive LE unlike EGFR at saturating EGF treatment. Interaction of RPTPγ with ligandless EGFR was observed on the PM as well as on the RE. The PM-based constitutive interaction between RPTPγ and monomeric EGFR further propagated to the cytosol due to their vesicular co-trafficking. The entry of RPTPγ to RE was further substantiated by proportionately increased influx of RPTPγ to RE with exogenous expression of RE biogenesis inducing Rab11. On the other hand, by utilizing a photoactivable form of RPTPγ we demonstrated the return of RE-situated pool of RPTPγ to the PM. These results proved that RPTPγ maintains constitutive recycling with or without growth factor treatment. Nevertheless, the treatment with EGF caused higher PM return of RPTPγ after its initial internalization. The additional recovery of RPTPγ at the PM could be traced back to the RE-situated pool of RPTPγ that was directed through recycling route. The plausible reason for this could be the activation of Akt upon EGF treatment that is known to be involved in inter-compartmental exchange and fusion of endocytic vesicles with the PM[47].

The immunoprecipitation as well as immunostaining experiments proved the interaction of RPTPγ with EGFR at low EGF doses and its loss upon saturating treatment of EGF (Figure 15, Figure 17). Although RPTPγ maintained its continuous recycling through RE, at growth factor conditions favorable to dimer formation (saturating concentrations), the ligand bound EGFR was driven to LE causing the disruption in EGFR-RPTPγ interaction. Another probable reason for the loss of interaction can be an EGFR dimerization induced change in the structural conformation that results in the rearrangement of interacting domains[18]. The dynamic nature of the interaction became clearer from the STMs of the high

temporal resolution images of the translocation of EGFR and RPTPγ. Under stimulus conditions at which a substantial population of EGFR was in monomeric form, EGFR and RPTPγ both showed internalization at similar time scales and subsequent recovery at the PM. Such a trend was observed upon 5 mins pulse of EGF (sub-saturating as well as saturating) or sustained treatment of sub-saturating EGF (Figure 16 C, D, A). The PM-temporal dynamics of EGFR and RPTPγ exhibited analogous profiles, further substantiating the interaction between monomeric EGFR and RPTPγ. The sustained EGF-treatment (Figure 16 A, B) maintained continuous EGFR activity to accelerate the recycling of pre-existing endosomal RPTPγ, aptly reflected from the higher relative amount of RPTPγ that reverted back to the PM. The STM profiles of RPTPγ and EGFR showed maximum disparity when the cells were exposed to sustained saturating EGF. Here, the dimerization of EGFR drove the receptors on the path of continuous ubiquitin dependent degradation[50]. As predicted from our previous conclusions, RPTPγ did not interact with this fraction and followed the recycling route alone.

5.3.3 Redox cycle of RPTPγ is regulated by EGFR activity and endocytosis

Previous studies have characterized the role of vesicular trafficking as a means to distribute EGFR to different spatial compartments so to generate its activity gradient and regulate its signaling duration by transporting it to ER-based PTPs[50,138]. However, the impact of vesicular trafficking on RPTPγ activity and on its interaction with EGFR was still unknown. We revealed the vesicular recycling route of RPTPγ for the first time in this study (Figure 15, Figure 16, Figure 17). On these lines, we further elaborated the utility of this mechanism in restoring RPTPγ activity post EGF induced oxidation.

The temporal mapping of RPTPγ oxidation post EGF stimulus showed that the redox state of RPTPγ is strongly coupled to the activity of EGFR. The oxidation of RPTPγ attained its maximum at the PM on the timescales comparable to the peak of ligand induced EGFR phosphorylation. The oxidation subsequently dropped back to the basal level when the system was deprived of EGF or underwent EGFR depletion (Figure 26, Figure 27). When continuous EGFR activity was maintained by providing low sustained treatment of EGF, oxidation of RPTPγ remained well above the basal level due to EGF-induced activity of recycled EGFR. The fraction of RPTPγ on endosomes stayed reduced and this fraction increased post growth factor accelerated endocytosis of RPTPγ. Moreover, the recycled RPTPγ that eventually regained its PM localization was observed in reduced state in the absence of growth factor treatment. These observations led us to understand the reduction mechanism of RPTPγ. The ROS gradient from the PM to the cytosol provides a localized oxidizing zone surrounded by vast reducing environment which reduces endosomal RPTPγ. Vesicular trafficking machinery carries the PM bound RPTPγ to RE and exposes the oxidized RPTPγ to an outspread pool of reducing agents in the cytoplasm[93]. These proteins reduce RPTPγ with commonly established mechanisms such as glutathione redox system, and RPTPγ is carried back to the PM in the reduced state with its restored catalytic activity.

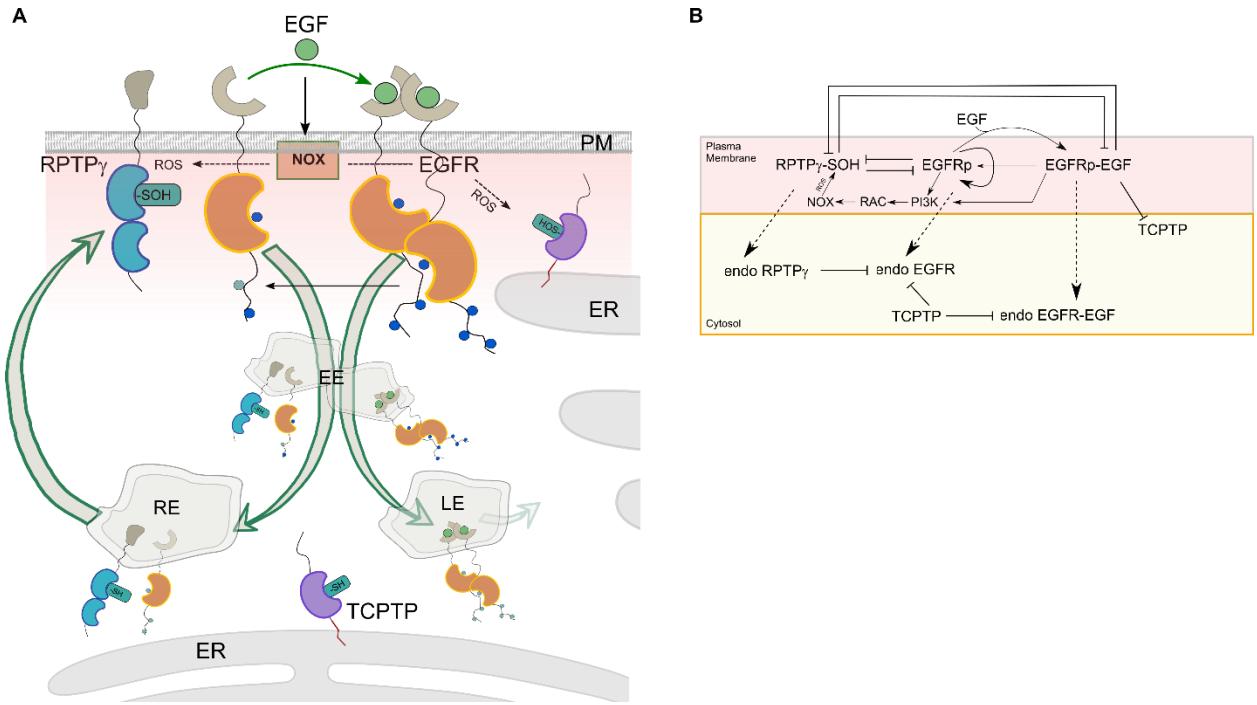

Figure 31: EGF-dependent vesicular dynamics integrate RPTPγ redox regulation with EGFR activity

(A) Schematic of spatially spanning EGFR-PTP interactions. EGFR and RPTPγ mutually regulate their activities through EGF-dependent ROS production by the NOX-complexes at the plasma membrane (PM). Vesicular co-trafficking of active monomeric-EGFR (blue circles) and RPTPγ extend their PM-based interaction to recycling endosomes (RE). Cytosolic exposure converts the oxidized cysteine (-SOH) of RPTPγ to active-reduced state (-SH) so as to continue its phosphatase activity on endosomal EGFR monomers (cyan circles) along with TCPTP on the ER. Recycling of RPTPγ and EGFR to the PM restores their regulatory interactions. EGF-bound dimerized EGFR further ensures its activation at the PM by elevating the oxidation of PM-proximal TCPTP (-SOH) and undergoes signal termination upon its contact with PM-distal TCPTP. **(B)** Causality diagram for the interactions in scheme (A). ROS induced activity regulation of RPTPγ forms a double-negative feedback with monomeric EGFR and dimeric EGFR at the PM. Reduced endocytosed RPTPγ exerts its negative regulation on co-trafficking EGFR along with TCPTP on the ER. Dimeric EGFR exhibits negative regulation on PM vicinal TCTPT via ROS and negative feedback through vesicular trafficking.

In this manner, vesicular recycling recovers the active state of RPTPγ post ROS induced catalytic site inhibition. It reestablishes the enzymatic check of RPTPγ on EGFR after the removal of growth factor stimuli. Moreover, the ligand independent constitutive recycling of RPTPγ does not let the system to deplete RPTPγ from the PM and stage the system at criticality to ensure that EGFR responds to physiological growth factor cues[138,166]. An important feature of this system is to synchronize the phosphorylation-dephosphorylation cycle of EGFR to the oxidation-reduction cycle of RPTPγ (Figure 31). Looking at the trafficking profiles of RPTPγ and monomeric EGFR, it could be deduced that the interaction between them continues also on endosomal compartments. The reduction of RPTPγ upon endocytosis makes it capable of exerting negative regulation on phosphorylated colocalized EGFR, thereby adding a dimension of spatial regulation to the RPTPγ and EGFR toggle switch. Such an interaction does not take place with EGF bound dimeric EGFR, thereby sparing this fraction of receptors from dephosphorylating regulation by RPTPγ on endosomes. Along the similar lines, EGFR dimers (and not monomers) have been shown to signal efficiently on endosomes and are linked to the activation of

proliferation inducing subcellular soluble-ERK[1], which would have been difficult in the spatial vicinity of catalytically active RPTPγ. Evidently, recycling of RPTPγ and monomeric-EGFR back to the PM continues the recursive interactions between them to stage the system at the disposal of growth factor sensing.

5.4 Broader perspective

In summary, we prove that RPTPγ works as a major regulator of EGFR growth factor sensitivity and signaling response. The lack of RPTPγ regulation pushes EGFR associated signaling in a state of constitutive activity, projecting RPTPγ as a tumor suppressor that possesses potential applicability in terms of addressing EGFR associated malignancies. Another notable aspect that we decipher is the regulation of RPTPγ catalytic cysteine oxidation as a requisite for EGFR activation. The essential player here is $p22^{phox}$, that controls the EGF induced activation of NOX-complexes responsible for the redox-regulation of RPTPγ. Activation of EGFR is completely inhibited upon the loss of $p22^{phox}$, making it a therapeutic target of interest to inhibit EGFR signaling.

By showing the EGFR activity dependent oxidation of RPTPγ at the PM and its reduction in the cytoplasm, we demonstrated the function of ROS as a target specific signaling molecule over the popular notion of DNA damaging antagonist. Additionally, the imaging technique DyTo-FLIM presented in the thesis can be applied for mapping the wide array of oxidized proteins in living cell without perturbing the redox-microenvironment. We unravel the spatial dimension of RPTPγ-EGFR regulation by elucidating the vesicular co-recycling route for RPTPγ and EGFR. The mechanism serves as a means for reducing RPTPγ and dephosphorylating monomeric-EGFR, thereby integrating the activity regulation of interacting species in the same spatial cycle. Although our inferences present an outlook into the regulation of EGFR activity by redox-coupling with RPTPγ activity, their applicability in physiological situations should be elaborated in complex three-dimensional tissue structures like organoids.

References

1. Brüggemann, Y., Karajannis, L. S., Stanoev, A., Stallaert, W. & Bastiaens, P. I. H. Growth factor–dependent ErbB vesicular dynamics couple receptor signaling to spatially and functionally distinct Erk pools. *Sci. Signal.* **14**, eabd9943 (2021).

2. Ferrell, J. E. Self-perpetuating states in signal transduction: Positive feedback, double-negative feedback and bistability. *Curr. Opin. Cell Biol.* **14**, 140–148 (2002).

3. Santos, S. D. M., Verveer, P. J. & Bastiaens, P. I. H. Growth factor-induced MAPK network topology shapes Erk response determining PC-12 cell fate. *Nat. Cell Biol.* **9**, 324–330 (2007).

4. Koseska, A. & Bastiaens, P. I. Cell signaling as a cognitive process. *EMBO J.* **36**, 568–582 (2017).

5. Koseska, A. & Bastiaens, P. I. H. Processing Temporal Growth Factor Patterns by an Epidermal Growth Factor Receptor Network Dynamically Established in Space. *Annu. Rev. Cell Dev. Biol.* (2020). doi:10.1146/annurev-cellbio-013020-103810

6. Stallaert, W. *et al.* Contact inhibitory Eph signaling suppresses EGF-promoted cell migration by decoupling EGFR activity from vesicular recycling. *Sci. Signal.* (2018). doi:10.1126/scisignal.aat0114

7. Sibilia, M. & Wagner, E. F. Strain-dependent epithelial defects in mice lacking the EGF receptor. *Science (80-.).* **269**, 234–238 (1995).

8. Miettinen, P. *et al.* Epithelial immaturity and multiorgan failure in mice lacking epidermal growth factor receptor. *Nature* **376**, 337–341 (1995).

9. Paria, B. C., Das, S. K., Andrews, G. K. & Dey, S. K. Expression of the epidermal growth factor receptor gene is regulated in mouse blastocysts during delayed implantation. *Proc. Natl. Acad. Sci. U. S. A.* **90**, 55–59 (1993).

10. Threadgill, D. W. *et al.* Targeted disruption of mouse EGF receptor: Effect of genetic background on mutant phenotype. *Science (80-.).* **269**, 230–234 (1995).

11. Sebastian, J. *et al.* Activation and function of the epidermal growth factor receptor and erbB-2 during mammary gland morphogenesis. *Cell Growth Differ.* **9**, 777–785 (1998).

12. Robson, J. P. *et al.* Impaired neural stem cell expansion and hypersensitivity to epileptic seizures in mice lacking the EGFR in the brain. *FEBS J.* **285**, 3175–3196 (2018).

13. Kornblum, H. I. *et al.* Abnormal astrocyte development and neuronal death in mice lacking the epidermal growth factor receptor. *J. Neurosci. Res.* **53**, 697–717 (1998).

14. Da Cunha Santos, G., Shepherd, F. A. & Tsao, M. S. EGFR mutations and lung cancer. *Annu.*

Rev. Pathol. Mech. Dis. **6**, 49–69 (2011).

15. Nicholson, R. I., Gee, J. M. W. & Harper, M. E. EGFR and cancer prognosis. *Eur. J. Cancer* **37**, 9 (2001).

16. Ullrich, A. & Schlessingert, J. Signal Transduction by Receptors with Tyrosine Kinase Activity. *Cell* **61**, 203–212 (1990).

17. Lemmon, M. A. & Schlessinger, J. Cell signaling by receptor tyrosine kinases. *Cell* **141**, 1117–1134 (2010).

18. Ferguson, K. M. *et al.* EGF activates its receptor by removing interactions that autoinhibit ectodomain dimerization. *Mol. Cell* **11**, 507–517 (2003).

19. Claesson-Welsh, L. SIGNAL RECEPTORS BY THE PDGF Lena Claesson-Welsh. *Prog. Growth Factor Res.* **5**, 37–54 (1994).

20. Lee, J. & Pilch, P. F. The insulin receptor: structure, function, and signaling. *Am. J. Physiol. Physiol.* **266**, C319–C334 (1994).

21. Li, J., Choi, E., Yu, H. & Bai, X. chen. Structural basis of the activation of type 1 insulin-like growth factor receptor. *Nat. Commun.* **10**, (2019).

22. Arteaga, C. L. & Engelman, J. A. ERBB receptors: From oncogene discovery to basic science to mechanism-based cancer therapeutics. *Cancer Cell* **25**, 282–303 (2014).

23. Lee, K.-F. *et al.* Requirement for neuregulin receptor erbB2 in neural and cardiac development. *Nature* **378**, 25–78 (1995).

24. Erickson, S. L. *et al.* ErbB3 is required for normal cerebellar and cardiac development: A comparison with ErbB2- and heregulin-deficient mice. *Development* **124**, 4999–5011 (1997).

25. Gassmann, M. *et al.* Aberrant neural and cardiac development in mice lacking the ErbB4 neuregulin receptor. *Nature* **378**, 390–394 (1995).

26. Freed, D. M. *et al.* EGFR Ligands Differentially Stabilize Receptor Dimers to Specify Signaling Kinetics. *Cell* **171**, 683-695.e18 (2017).

27. Sweeney, C. & Carraway, K. L. Ligand discrimination by ErbB receptors: Differential signaling through differential phosphorylation site usage. *Oncogene* **19**, 5568–5573 (2000).

28. Lax, I. *et al.* Functional analysis of the ligand binding site of EGF-receptor utilizing chimeric chicken/human receptor molecules. *EMBO J.* **8**, 421–427 (1989).

29. Garrett, T. P. J. *et al.* Crystal structure of a truncated epidermal growth factor receptor extracellular domain bound to transforming growth factor α. *Cell* **110**, 763–773 (2002).

30. Zhang, X., Gureasko, J., Shen, K., Cole, P. A. & Kuriyan, J. An Allosteric Mechanism for Activation of the Kinase Domain of Epidermal Growth Factor Receptor. *Cell* (2006).

doi:10.1016/j.cell.2006.05.013

31. Wagner, M. J., Stacey, M. M., Liu, B. A. & Pawson, T. Molecular mechanisms of SH2- and PTB-Domain-containing proteins in receptor tyrosine kinase signaling. *Cold Spring Harb. Perspect. Biol.* **5**, 1–20 (2013).

32. Bajaj, M., Waterfield, M. D., Schlessinger, J., Taylor, W. R. & Blundell, T. On the tertiary structure of the extracellular domains of the epidermal growth factor and insulin receptors Mona. *Biochim. Biophys. Acta* **916**, 220–226 (1987).

33. Ogiso, H. *et al.* Crystal structure of the complex of human epidermal growth factor and receptor extracellular domains. *Cell* **110**, 775–787 (2002).

34. Alvarado, D., Klein, D. E. & Lemmon, M. A. Structural basis for negative cooperativity in growth factor binding to an EGF receptor. *Cell* **142**, 568–579 (2010).

35. Ichinose, J., Murata, M., Yanagida, T. & Sako, Y. EGF signalling amplification induced by dynamic clustering of EGFR. *Biochem. Biophys. Res. Commun.* **324**, 1143–1149 (2004).

36. Salazar-Cavazos, E. *et al.* Multisite EGFR phosphorylation is regulated by adaptor protein abundances and dimer lifetimes. *Mol. Biol. Cell* **31**, 695–708 (2020).

37. Shan, Y., Arkhipov, A., Kim, E. T., Pan, A. C. & Shawa, D. E. Transitions to catalytically inactive conformations in EGFR kinase. *Proc. Natl. Acad. Sci. U. S. A.* **110**, 7270–7275 (2013).

38. Baumdick, M. *et al.* A conformational sensor based on genetic code expansion reveals an autocatalytic component in EGFR activation. *Nat. Commun.* **9**, (2018).

39. Osherov, N. & Levitzki, A. Epidermal-growth-factor-dependent activation of the Src-family kinases. *Eur. J. Biochem.* **1053**, 1047–1053 (1994).

40. Sato Ken-ichi, Sato, A., Aoto, M. & Fukami, Y. Site-specific association of c-Src with epidermal growth factor receptor in A431 cells. *Biochem Biophys Res Commun* **210**, 844–851 (1995).

41. Kovacs, E. *et al.* Analysis of the Role of the C-Terminal Tail in the Regulation of the Epidermal Growth Factor Receptor. *Mol. Cell. Biol.* **35**, 3083–3102 (2015).

42. Shan, Y. *et al.* Oncogenic mutations counteract intrinsic disorder in the EGFR kinase and promote receptor dimerization. *Cell* **149**, 860–870 (2012).

43. Yamazaki, T. *et al.* Role of Grb2 in EGF-stimulated EGFR internalization. *J. Cell Sci.* **115**, 1791–1802 (2002).

44. Rappoport, J. Z. & Simon, S. M. Endocytic trafficking of activated EGFR is AP-2 dependent and occurs through preformed clathrin spots. *J. Cell Sci.* **122**, 1301–1305 (2009).

45. Goh, L. K., Huang, F., Kim, W., Gygi, S. & Sorkin, A. Multiple mechanisms collectively regulate clathrin-mediated endocytosis of the epidermal growth factor receptor. *J. Cell Biol.* **189**, 871–

883 (2010).

46. Sigismund, S. *et al.* Clathrin-Mediated Internalization Is Essential for Sustained EGFR Signaling but Dispensable for Degradation. *Dev. Cell* **15**, 209–219 (2008).

47. Er, E. E., Mendoza, M. C., Mackey, A. M., Rameh, L. E. & Blenis, J. AKT Facilitates EGFR Trafficking and Degradation by Phosphorylating and Activating PIKfyve. *Sci. Signal.* **6**, (2013).

48. Nishimura, Y., Takiguchi, S., Ito, S. & Itoh, K. EGF-stimulated AKT activation is mediated by EGFR recycling via an early endocytic pathway in a gefitinib-resistant human lung cancer cell line. *Int. J. Oncol.* **46**, 1721–1729 (2015).

49. Levkowitz, G. *et al.* c-Cb1/Sli-1 regulates endocytic sorting and ubiquitination of the epidermal growth factor receptor. *Genes Dev.* **12**, 3663–3674 (1998).

50. Baumdick, M. *et al.* EGF-dependent re-routing of vesicular recycling switches spontaneous phosphorylation suppression to EGFR signaling. *Elife* **4**, 1–28 (2015).

51. Ullrich, O. *et al.* Rab GDP dissociation inhibitor as a general regulator for the membrane association of rab proteins. *J. Biol. Chem.* **268**, 18143–18150 (1993).

52. Ullrich, O., Reinsch, S., Urbé, S., Zerial, M. & Parton, R. G. Rab11 regulates recycling through the pericentriolar recycling endosome. *J. Cell Biol.* **135**, 913–924 (1996).

53. Zeigerer, A. *et al.* Rab5 is necessary for the biogenesis of the endolysosomal system in vivo. *Nature* **485**, 465–470 (2012).

54. Stenmark, H. Rab GTPases as coordinators of vesicle traffic. *Nat. Rev. Mol. Cell Biol.* **10**, 513–525 (2009).

55. Haj, F. G., Verveer, P. J., Squire, A., Neel, B. G. & Bastiaens, P. I. H. Imaging sites of receptor dephosphorylation by PTP1B on the surface of the endoplasmic reticulum. *Science (80-.).* **295**, 1708–1711 (2002).

56. Tiganis, T., Kemp, B. E. & Tonks, N. K. The protein-tyrosine phosphatase TCPTP regulates epidermal growth factor receptor-mediated and phosphatidylinositol 3-kinase-dependent signaling. *J. Biol. Chem.* **274**, 27768–27775 (1999).

57. Ibach, J. *et al.* Single particle tracking reveals that EGFR signaling activity is amplified in clathrin-coated pits. *PLoS One* **10**, 1–22 (2015).

58. Wang, Y., Pennock, S., Chen, X. & Wang, Z. Endosomal Signaling of Epidermal Growth Factor Receptor Stimulates Signal Transduction Pathways Leading to Cell Survival. *Mol. Cell. Biol.* **22**, 7279–7290 (2002).

59. Yudushkin, I. A. *et al.* Live-Cell Imaging of Enzyme-Substrate Interaction Reveals Spatial Regulation of PTP1B. *Science (80-.).* **315**, 115–119 (2007).

60. Andersen, J. N. *et al.* A genomic perspective on protein tyrosine phosphatases: gene structure, pseudogenes, and genetic disease linkage. *FASEB J.* **18**, 8–30 (2004).

61. Tonks, N. K. Protein tyrosine phosphatases: From genes, to function, to disease. *Nat. Rev. Mol. Cell Biol.* **7**, 833–846 (2006).

62. Streuli, M., Krueger, N. X., Thai, T., Tang, M. & Saito, H. Distinct functional roles of the two intracellular phosphatase like domains of the receptor-linked protein tyrosine phosphatases LCA and LAR. *EMBO J.* **9**, 2399–2407 (1990).

63. Blanchetot, C., Tertoolen, L. G., Overvoorde, J. & Den Hertog, J. Intra- and intermolecular interactions between intracellular domains of receptor protein-tyrosine phosphatases. *J. Biol. Chem.* **277**, 47263–47269 (2002).

64. Wallace, M. J., Fladd, C., Batt, J. & Rotin, D. The Second Catalytic Domain of Protein Tyrosine Phosphatase δ (PTPδ) Binds to and Inhibits the First Catalytic Domain of PTPς. *Mol. Cell. Biol.* **18**, 2608–2616 (1998).

65. Sap, J., Jiang, Y. P., Friedlander, D., Grumet, M. & Schlessinger, J. Receptor tyrosine phosphatase R-PTP-kappa mediates homophilic binding. *Mol. Cell. Biol.* **14**, 1–9 (1994).

66. Kulas, D. T., Goldstein, B. J. & Mooney, R. A. The transmembrane protein-tyrosine phosphatase LAR modulates signaling by multiple receptor tyrosine kinases. *J. Biol. Chem.* **271**, 748–754 (1996).

67. Bennett, A. M., Tang, T. L., Sugimoto, S., Walsh, C. T. & Neel, B. G. Protein-tyrosine-phosphatase SHPTP2 couples platelet-derived growth factor receptor β to Ras. *Proc. Natl. Acad. Sci. U. S. A.* **91**, 7335–7339 (1994).

68. Guan, K. & Dixon, J. E. Protein tyrosine phosphatase activity of an essential virulence determinant in Yersinia. *Science (80-.).* **249**, 553–556 (1990).

69. Pot, D. A. & Dixon, J. E. Active site labeling of a receptor-like protein tyrosine phosphatase. *J. Biol. Chem.* **267**, 140–143 (1992).

70. Zhang, Z. Y., Wang, Y. & Dixon, J. E. Dissecting the catalytic mechanism of protein-tyrosine phosphatases. *Proc. Natl. Acad. Sci. U. S. A.* **91**, 1624–1627 (1994).

71. Tautz, L., Critton, D. A. & Grotegut, S. *Protein Tyrosine Phosphatases: Structure, Function, and Implication in Human Disease*. *Methods in Molecular Biology* **1053**, (2013).

72. Liu, Z., Zhou, T., Ziegler, A. C., Dimitrion, P. & Zuo, L. Oxidative Stress in Neurodegenerative Diseases: From Molecular Mechanisms to Clinical Applications. *Oxid. Med. Cell. Longev.* **2017**, (2017).

73. Cadet, J. & Richard Wagner, J. DNA base damage by reactive oxygen species, oxidizing agents, and UV radiation. *Cold Spring Harb. Perspect. Biol.* **5**, 1–18 (2013).

74. Franchini, A. M., Hunt, D., Melendez, J. A. & Drake, J. R. FcγR-driven release of IL-6 by macrophages requires NOX2-dependent production of reactive oxygen species. *J. Biol. Chem.* **288**, 25098–25108 (2013).

75. Kenny, E. F. *et al.* Diverse stimuli engage different neutrophil extracellular trap pathways. *Elife* **6**, 1–21 (2017).

76. Suh, Y. A. *et al.* Cell transformation by the superoxide-generating oxidase Mox1. *Nature* **401**, 79–82 (1999).

77. Ambasta, R. K. *et al.* Direct interaction of the novel Nox proteins with p22phox is required for the formation of a functionally active NADPH oxidase. *J. Biol. Chem.* **279**, 45935–45941 (2004).

78. Bánfi, B., Clark, R. A., Steger, K. & Krause, K. H. Two novel proteins activate superoxide generation by the NADPH oxidase NOX1. *J. Biol. Chem.* **278**, 3510–3513 (2003).

79. Nisimoto, Y., Motalebi, S., Han, C. H. & Lambeth, J. D. The p67(phox) activation domain regulates electron flow from NADPH to flavin in flavocytochrome b558. *J. Biol. Chem.* **274**, 22999–23005 (1999).

80. Wientjes, F. B., Hsuan, J. J., Totty, N. F. & Segal, A. W. p40(phox), a third cytosolic component of the activation complex of the NADPH oxidase to contain src homology 3 domains. *Biochem. J.* **296**, 557–561 (1993).

81. El-Benna, J., Dang, P. M. C., Gougerot-Pocidalo, M. A., Marie, J. C. & Braut-Boucher, F. p47phox, the phagocyte NADPH oxidase/NOX2 organizer: Structure, phosphorylation and implication in diseases. *Exp. Mol. Med.* **41**, 217–225 (2009).

82. Park, H. S. *et al.* Sequential Activation of Phosphatidylinositol 3-Kinase, βPix, Rac1, and Nox1 in Growth Factor-Induced Production of H 2 O 2 . *Mol. Cell. Biol.* **24**, 4384–4394 (2004).

83. Fridovich, I. The biology of oxygen radicals. *Science (80-.).* **201**, 875–880 (1978).

84. Bánfi, B. *et al.* A Ca2+-activated NADPH Oxidase in Testis, Spleen, and Lymph Nodes. *J. Biol. Chem.* **276**, 37594–37601 (2001).

85. Cheng, G., Cao, Z., Xu, X., Meir, E. G. Van & Lambeth, J. D. Homologs of gp91 phox : cloning and tissue expression of Nox3 , Nox4 , and Nox5. *Gene.* **269**, 131–140 (2001).

86. Lassègue, B. *et al.* Novel gp91phox Homologues in Vascular Smooth Muscle Cells nox1 Mediates Angiotensin II–Induced Superoxide Formation and Redox-Sensitive Signaling Pathways. *Mol. Med.* 888–895 (2001).

87. De Deken, X. *et al.* Cloning of two human thyroid cDNAs encoding new members of the NADPH oxidase family. *J. Biol. Chem.* **275**, 23227–23233 (2000).

88. Bedard, K. & Krause, K. H. The NOX family of ROS-generating NADPH oxidases: Physiology and pathophysiology. *Physiol. Rev.* **87**, 245–313 (2007).

89. Yamasoba, T., Nuttall, A. L., Harris, C., Raphael, Y. & Miller, J. M. Role of glutathione in protection against noise-induced hearing loss. *Brain Res.* **784**, 82–90 (1998).

90. Rhee, S. G. Redox signaling: Hydrogen peroxide as intracellular messenger. *Exp. Mol. Med.* **31**, 53–59 (1999).

91. Ho Zoon Chae, Kim, I. H., Kim, K. & Sue Goo Rhee. Cloning, sequencing, and mutation of thiol-specific antioxidant gene of Saccharomyces cerevisiae. *J. Biol. Chem.* **268**, 16815–16821 (1993).

92. Preston, T. J., Muller, W. J. & Singh, G. Scavenging of Extracellular H2O2 by Catalase Inhibits the Proliferation of HER-2/Neu-transformed Rat-1 Fibroblasts through the Induction of a Stress Response. *J. Biol. Chem.* **276**, 9558–9564 (2001).

93. Williams, D. L., Bonilla, M., Gladyshev, V. N. & Salinas, G. Thioredoxin glutathione reductase-dependent redox networks in platyhelminth parasites. *Antioxidants Redox Signal.* **19**, 735–745 (2013).

94. Oakley, F. D., Abbott, D., Li, Q. & Engelhardt, J. F. Signaling components of redox active endosomes: The redoxosomes. *Antioxidants Redox Signal.* **11**, 1313–1333 (2009).

95. Tsutsumi, R. *et al.* Assay to visualize specific protein oxidation reveals spatio-temporal regulation of SHP2. *Nat. Commun.* **8**, 1–14 (2017).

96. Haque, A., Andersen, J. N., Salmeen, A., Barford, D. & Tonks, N. K. Conformation-sensing antibodies stabilize the oxidized form of PTP1B and inhibit its phosphatase activity. *Cell* **147**, 185–198 (2011).

97. Gniadecki, R., Christoffersen, N. & Wulf, H. C. Cholesterol-rich plasma membrane domains (lipid rafts) in keratinocytes: Importance in the baseline and UVA-induced generation of reactive oxygen species. *J. Invest. Dermatol.* **118**, 582–588 (2002).

98. Bae, Y. S. *et al.* Platelet-derived Growth Factor-induced H2O2 Production Requires the Activation of Phosphatidylinositol 3-Kinase. *J. Biol. Chem.* **275**, 10527–10531 (2000).

99. Bae, Y. S. *et al.* Epidermal Growth Factor (EGF)-induced Generation of Hydrogen Peroxide. *J. Biol. Chem.* **272**, 217–221 (1997).

100. Abo, A. *et al.* Activation of the NADPH oxidase involves the small GTP-binding protein p21rac1. *Nature* **353**, 668–670 (1991).

101. Reynolds, A. R., Tischer, C., Verveer, P. J., Rocks, O. & Bastiaens, P. I. H. EGFR activation coupled to inhibition of tyrosine phosphatases causes lateral signal propagation. *Nat. Cell Biol.* **5**, 447–453 (2003).

102. Denu, J. M. & Tanner, K. G. Specific and reversible inactivation of protein tyrosine phosphatases by hydrogen peroxide: Evidence for a sulfenic acid intermediate and implications for redox

regulation. *Biochemistry* **37**, 5633–5642 (1998).

103. Skorey, K. *et al.* How does alendronate inhibit protein-tyrosine phosphatases? *J. Biol. Chem.* **272**, 22472–22480 (1997).

104. Huyer, G. *et al.* Mechanism of inhibition of protein-tyrosine phosphatases by vanadate and pervanadate. *J. Biol. Chem.* **272**, 843–851 (1997).

105. Kwon, J. *et al.* Reversible oxidation and inactivation of the tumor suppressor PTEN in cells stimulated with peptide growth factors. *Proc. Natl. Acad. Sci. U. S. A.* **101**, 16419–16424 (2004).

106. Salmeen, A. *et al.* Redox regulation of protein tyrosine phosphatase 1B involves a sulphenyl-amide intermediate. *Nature* **423**, 769–773 (2003).

107. Ren, X. *et al.* Redox Signaling Mediated by Thioredoxin and Glutathione Systems in the Central Nervous System. *Antioxidants Redox Signal.* **27**, 989–1010 (2017).

108. Mahadev, K., Zilbering, A., Zhu, L. & Goldstein, B. J. Insulin-stimulated Hydrogen Peroxide Reversibly Inhibits Protein-tyrosine Phosphatase 1B in Vivo and Enhances the Early Insulin Action Cascade. *J. Biol. Chem.* **276**, 21938–21942 (2001).

109. Meng, T. C., Buckley, D. A., Galic, S., Tiganis, T. & Tonks, N. K. Regulation of insulin signaling through reversible oxidation of the protein-tyrosine phosphatases TC45 and PTP1B. *J. Biol. Chem.* **279**, 37716–37725 (2004).

110. Meng, T. C., Hsu, S. F. & Tonks, N. K. Development of a modified in-gel assay to identify protein tyrosine phosphatases that are oxidized and inactivated in vivo. *Methods* **35**, 28–36 (2005).

111. Boivin, B., Zhang, S., Arbiser, J. L., Zhang, Z.-Y. & Tonks, N. K. A modified cysteinyl-labeling assay reveals reversible oxidation of protein tyrosine phosphatases in angiomyolipoma cells. *Proc. Natl. Acad. Sci.* **105**, 9959–9964 (2008).

112. Boschi-Muller, S. *et al.* A sulfenic acid enzyme intermediate is involved in the catalytic mechanism of peptide methionine sulfoxide reductase from Escherichia coli. *J. Biol. Chem.* **275**, 35908–35913 (2000).

113. Ellis, H. R. & Poole, L. B. Novel application of 7-chloro-4-nitrobenzo-2-oxa-1,3-diazole to identify cysteine sulfenic acid in the AhpC component of alkyl hydroperoxide reductase. *Biochemistry* **36**, 15013–15018 (1997).

114. Saurin, A. T., Neubert, H., Brennan, J. P. & Eaton, P. Widespread sulfenic acid formation in tissues in response to hydrogen peroxide. *Proc. Natl. Acad. Sci. U. S. A.* **101**, 17982–17987 (2004).

115. Poole, L. B., Zeng, B. B., Knaggs, S. A., Yakubu, M. & King, S. B. Synthesis of chemical probes to map sulfenic acid modifications on proteins. *Bioconjug. Chem.* **16**, 1624–1628 (2005).

116. Poole, L. B. *et al.* Fluorescent and affinity-based tools to detect cysteine sulfenic acid formation

in proteins. *Bioconjug. Chem.* **18**, 2004–2017 (2007).

117. Young, H. S. & Carroll, K. S. Profiling protein thiol oxidation in tumor cells using sulfenic acid-specific antibodies. *Proc. Natl. Acad. Sci. U. S. A.* **106**, 16163–16168 (2009).

118. Seo, Y. H. & Carroll, K. S. Facile synthesis and biological evaluation of a cell-permeable probe to detect redox-regulated proteins. *Bioorganic Med. Chem. Lett.* **19**, 356–359 (2009).

119. Leonard, S. E., Reddie, K. G. & Carroll, K. S. Mining the thiol proteome for sulfenic acid modifications reveals new targets for oxidation in cells. *ACS Chem. Biol.* **4**, 783–799 (2009).

120. Paulsen, C. E. *et al.* Peroxide-dependent sulfenylation of the EGFR catalytic site enhances kinase activity. *Nat. Chem. Biol.* **8**, 57–64 (2012).

121. Gupta, V., Yang, J., Liebler, D. C. & Carroll, K. S. Diverse Redoxome Reactivity Profiles of Carbon Nucleophiles. *J. Am. Chem. Soc.* **139**, 5588–5595 (2017).

122. Lichtman, J. W. & Conchello, J. A. Fluorescence microscopy. *Nat. Methods* **2**, 910–919 (2005).

123. Lakowicz, J. R. *General features of protein fluorescence*. *Principles of Fluorescence Spectroscopy* (2006).

124. Sanderson, M. J., Smith, I., Parker, I. & Bootman, M. D. Fluorescence Microscopy. *Cold Spring Harb. Protoc.* **176**, (2014).

125. Leica HyD for Confocal Imaging. *Leica Microsystems Gmbh* Available at: https://www.leica-microsystems.com/products/confocal-microscopes/p/leica-hyd/.

126. Bastiaens, P. I. H. & Squire, A. Fluorescence lifetime imaging microscopy: Spatial resolution of biochemical processes in the cell. *Trends Cell Biol.* **9**, 48–52 (1999).

127. Wouters, F. S. & Bastiaens, P. I. H. Fluorescence lifetime imaging of receptor tyrosine kinase activity in cells. *Curr. Biol.* **9**, 1127–1130 (1999).

128. Tinoco, I. & Gonzalez, R. L. Biological mechanisms, one molecule at a time. *Genes Dev.* **25**, 1205–1231 (2011).

129. Verveer, P. J., Squire, A. & Bastiaens, P. I. H. Global analysis of fluorescence lifetime imaging microscopy data. *Biophys. J.* **78**, 2127–2137 (2000).

130. Grecco, H. E., Roda-Navarro, P. & Verveer, P. J. Global analysis of time correlated single photon counting FRET-FLIM data. *Opt. Express* **17**, 6493 (2009).

131. Pelet, S., Previte, M. J., Laiho, L. H. & So, P. T. A fast global fitting algorithm for fluorescence lifetime imaging microscopy based on image segmentation. *Biophys. J.* **87**, 2807–2817 (2004).

132. Barber, P. R. *et al.* Multiphoton time-domain fluorescence lifetime imaging microscopy: Practical application to protein-protein interactions using global analysis. *J. R. Soc. Interface* **6**, (2009).

133. Tischer, C. & Bastiaens, P. I. H. Lateral phosphorylation propagation: An aspect of feedback signalling? *Nat. Rev. Mol. Cell Biol.* **4**, 971–975 (2003).

134. Bertics, P. J. & Gill, G. N. Self-phosphorylation enhances the protein-tyrosine kinase activity of the epidermal growth factor receptor. *J. Biol. Chem.* **260**, 14642–14647 (1985).

135. Hsu, C. Y. J., Hurwitz, D. R., Mervic, M. & Zilberstein, A. Autophosphorylation of the intracellular domain of the epidermal growth factor receptor results in different effects on its tyrosine kinase activity with various peptide substrates: Phosphorylation of peptides representing Tyr(P) sites of phospholipase C-. *J. Biol. Chem.* **266**, 603–608 (1991).

136. FISCHER, E. H., CHARBONNEAU, H. & TONKS, N. K. Protein Tyrosine Phosphatases: A Diverse Family of Intracellular and Transmembrane Enzymes. *Science (80-.).* **253**, 401–406 (1991).

137. Lammers, R. *et al.* Differential activities of protein tyrosine phosphatases in intact cells. *J. Biol. Chem.* **268**, 22456–22462 (1993).

138. Stanoev, A. *et al.* Interdependence between EGFR and Phosphatases Spatially Established by Vesicular Dynamics Generates a Growth Factor Sensing and Responding Network. *Cell Syst.* **7**, 295-309.e11 (2018).

139. Sigismund, S., Avanzato, D. & Lanzetti, L. Emerging functions of the EGFR in cancer. *Mol. Oncol.* **12**, 3–20 (2018).

140. Chen, P. H. *et al.* Crosstalk between CLCb/Dyn1-Mediated Adaptive Clathrin-Mediated Endocytosis and Epidermal Growth Factor Receptor Signaling Increases Metastasis. *Dev. Cell* **40**, 278-288.e5 (2017).

141. Han, W., Zhang, T., Yu, H., Foulke, J. G. & Tang, C. K. Hypophosphorylation of residue Y1045 leads to defective downregulation of EGFRvIII. *Cancer Biol. Ther.* **5**, 1361–1368 (2006).

142. Lee, J. C. *et al.* Epidermal growth factor receptor activation in glioblastoma through novel missense mutations in the extracellular domain. *PLoS Med.* **3**, 2264–2273 (2006).

143. Westover, D., Zugazagoitia, J., Cho, B. C., Lovly, C. M. & Paz-Ares, L. Mechanisms of acquired resistance to first-and second-generation EGFR tyrosine kinase inhibitors. *Ann. Oncol.* **29**, i10–i19 (2018).

144. Chan, G., Kalaitzidis, D. & Neel, B. G. The tyrosine phosphatase Shp2 (PTPN11) in cancer. *Cancer Metastasis Rev.* **27**, 179–192 (2008).

145. Bowen, M. E. *et al.* Loss-of-function mutations in PTPN11 cause metachondromatosis, but not ollier disease or maffucci syndrome. *PLoS Genet.* **7**, (2011).

146. Kleppe, M. *et al.* Deletion of the protein tyrosine phosphatase gene PTPN2 in T-cell acute lymphoblastic leukemia. *Nat. Genet.* **42**, 530–535 (2010).

147. Shields, B. J. *et al.* TCPTP Regulates SFK and STAT3 Signaling and Is Lost in Triple-Negative Breast Cancers. *Mol. Cell. Biol.* **33**, 557–570 (2013).

148. Veeriah, S. *et al.* The tyrosine phosphatase PTPRD is a tumor suppressor that is frequently inactivated and mutated in glioblastoma and other human cancers. *Proc. Natl. Acad. Sci. U. S. A.* **106**, 9435–9440 (2009).

149. Zhao, Y. *et al.* Identification and functional characterization of paxillin as a target of protein tyrosine phosphatase receptor T. *Proc. Natl. Acad. Sci. U. S. A.* **107**, 2592–2597 (2010).

150. Burgoyne, A. M. *et al.* Proteolytic cleavage of protein tyrosine phosphatase μ regulates glioblastoma cell migration. *Cancer Res.* **69**, 6960–6968 (2009).

151. Anders, L. *et al.* Furin-, ADAM 10-, and Gamma-Secretase-Mediated Cleavage of a Receptor Tyrosine Phosphatase and Regulation of Beta-Catenin's Transcriptional Activity. *Mol. Cell. Biol.* **26**, 3917–3934 (2006).

152. Fournier, P., Dussault, S., Fusco, A., Rivard, A. & Royal, I. Tyrosine phosphatase PTPRJ/DEP-1 Is an essential promoter of vascular permeability, angiogenesis, and tumor progression. *Cancer Res.* **76**, 5080–5091 (2016).

153. LaForgia, S. *et al.* Receptor protein-tyrosine phosphatase γ is a candidate tumor suppressor gene at human chromosome region 3p21. *Proc. Natl. Acad. Sci. U. S. A.* **88**, 5036–5040 (1991).

154. Van Niekerk, C. C. & Poels, L. G. Reduced expression of protein tyrosine phosphatase gamma in lung and ovarian tumors. *Cancer Lett.* **137**, 61–73 (1999).

155. Van Roon, E. H. J. *et al.* Tumor-specific methylation of PTPRG intron 1 locus in sporadic and Lynch syndrome colorectal cancer. *Eur. J. Hum. Genet.* **19**, 307–312 (2011).

156. Cheung, A. K. L. *et al.* PTPRG suppresses tumor growth and invasion via inhibition of Akt signaling in nasopharyngeal carcinoma. *Oncotarget* **6**, 13434–13447 (2015).

157. Stevenson, W. S. *et al.* DNA methylation of membrane-bound tyrosine phosphatase genes in acute lymphoblastic leukaemia. *Leukemia* **28**, 787–793 (2014).

158. Xiao, J. *et al.* PTPRG inhibition by DNA methylation and cooperation with RAS gene activation in childhood acute lymphoblastic leukemia. *Int. J. Cancer* **135**, 1101–1109 (2014).

159. Rostovtsev, V. V, Green, L. G., Fokin, V. V & Sharpless, K. B. A stepwise huisgen cycloaddition process: Copper(I)-catalyzed regioselective 'ligation' of azides and terminal alkynes. *Angew. Chemie - Int. Ed.* **41**, 2596–2599 (2002).

160. Ran, F. A. *et al.* Genome engineering using the CRISPR-Cas9 system. *Nat. Protoc.* **8**, 2281–2308 (2013).

161. Vezzalini, M. *et al.* Expression of transmembrane protein tyrosine phosphatase gamma (PTPγ) in normal and neoplastic human tissues. *Histopathology* **50**, 615–628 (2007).

162. Charafe-Jauffret, E. *et al.* Gene expression profiling of breast cell lines identifies potential new basal markers. *Oncogene* **25**, 2273–2284 (2006).

163. Kavanaugh, M. W. & Williams, L. T. An Alternative to SH2 Domains for Binding Tyrosine-Phosphorylated Proteins. *Science (80-.).* **266**, 1862–1865 (1994).

164. Offterdinger, M., Georget, V., Girod, A. & Bastiaens, P. I. H. Imaging phosphorylation dynamics of the epidermal growth factor receptor. *J. Biol. Chem.* **279**, 36972–36981 (2004).

165. Konturek, J. W., Bielanski, W., Konturek, S. J., Bogdal, J. & Oleksy, J. Distribution and release of epidermal growth factor in man. *Gut* **30**, 1194–1200 (1989).

166. Stanoev, A., Nandan, A. P. & Koseska, A. Organization at criticality enables processing of time-varying signals by receptor networks. *Mol. Syst. Biol.* **16**, 1–13 (2020).

167. Endres, N. F. *et al.* Conformational coupling across the plasma membrane in activation of the EGF receptor. *Cell* **152**, 543–556 (2013).

168. Paulsen, C. E. & Carroll, K. S. Orchestrating Redox Signaling Networks through Regulatory Cysteine Switches. *ACS Chem. Biol.* **5**, 47–62 (2010).

169. Lim, D. C., Joukov, V. & Yaffe, M. B. Are redox changes a critical switch for mitotic progression? *Mol. Cell. Oncol.* **7**, 6–8 (2020).

170. Yaffe, M. B. Predicting the future of signaling for 2018. *Sci. Signal.* **11**, (2018).

171. Warren, R. A., Green, F. A., Stenberg, P. E. & Enns, C. A. Distinct saturable pathways for the endocytosis of different tyrosine motifs. *J. Biol. Chem.* **273**, 17056–17063 (1998).

172. Szatrowski, T. P. & Nathan, C. F. Production of Large Amounts of Hydrogen Peroxide by Human Tumor Cells. *Cancer Res.* **51**, 794–798 (1991).

173. Liou, G. Y. & Storz, P. *Reactive oxygen species in cancer*. *Free Radical Research* **44**, (2010).

174. Toullec, A. *et al.* Oxidative stress promotes myofibroblast differentiation and tumor spreading. *EMBO Mol. Med.* **2**, 211–230 (2010).

175. Weinberg, F. *et al.* Mitochondrial metabolism and ROS generation are essential for Kras-mediated tumorigenicity. *Proc. Natl. Acad. Sci. U. S. A.* **107**, 8788–8793 (2010).

176. Fuchs, T. A. *et al.* Novel cell death program leads to neutrophil extracellular traps. *J. Cell Biol.* **176**, 231–241 (2007).

177. Grecco, H. E., Schmick, M. & Bastiaens, P. I. H. Signaling from the living plasma membrane. *Cell* **144**, 897–909 (2011).

Acknowledgments

The First and the foremost, I would like to thank my thesis adviser Prof. Dr. Philippe Bastiaens for giving me an opportunity to work on exciting projects in his laboratory, but more importantly for encouraging me to think out of the box which helped me a lot to evolve as a scientist. His passion for science and enthusiasm to learn will keep inspiring me. I would like to thank Dr. Leif Dehmelt for being the second reviewer of this thesis.

I would like to thank the PTP squad: Angel, Amit, Klaus, Rabea, Yannick, Martin and Wayne for helping me with developing conceptual ideas and experimental techniques on the foundation of which my project strengthened. And of course, working with Aneta made my learning experience even more interesting.

My special thanks to Lisaweta, Kirsten, Hendrike, Jutta, Manuela, Micha and Michelle for their unceasing help with laboratory assistance. I would like to extend my thanks to Sven and Michael for supporting me on demand with microscopy and FACS. I would like to thank Christa, Lucia, Astrid and Tanja for making all the administrative work hassle-free for me.

I would like to thank Vaishnavi and Kitso for constantly caring for my happiness and helping me to stay mentally strong. Akhilesh, Abhishek, Manish, Dhruv, Ola and Sarah, thank you for being my family away from home and making the duration of my PhD a memorable experience.

I would like to extend my thanks to Aai, Baba and Nirmayi for their constant support from India and enormous contribution in shaping my personality. Many thanks to Nikita, Reva, Prachi and Megha for encouragement and support. Thanks Wim, for always being there for me and believing in me.

Finally, I would further extend my gratitude to all the current and past members of department 2 for sharing creative ideas, prolific discussions and enjoyable times!